Single-cell profiling of trabecular meshwork identifies mitochondrial dysfunction in a glaucoma model that is protected by vitamin B3 treatment

Nicholas Tolman[1¶], Taibo Li[2¶], Revathi Balasubramanian[1¶], Guorong Li[3], Rebecca Pfeiffer[5], Violet Bupp-Chickering[1], Ruth A. Kelly[3], Marina Simón[1], John Peregrin[1], Christa Montgomery[1], Bryan Jones[5], W. Daniel Stamer[3]*, Jiang Qian[4]*, Simon W.M. John[1,6]*

1. Department of Ophthalmology, Columbia University Irving Medical Center, New York, NY
2. Department of Biomedical Engineering, Johns Hopkins University, Baltimore, MD
3. Department of Ophthalmology, Duke University, Durham, NC 27710.
4. Department of Ophthalmology, Johns Hopkins School of Medicine, Baltimore, MD
5. Department of Ophthalmology, University of Pittsburgh, Pittsburgh, PA
6. Zuckerman Mind Brain Behavior Institute, Columbia University, New York, NY

*Corresponding author
E-mail: sj2967@cumc.columbia.edu (SWMJ)
E-mail: william.stamer@duke.edu (WDS)
E-mail: jiang.qian@jhmi.edu (JQ)

¶These authors contributed equally to this work.

Abstract

Since the trabecular meshwork (TM) is central to intraocular pressure (IOP) regulation and glaucoma, a deeper understanding of its genomic landscape is needed. We present a multimodal, single-cell resolution analysis of mouse limbal cells (includes TM). In total, we sequenced 9,394 wild-type TM cell transcriptomes. We discovered three TM cell subtypes with characteristic signature genes validated by immunofluorescence on tissue sections and whole-mounts. The subtypes are robust, being detected in datasets for two diverse mouse strains and in independent data from two institutions. Results show compartmentalized enrichment of critical pathways in specific TM cell subtypes. Distinctive signatures include increased expression of genes responsible for 1) extracellular matrix structure and metabolism (TM1 subtype), 2) secreted ligand signaling to support Schlemm's canal cells (TM2), and 3) contractile and mitochondrial/metabolic activity (TM3). ATAC-sequencing data identified active transcription factors in TM cells, including LMX1B. Mutations in *LMX1B* cause high IOP and glaucoma. LMX1B is emerging as a key transcription factor for normal mitochondrial function and its expression is much higher in TM3 cells than other limbal cells. To understand the role of LMX1B in TM function and glaucoma, we single-cell sequenced limbal cells from *Lmx1b*$^{V265D/+}$ mutant mice (2,491 TM cells). In *V265D/+* mice, TM3 cells were uniquely affected by pronounced mitochondrial pathway changes. Mitochondria in TM cells of *V265D/+* mice are swollen with a reduced cristae area, further supporting a role for mitochondrial dysfunction in the initiation of IOP elevation in these mice. Importantly, treatment with vitamin B_3 (nicotinamide), to enhance mitochondrial function and metabolic resilience, significantly protected *Lmx1b* mutant mice from IOP elevation.

Introduction:

Aqueous humor (AH) dynamics and pressure homeostasis are important for proper ocular inflation and vision. Elevated intraocular pressure (IOP) is a key risk factor for glaucoma, a serious blinding disorder that affects 80 million people worldwide [1]. IOP is controlled by continually adjusting resistance to drainage (outflow) of AH through the trabecular meshwork (TM) and Schlemm's canal (SC), the primary route of AH outflow from the eye. AH percolates through the TM before exiting the eye through SC and then entering the venous circulation. As the most abundant constituent of the conventional outflow pathway, TM cells are central in regulating AH drainage and IOP. Despite significant advances over the past few decades, a much deeper understanding of the molecular mechanisms governing TM cell health and function, as well as the pathological alterations responsible for increased outflow resistance, elevated IOP, and increased glaucoma risk are still needed.

The TM is located at the inner aspect of the wall of the eye at the iridocorneal angle just anterior to where the iris and cornea meet (i.e. the limbus). In humans, the TM is morphologically separated into distinct zones, including the uveal, corneoscleral, and juxtacanalicular trabecular meshwork (JCT), which lies adjacent to the SC. AH first drains through the uveal and corneoscleral meshwork whose TM cells have endothelial-like properties [2-4]. In these regions, the TM consists of beams and plates made of various extracellular matrix (ECM) components including fibrillar collagens [5-9]. The beams and plates are covered with monolayers of TM cells. AH drains through a tortuous series of intertrabecular spaces, which run between the beams, ensuring interaction with TM cells. Next, AH flows into the less structured JCT region before entering the SC. The JCT consists of TM cells that are fibroblast-like extending their processes onto neighboring JCT and SC cells. JCT TM cells are embedded within a diffuse

ECM ground substance (including glycosaminoglycans) [2, 10-12], and have contractile smooth muscle-like properties [2, 13]. Importantly, cells in the JCT region impose critical resistance to AH outflow with a major site of resistance to outflow being located in the tissue where the JCT and SC meet [5, 12, 14, 15].

Regulation of AH outflow resistance and IOP homeostasis by TM cells is complicated. AH outflow is modulated by: 1) The physical properties (shape/volume and contractility) of the TM cells. For example, some TM cells have smooth muscle-like properties that adjust outflow resistance and thus IOP by controlling cellular contractility [16-23]. 2) The effects of different TM cell types on both the composition and abundance of ECM in the JCT due to ECM synthesis/ metabolism and phagocytic activity. 3) The paracrine or physical effects of TM cells on SC and possibly the vasculature just distal to SC [24-27].

Due to their importance, a more detailed molecular characterization of TM cells is still required. The degree to which specific pathways and modulatory roles are compartmentalized or shared by specific TM cell subtypes and how specific subtypes influence each other and the SC are not known. In fact, the number of molecularly distinct subtypes is currently unknown as is the role of the > 120 genes associated with elevated IOP within these subtypes [28]. Although the TM has fewer beams and a narrower drainage path in mice, developmental, functional and anatomical similarities between human and mouse TM make mice a valuable model for studying the molecular characteristics, heterogeneity, subtypes and distribution of TM cells [29, 30].

Single-cell resolution transcriptomic profiling is revolutionizing the molecular characterization of cell types and cellular heterogeneity (single-cell RNA sequencing, scRNA-seq; and single-nucleus, snRNA-seq). Initial single-cell-level studies have characterized cell types of the ocular anterior segment, including TM cells [24, 26, 31-33], but further depth, validation, and more

uniform molecular consensus/ naming of cell types are needed. This is especially true for TM cells. Currently, reports differ in the naming and definition of TM cell subtypes and offer limited validation by immunohistochemistry (IHC) or immunofluorescence (IF) on tissue sections or flat mounts.

Here we more deeply characterized the mouse TM and validated findings by immunostaining tissue sections and flat mounts and by in situ hybridization (ISH). We independently isolated and sequenced limbal cells of mice at 2 institutions and characterized the same 3 TM cell subtypes at both. Additionally, single-nucleus assay for transposase-accessible chromatin with sequencing (snATAC-seq) identified LIM homeobox transcription factor 1 beta (LMX1B) as one of the most active transcription factors in TM cells. Variants in *LMX1B* cause IOP elevation and glaucoma [28, 34-38]. By analyzing *Lmx1b*$^{V265D/+}$ mutant mice (develop elevated IOP and glaucoma) [39, 40], we show that mitochondrial pathways are primarily disturbed in the TM3 cell subtype, which most strongly expresses *Lmx1b*. Treatment with nicotinamide lessened IOP elevation in *Lmx1b*$^{V265D/+}$ mutants supporting testing of therapeutics that boost mitochondrial health and function in human patients.

Results

Three molecularly distinct TM cell subtypes

Using scRNA-seq, we sequenced 17,914 cells from dissected limbal tissue (contains drainage structures) of 2-month-old mice. The dataset included 13,251 cells from strain C57BL/6J (B6) and 4,663 cells from strain 129/Sj (129). The data for both strains were integrated (S1 Fig). Computational analysis revealed six distinct clusters of cells that were TM-containing, epithelia,

126 pigmented epithelia (iris and ciliary body), endothelial, immune and neuron (Fig 1A). The identity
127 of each of these cell clusters was based on various well-characterized marker genes (S2A-B
128 Fig) [24, 26, 31]. There were no major differences in the distributions of strain B6 and strain 129
129 cells within the relevant cell-type clusters (S3A-C Fig). Therefore, to improve statistical power,
130 downstream analyses used the integrated dual-strain dataset.
131
132 Cells of cluster 1 expressed various TM genes, including *Acta2* (α-SMA), *Pitx2*, *Tfap2b*, and
133 *Myoc* (S2A-B Fig) [26, 31, 41-43]. Unbiased sub-clustering of Cluster 1 revealed 10 distinct sub-
134 clusters (Fig 1B), which included three TM cell clusters based on signature gene expression
135 (Fig 1D-E). We named these clusters TM1, TM2, and TM3. Hierarchical clustering of these cell
136 types indicated that TM1 and TM2 are more molecularly similar to each other than to TM3 (Fig
137 1C). The remaining seven clusters were identified as cells from other ocular tissue including the
138 iris stroma, sclera, corneal keratocytes, corneal endothelium, ciliary muscle, pericytes, and
139 Schwann cells (S2C Fig) [32, 44-50].

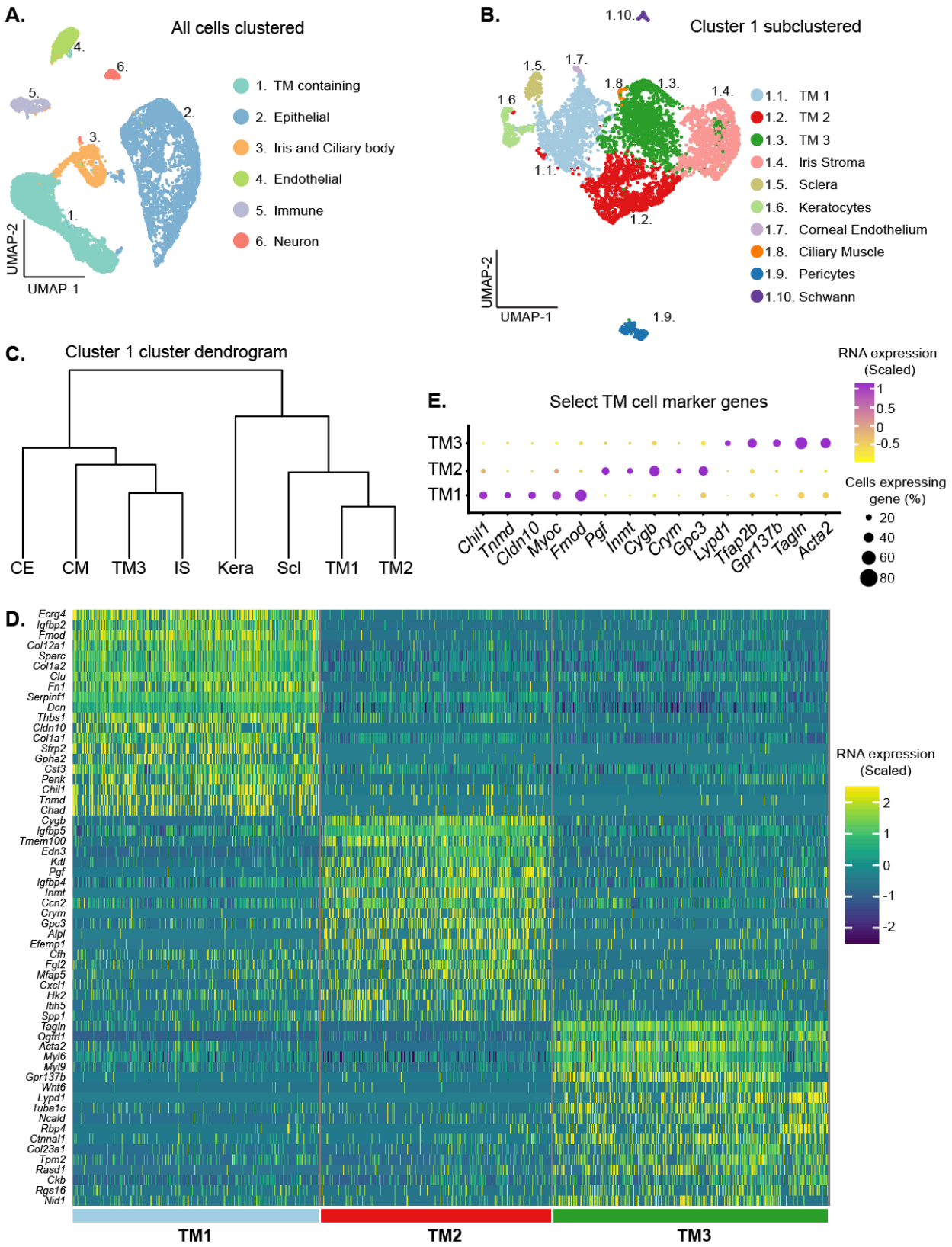
A.
All cells clustered
1. TM containing
2. Epithelial
3. Iris and Ciliary body
4. Endothelial
5. Immune
6. Neuron
UMAP-2
UMAP-1
B.
Cluster 1 subclustered
1.1. TM 1
1.2. TM 2
1.3. TM 3
1.4. Iris Stroma
1.5. Sclera
1.6. Keratocytes
1.7. Corneal Endothelium
1.8. Ciliary Muscle
1.9. Pericytes
1.10. Schwann
C.
Cluster 1 cluster dendrogram
CE
CM
TM3
IS
Kera
Scl
TM1
TM2
E.
Select TM cell marker genes
TM3
TM2
TM1
Chil1
Tnmd
Cldn10
Myoc
Fmod
Pgf
Inmt
Cygb
Crym
Gpc3
Lypd1
Tfap2b
Gpr137b
Tagln
Acta2
RNA expression (Scaled)
Cells expressing gene (%)
D.
Ecrg4
Igfbp2
Fmod
Col12a1
Sparc
Col1a2
Clu
Fn1
Serpinf1
Dcn
Thbs1
Cldn10
Col1a1
Sfrp2
Gpha2
Cst3
Penk
Chil1
Tnmd
Chad
Cygb
Igfbp5
Tmem100
Edn3
Kitl
Pgf
Igfbp4
Inmt
Ccn2
Crym
Gpc3
Alpl
Efemp1
Cfh
Fgl2
Mfap5
Cxcl1
Hk2
Itih5
Spp1
Tagln
Ogfrl1
Acta2
Myl6
Myl9
Gpr137b
Wnt6
Lypd1
Tuba1c
Ncald
Rbp4
Ctnnal1
Col23a1
Tpm2
Rasd1
Ckb
Rgs16
Nid1
TM1
TM2
TM3
RNA expression (Scaled)

140

Fig 1. scRNA-seq data identifies three TM cell clusters. (A) Cells from limbal tissue dissected and sequenced at Columbia University (integrated B6 and 129/Sj datasets) are depicted in clusters on a UMAP space. **(B)** A separate UMAP representation of the trabecular meshwork (TM) containing cluster following subclustering. Three distinct TM cell clusters are identified (TM1, TM2, and TM3). **(C)** Dendrogram illustrating the relationships among these subclusters. TM1 and TM2 are more similar to each other than to TM3. **(D)** Heatmap showing the signature genes for TM1, TM2, and TM3 cells. The scaled RNA expression indicates how many standard deviations a given gene's expression is from the average expression across all examined cells (positive value is greater than the expression average and negative values are lower than expression average). **(E)** The scaled expression of select marker genes that robustly differentiate TM cell subsets from each other are shown with a dot plot. CE: corneal endothelium, CM: ciliary muscle, IS: iris stroma, Kera: corneal keratocytes, Scl: scleral.

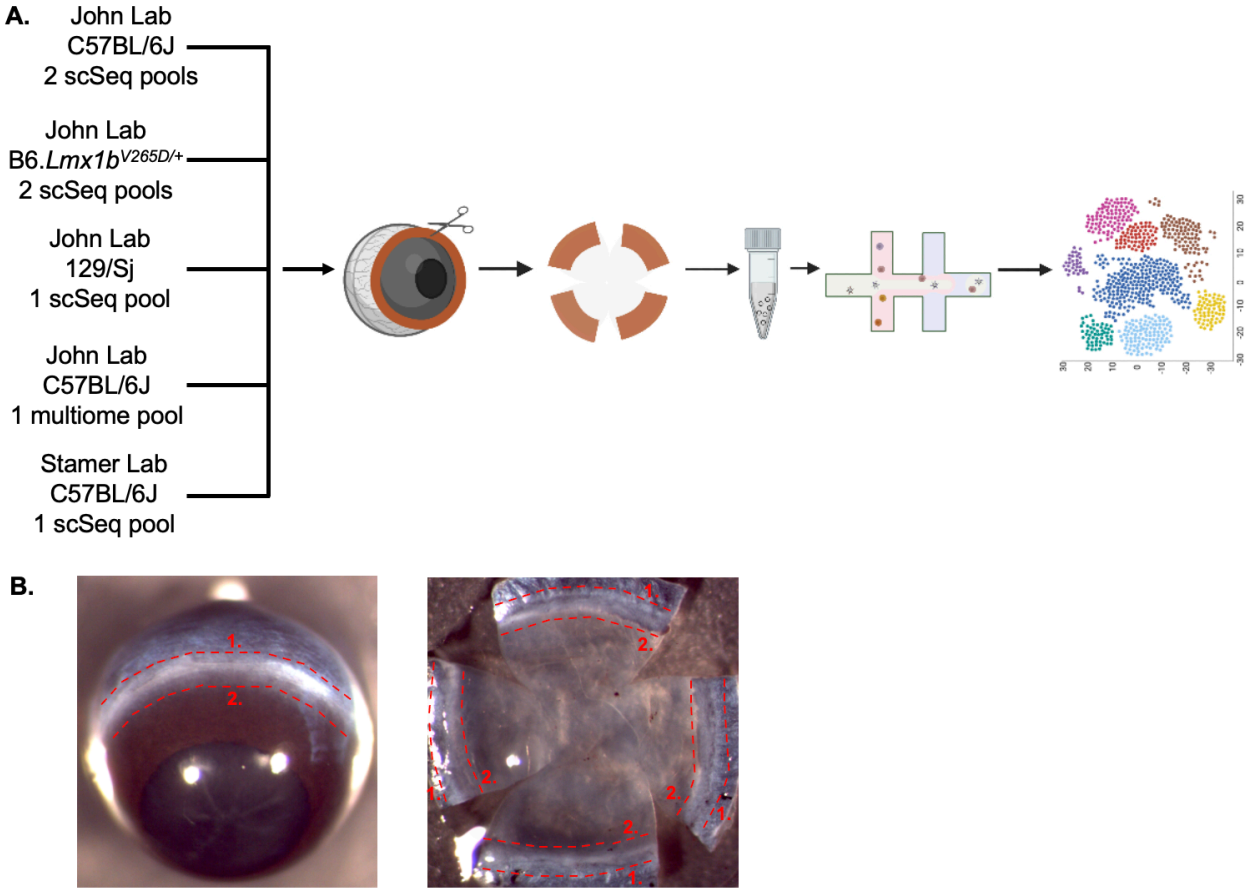

S1 Fig. Schematic of datasets and pipeline. (A) Each pool included limbal tissue from 8 eyes. The mouse strains and lab where data were generated are shown (Columbia University, John Lab or Duke, Stamer lab). Individual eyes were dissected to isolate strips of limbal tissue, which are enriched for TM cells in comparison to dissecting the anterior segment as a whole. Limbal strips were then minced and pooled for further processing. Individual cells were sequenced using the 10X Genomics pipeline (see Methods) for sc-RNA-Seq or multiome (snRNA-seq and scATAC-seq). Schematic created with BioRender.com. **(B)** (Left) The limbal region of the enucleated eye is outlined with red dotted lines. The posterior portion of the eye is first removed by making a cut along line1. After lens removal, a second cut is made through the anterior cornea and iris along line 2, generating a limbal strip. This strip is then minced prior to dissociation. (Right) A dissected anterior eye cup (with the lens removed) is shown to indicate the interior surface of the limbus between lines 1 and 2. Centripetal cuts were made in the

173 cornea of this specimen to flatten it for ease of imaging. Although we do not flatten limbal strips

174 used for RNA-seq, this view provides additional context.

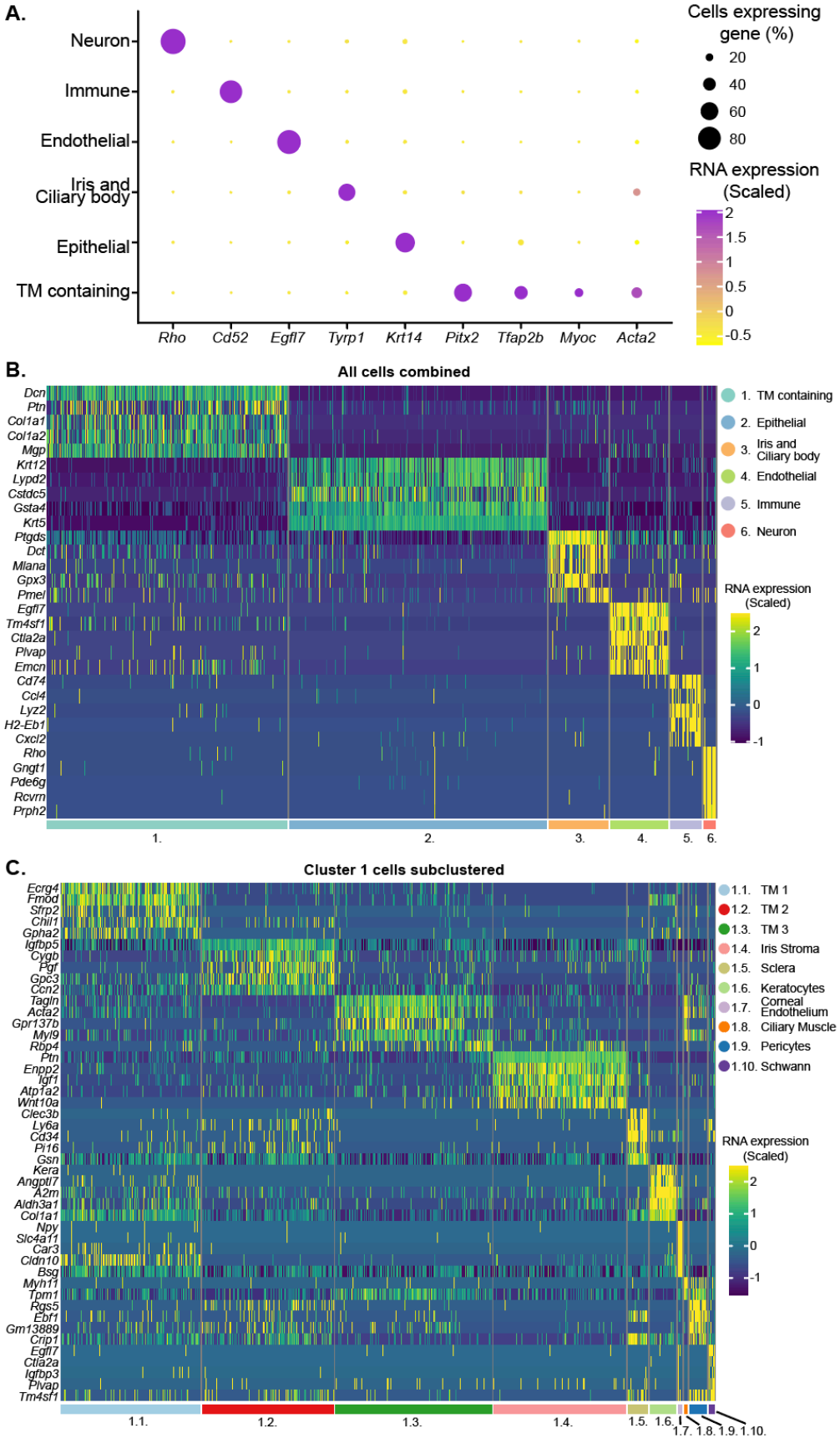
A.
Neuron
Immune
Endothelial
Iris and Ciliary body
Epithelial
TM containing
Rho
Cd52
Egfl7
Tyrp1
Krt14
Pitx2
Tfap2b
Myoc
Acta2
Cells expressing gene (%)
20
40
60
80
RNA expression (Scaled)
2
1.5
1
0.5
0
-0.5
B.
All cells combined
Dcn
Ptn
Col1a1
Col1a2
Mgp
Krt12
Lypd2
Cstdc5
Gsta4
Krt5
Ptgds
Dct
Mlana
Gpx3
Pmel
Egfl7
Tm4sf1
Ctla2a
Plvap
Emcn
Cd74
Ccl4
Lyz2
H2-Eb1
Cxcl2
Rho
Gngt1
Pde6g
Rcvrn
Prph2
1. TM containing
2. Epithelial
3. Iris and Ciliary body
4. Endothelial
5. Immune
6. Neuron
RNA expression (Scaled)
2
1
0
-1
1.
2.
3.
4.
5.
6.
C.
Cluster 1 cells subclustered
Ecrg4
Fmod
Sfrp2
Chil1
Gpha2
Igfbp5
Cygb
Pgf
Gpc3
Ccn2
Tagln
Acta2
Gpr137b
Myl9
Rbp4
Ptn
Enpp2
Igf1
Atp1a2
Wnt10a
Clec3b
Ly6a
Cd34
Pi16
Gsn
Kera
Angptl7
A2m
Aldh3a1
Col1a1
Npy
Slc4a11
Car3
Cldn10
Bsg
Myh11
Tpm1
Rgs5
Ebf1
Gm13889
Crip1
Egfl7
Ctla2a
Igfbp3
Plvap
Tm4sf1
1.1. TM 1
1.2. TM 2
1.3. TM 3
1.4. Iris Stroma
1.5. Sclera
1.6. Keratocytes
1.7. Corneal Endothelium
1.8. Ciliary Muscle
1.9. Pericytes
1.10. Schwann
RNA expression (Scaled)
2
1
0
-1
1.1.
1.2.
1.3.
1.4.
1.5.
1.6.
1.7.
1.8.
1.9.
1.10.

175

176 **S2 Fig. Limbal cell cluster marker genes. (A)** The expression levels of various anterior
177 segment cell type marker genes in the integrated B6 and 129 data are depicted on a dot plot.
178 These marker genes are generally accepted to be specific to individual cell types. Epithelial
179 cells (*Krt14*); neurons (*Rho*); endothelial cells (*Egfl7*); ciliary body and iris cells (*Tyrp1*); and
180 immune cells (*Cd52*). Cluster 1 expressed multiple TM marker genes including *Myoc*, *Acta2*
181 (encodes α-SMA), *Pitx2*, and *Tfap2b*. Although some of the neurons may be limbal, it is possible
182 that others are retinal contamination. **(B-C)** Heatmaps of differentially expressed genes across
183 all limbal tissue cell clusters (B) and across the subclusters of cluster 1 (C).
184

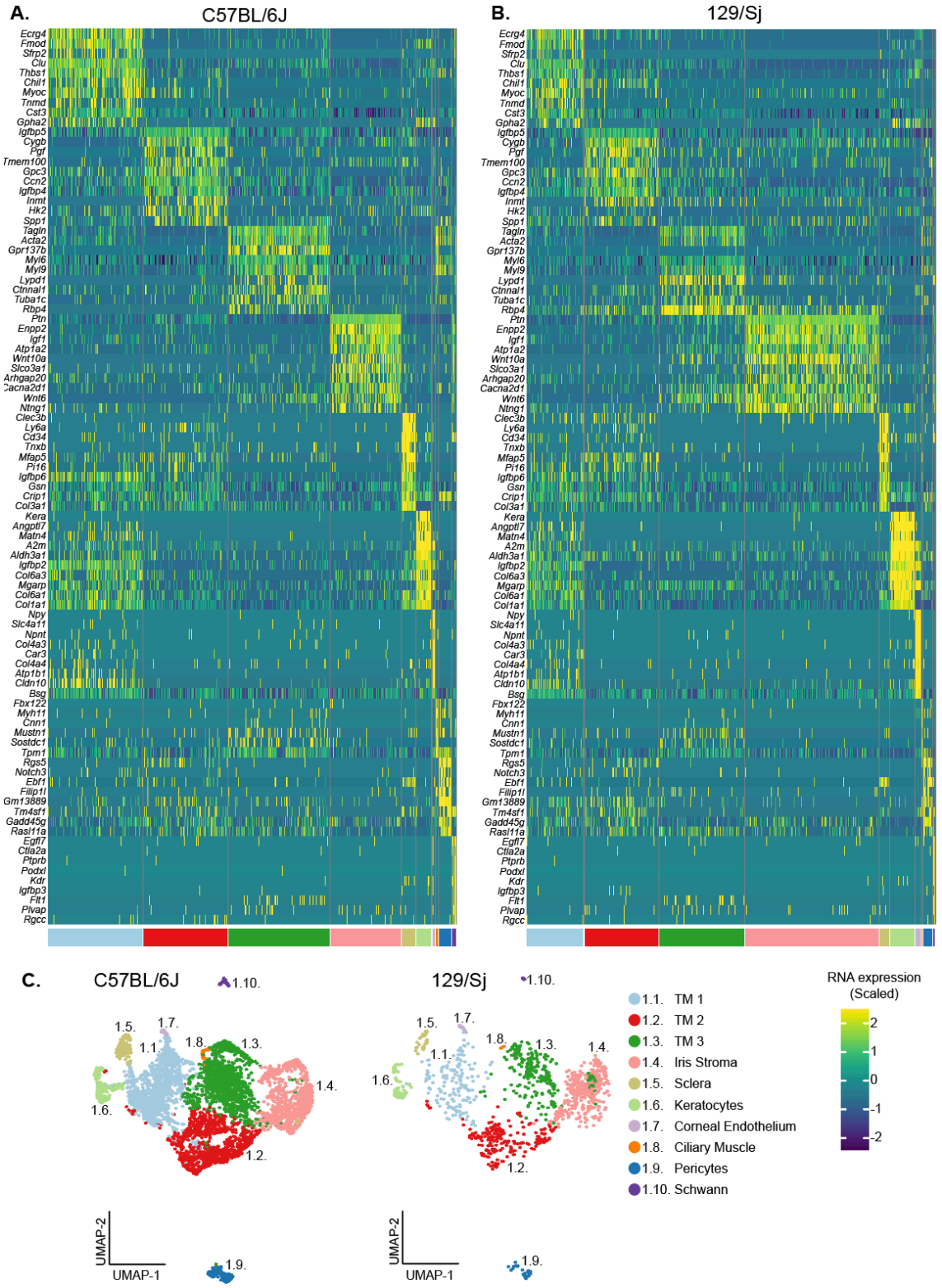

S3 Fig. Transcriptomic similarities between strain B6 and strain 129.

(A-B) The 129/Sj (129) and C57BL/6J (B6) strains exhibit significant overlap in marker gene expression. Heatmaps display the expression of the top 10 gene markers for each subcluster of

cluster 1. The expression patterns are very similarity across strains. **(C)** UMAP representations of subclusters derived from cluster 1 separated by strain.

214 Next, we integrated an additional limbal tissue scRNA-seq dataset (14,912 cells, Duke
215 University) from 3 months old C57BL/6J mice with our initial 2 months old C57BL/6J dataset.
216 Due to batch effects most likely based on differences in cell isolation techniques and
217 environment (Columbia University vs. Duke University, see Methods), TM cells from these
218 datasets occupied adjacent, partially overlapping, but not identical UMAP space (S4A Fig).
219 Individual analysis of the Duke dataset also identified 3 TM cell subtypes with the same marker
220 gene expression and enriched molecular pathways compared to the Columbia University data
221 (S4B-E Fig, S1 Table). In datasets from previous mouse limbal scRNA-seq studies, there was
222 also a high degree of overlap of marker gene expression with our 3 TM cell clusters (S5A-B Fig)
223 [24, 31, 51]. However, some TM subtype clusters reported in previous studies expressed genes
224 that overlapped with both of our TM2 and scleral cell clusters (S5B-C Fig) [24, 31]. To resolve
225 this discrepancy, we performed IF for two of the discordantly annotated markers previously
226 reported to be expressed in TM cells but present in our scleral cluster (CD34 and LY6C1). This
227 immunolabeling showed that these markers are expressed in scleral but not TM cells (S6A-B
228 Fig). In addition, in previous studies, cells with markers matching TM3 (e.g. Lypd1) were named
229 uveal cells without IF confirmation [24, 31, 51]. IF revealed that our TM3 cells are neither
230 located in the uvea nor abundant in the uveal adjacent TM but primarily reside in the anterior
231 TM closer to the cornea (see below).
232

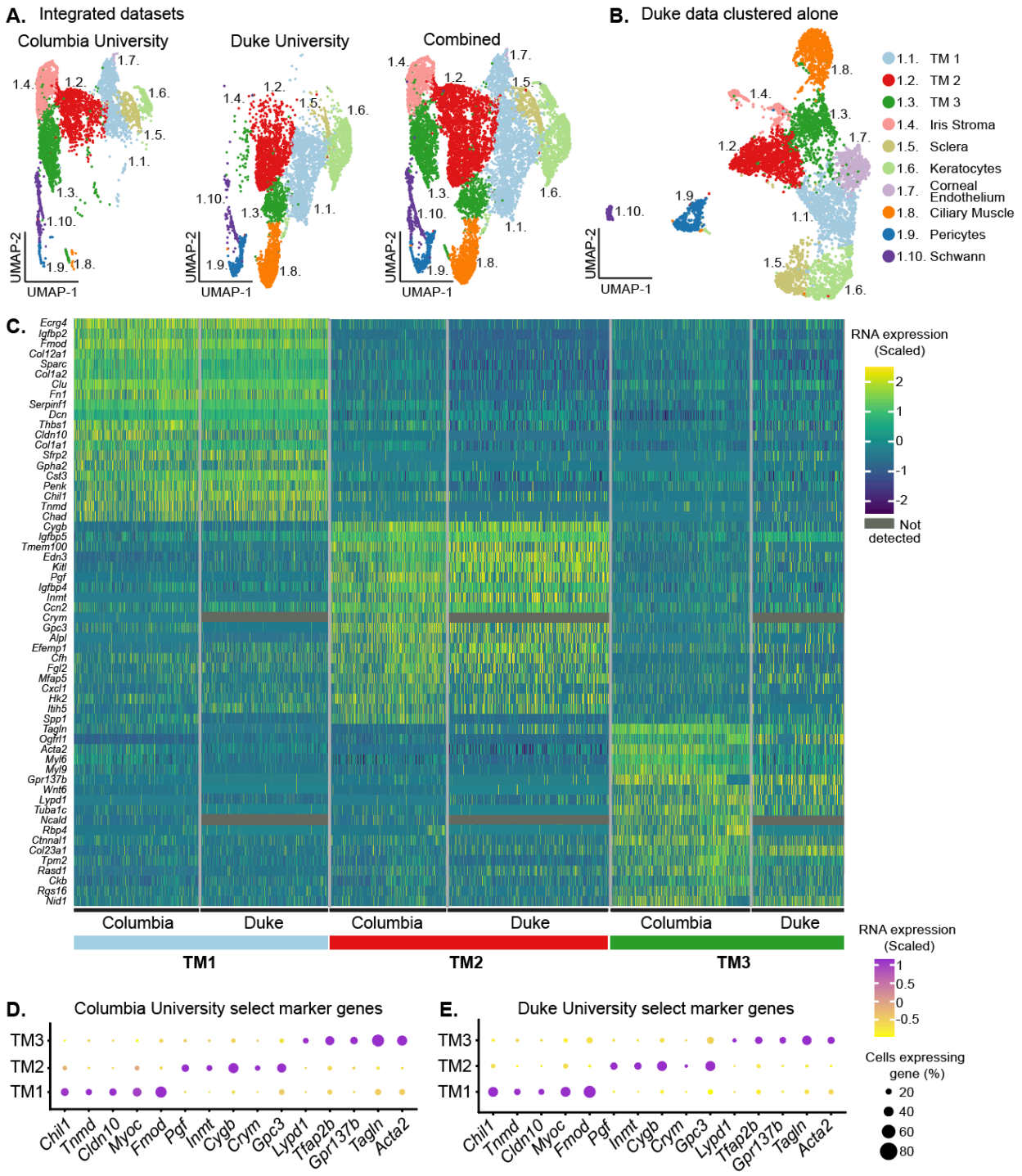

S4 Fig. An independent B6 scRNA-seq dataset corroborates TM cell clusters. (A) UMAPs of the integrated Columbia University and Duke University datasets. Cells from the different institutions occupy largely different but adjacent UMAP coordinates with some overlap, indicating batch effects. The difference was largest for TM3, but the marker genes were still

238 conserved. Because tissue processing techniques can alter gene expression [52], the heatmap
239 variation between institutes likely reflects differences in processing techniques (Methods) and
240 suggests that TM3 cells are more susceptible to these effects than other cell types. **(B)** Analysis
241 of Duke University data alone independently validates our findings presented in *Figure 1* from
242 Columbia University, including the presence of 3 TM cell clusters. **(C)**. A heatmap comparing
243 the top 20 marker genes of each TM cell subcluster for the Columbia (C57BL/6J strain only) and
244 Duke datasets. Overall, there is strong overlap of TM cell gene expression between datasets.
245 Discrepancies include certain marker genes (eg. *Crym*) in the Columbia dataset that are not
246 detected in the Duke dataset. These differences are associated with lower sequencing depth in
247 the Duke data, and other technical factors/batch effects. **(D-E)** Dot plots showing similar TM
248 subtype marker gene expression in the two datasets.
249

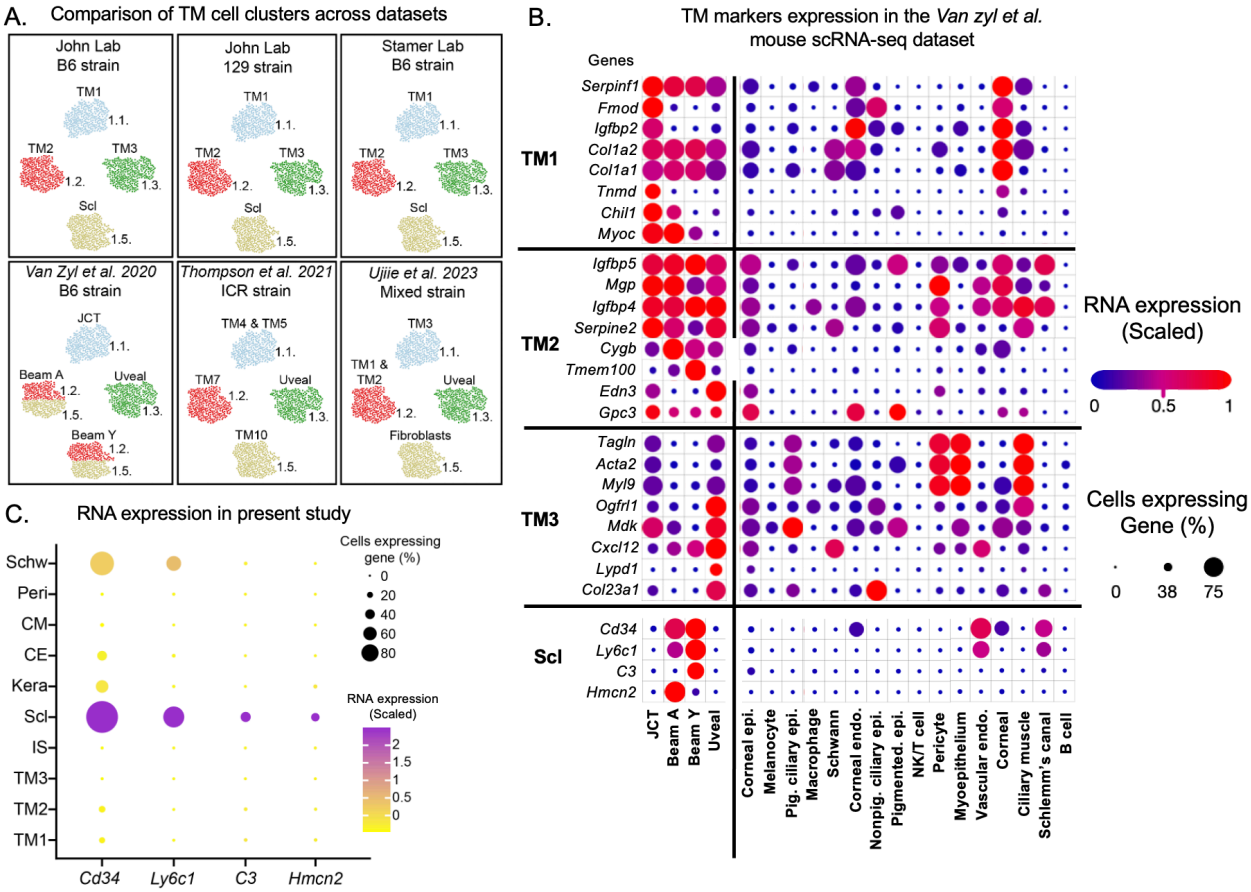

S5 Fig. Comparison of our TM cells to published mouse datasets (A) Diagrammatic representation of TM and scleral cell clusters across different mouse scRNA-seq datasets. **Upper panels** diagrammatically represent the current study. **Lower panels** represent the indicated studies. All diagrams based on marker gene expression in the cells that were clustered together. Despite some naming differences, matches for the 3 TM cell types that we identify in the current paper are evident in the previous studies. Although previous studies named additional TM subtypes, we did not subcluster to the same degree to ensure that subtype differences are robust. Previous studies had limited if any validation for some cell types. Based on our current characterization and immunofluorescent localization studies (Figures 2, S6, S8, & S9) some of the cells previously labeled TM beam cells are scleral (possibly fibroblasts). The marker gene expression for these previously named TM beam cells is highest in 'Fibroblasts' rather than TM cells in human scRNA-seq data, further supporting a scleral

263 identity. In addition, cells previously named as uveal cells are a TM cell type. The cells are
264 color-coded based on their molecular identities to match the current study. Current study
265 subcluster identity numbers are shown. **(B)** Dot plot of TM cell subtype markers identified in the
266 present study (left) using the dataset and cell type assignments (bottom) of Van Zyl et al. Based
267 on these markers, our TM subtypes match their data as follows: TM1= JCT, TM2 = Beam A and
268 Beam Y, and TM3 = Uveal). Scleral markers that we found are enriched in the Van Zyl Beam A
269 and Y cells, which appear to be a mix of different cell types. **(C)** Expression of the Van Zyl Beam
270 A and Y cell markers that are enriched in sclera in our combined B6 and 129 dataset (the same
271 expression pattern was evident in all Columbia and Duke datasets in the current study). See
272 Figure S6 for IF showing expression of these markers in Sclera but not TM.
273
274
275
276
277
278
279
280
281
282
283

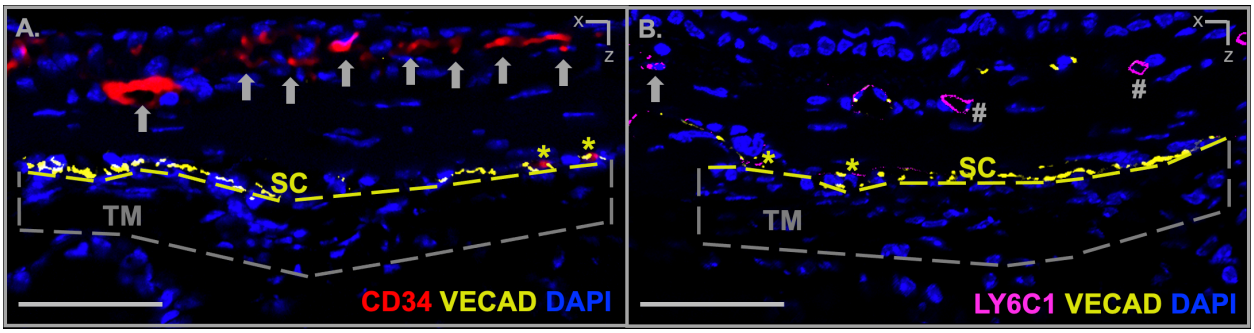

S6 Fig. Immunostaining demonstrates expression of specific marker genes in sclera but not TM. (**A**) CD34 is expressed in cells of the sclera/corneoscleral transition zone (arrows). No CD34 staining was found in the TM (> 60 sections from 4 eyes). **(B)** LY6C1 is expressed in both vascular (based on morphology and the vascular endothelial cell marker, VECAD, hash marks) and nonvascular (arrow) cells in the sclera. LY6C1 is not found in the TM. The TM is encompassed within the dashed box while the yellow dashed line marks the inner wall of SC (see Figure S7). CD34 and LY6C1 were expressed in SC endothelial cells (yellow asterisks). Scale bars = 50 μm.

305 # TM subtypes differentially occupy TM zones

306

307 To further explore the sub-anatomical localization of the TM cell subtypes, we used a
308 combination of IF and ISH to identify subtype markers. Each TM cell subtype had a higher
309 percentage of cells expressing, and an increased average expression of, its respective subtype
310 markers (all $P < 1E\text{-}100$ compared to other TM cells, S7A Fig). To analyze the distribution of
311 subtypes, we first divided the TM into zones along its anterior/posterior and inner/outer axes
312 (S7B-E Fig). The total area of TM occupied by each individual subtype marker was assessed in
313 each zone on more than 150 tissue sections. This detected biases for the subtypes to be
314 differentially localized in specific TM zones (Fig 2A-F). For instance, TM1 cells were significantly
315 more frequent in the posterior and outer TM zones, while TM3 cells were overrepresented in the
316 anterior and inner zones (all $P < 0.01$). The different marker molecules that were assessed for
317 each TM cell subtype gave highly consistent results regarding zonal occupancy (S8A-B Fig, S9
318 Fig). In addition, we confirmed the localization biases in 3D whole mounts of the mouse limbus
319 (Fig 2G-H, TM1 – MYOC, TM3 – α-SMA) [25]. Collectively, these data indicate clear localization
320 biases that differ for the TM1 and TM3 subtypes.

321

322 To better understand the location of TM cell subtypes, we analyzed marker expression patterns
323 in 50-60 exceptionally high-quality sections for each marker of each TM cell subtype (see
324 Methods). For this analysis, the TM was divided into eight regions (S7F Fig). Not only did this
325 refine the localization bias of TM1 and TM3 cells, but it discovered that TM2 cells are most
326 concentrated in the mid-posterior two-thirds of the TM (mid regarding inner-outer axis, all $P <$
327 0.01, Fig 2I-K). Despite their biased distributions, some cells of each TM subtype were detected
328 in most TM regions.

329

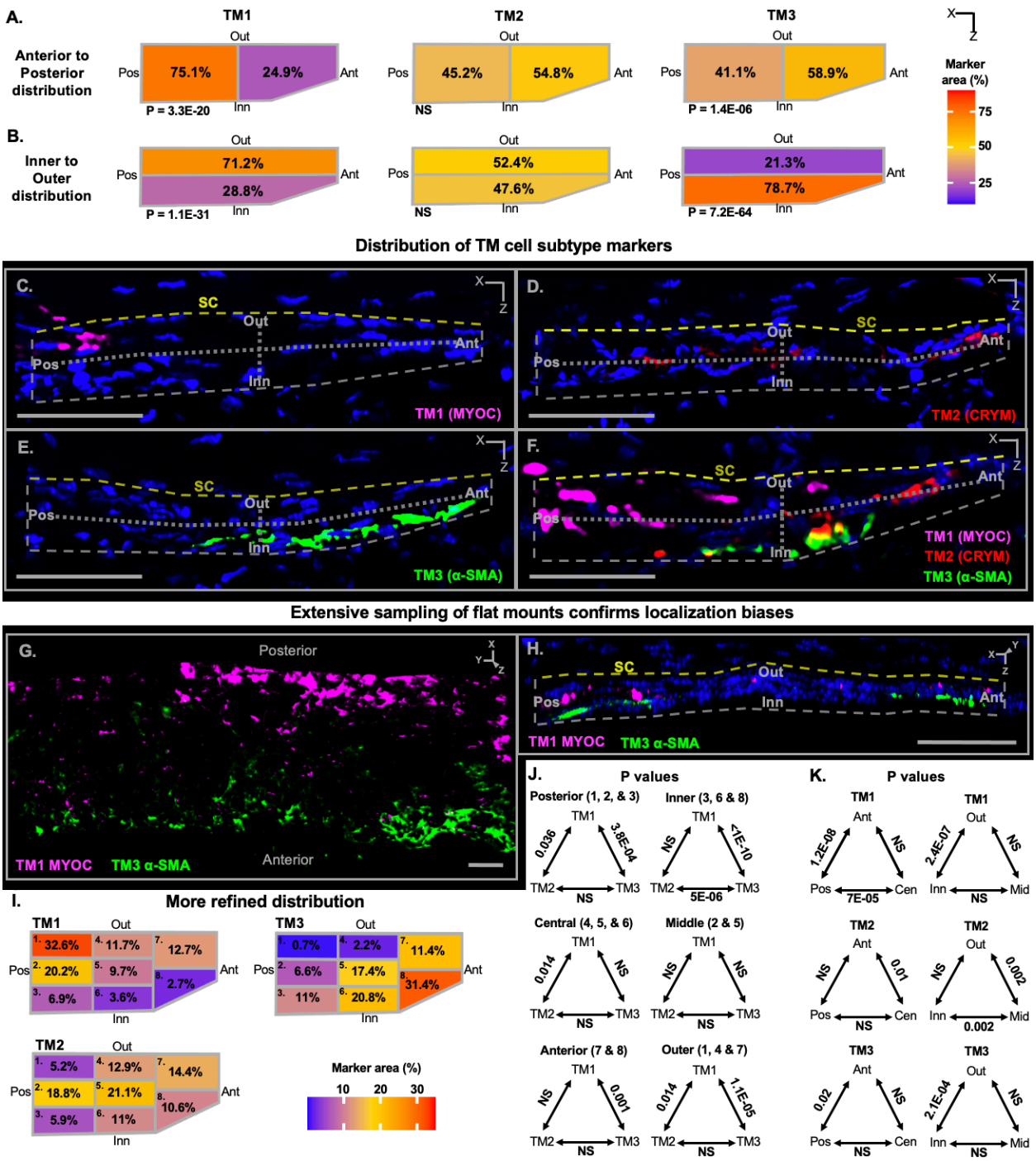

Fig 2. Biased localization of TM cell subtypes within the TM. (A-B) Summary diagrams showing the location of expression of TM1, TM2, and TM3 signature markers in the TM. For quantification of marker distributions, the TM was divided in half along both anterior-posterior (A) and inner-outer (B) axes (see Figure S7 localization of TM and SC). The area of the TM that

was positive for each marker within each region was calculated as a percentage of the total area occupied by that marker in the entire TM on each section. The percentage of marker localization to each region was averaged across all analyzed sections. The average localization across all markers used for each TM cell subtype (see S8 and S9 Figs) is shown on the diagrammatic representations of the TM using heatmaps. TM1 localization is biased towards the posterior and outer TM, whereas TM3 is biased towards the anterior and inner TM. No clear bias for TM2 was observed. A total of 286 sections were examined using immunofluorescence (IF) and in situ hybridization (ISH). Between 130-160 sections were examined for each TM cell subtype. **(C-F)** Representative sections for a subset of markers for each subtype used for quantification. See Figure S6 for explanation of indicated tissue orientations. **(G)** En face image of the TM in a 3D reconstruction of a tissue whole mount, clearly demonstrating the anterior vs posterior localization bias for TM1 (posterior bias) and TM3 (anterior bias) cell types. **(H)** Orthogonal 3D image that is cropped and oriented in the same planes as the tissue sections. The inner bias for α-SMA (*Acta2*, TM3) compared to an outer bias for MYOC (TM1) is evident. **(I)** More spatially refined analyses were subsequently conducted using extremely high-quality sections (50-60 per marker) by dividing the TM into 8 smaller zones (S7 Fig). In this more refined study, TM2 cells have a biased localization to a posterior and central region of TM (most enriched in zones 2 and 5, see Figure S7). **(J-K)** The TM subtype distributions were statistically compared across the combined zones (in parentheses) as indicated. ANOVA followed by Tukey's honestly significant difference test. Ant: anterior TM, Pos: posterior TM, Inn: inner TM, Out: outer TM, SC: Schlemm's canal. Grey dotted lines mark the TM zones, yellow dotted lines mark inner wall of Schlemm's canal. All scale bars: 50 μm.

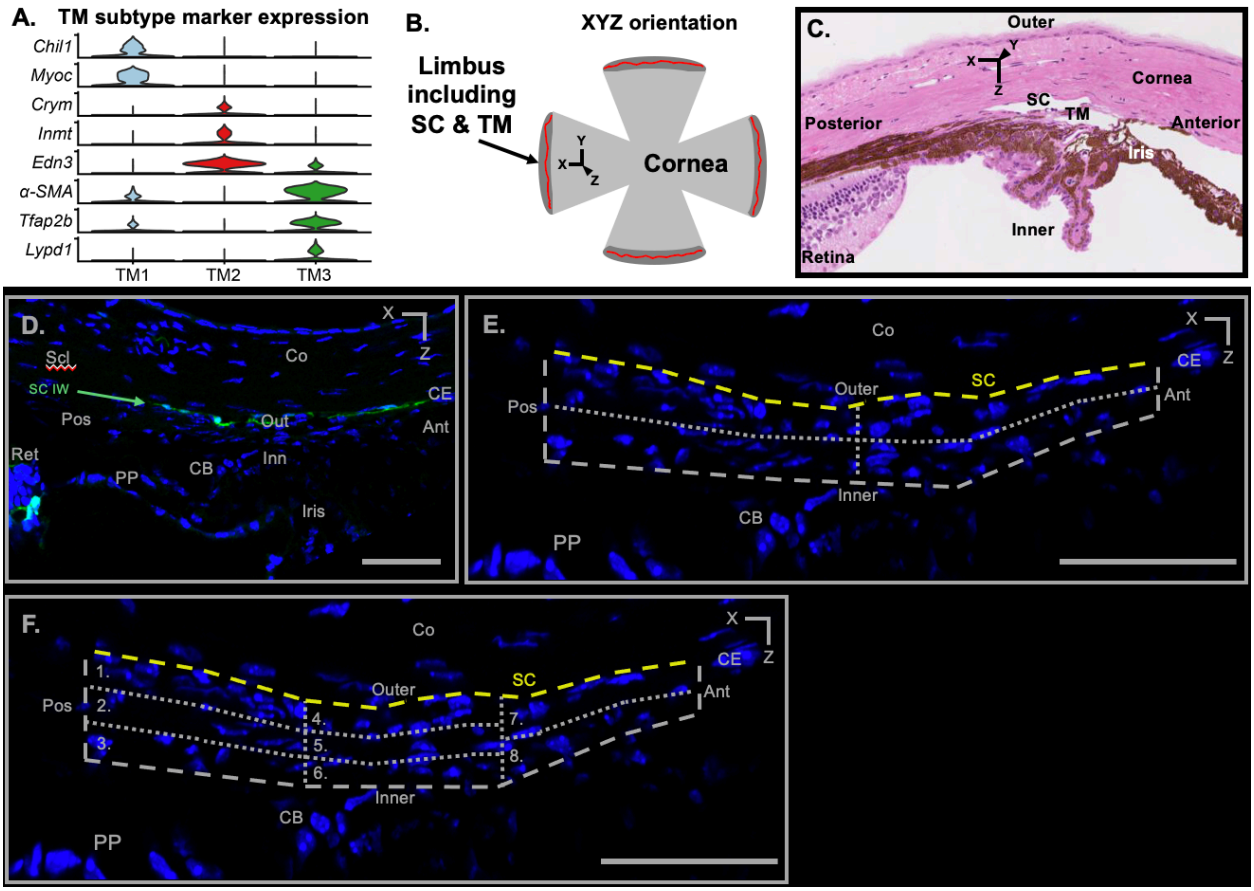

S7 Fig. Assessing zonal distribution of TM cell subtypes. (A) Violin plot showing expression of signature genes that were used to localize TM cell subtypes. **(B-C)** Diagram of flat-mounted anterior segment (B) and *hematoxylin and eosin-stained s*agittal section (C) indicating the X, Y and Z axis as used throughout this paper as previously reported (Kizhatil et al., 2014)**. (D-E)** Schlemm's canal (SC) inner wall was identified based on anatomy and the expression of *Prox*-GFP (green) and other endothelial cell markers. The pars plana (PP) and corneal endothelium (CE) were identified based on anatomy and DAPI staining. The posterior boundary of the TM begins just anterior to the PP and was typically aligned with the most posterior portion of SC. The anterior TM ends where the corneal endothelium begins. This typically aligned with the most anterior portion of SC. The outer boundary of the TM was immediately internal to the inner wall of SC. The inner-most TM was where the TM cells end abutting the anterior chamber. Using these boundaries, the anterior-posterior and inner-outer axis of the TM were measured.

374 Based on these measurements for each eye, the TM was divided in half along both the inner-
375 outer and anterior-posterior axes. (**F**) For more refined analysis, the anterior-posterior distance
376 was then divided into thirds to generate posterior, central, and anterior regions. Each of these
377 regions was then equally divided into their subregions as shown. Because the anterior TM is
378 thinner, it was divided into two zones. These divisions generate 8 TM zones. All scale bars: 50
379 μm.

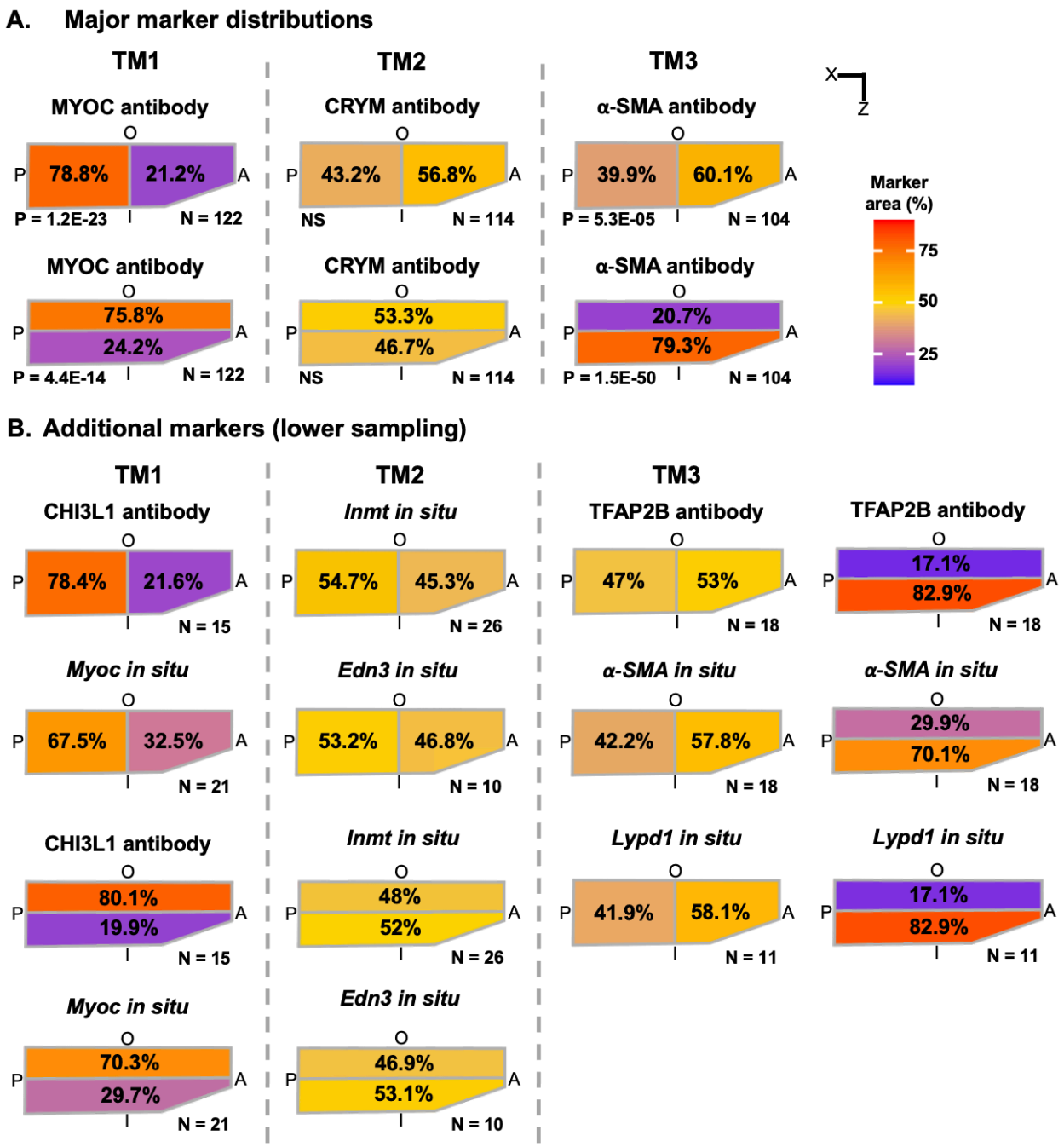

S8 Fig. Distribution of TM cell subtypes by marker. (A) Schematic representation of major marker distributions from Figure 2. **(B)** Additional markers for a given TM cell subtype had similar patterns of localization (see Figure S9 for example staining). However, these markers were not sampled deeply enough to perform statistical analysis. A: anterior TM, I: inner TM, O: outer TM, P: posterior TM.

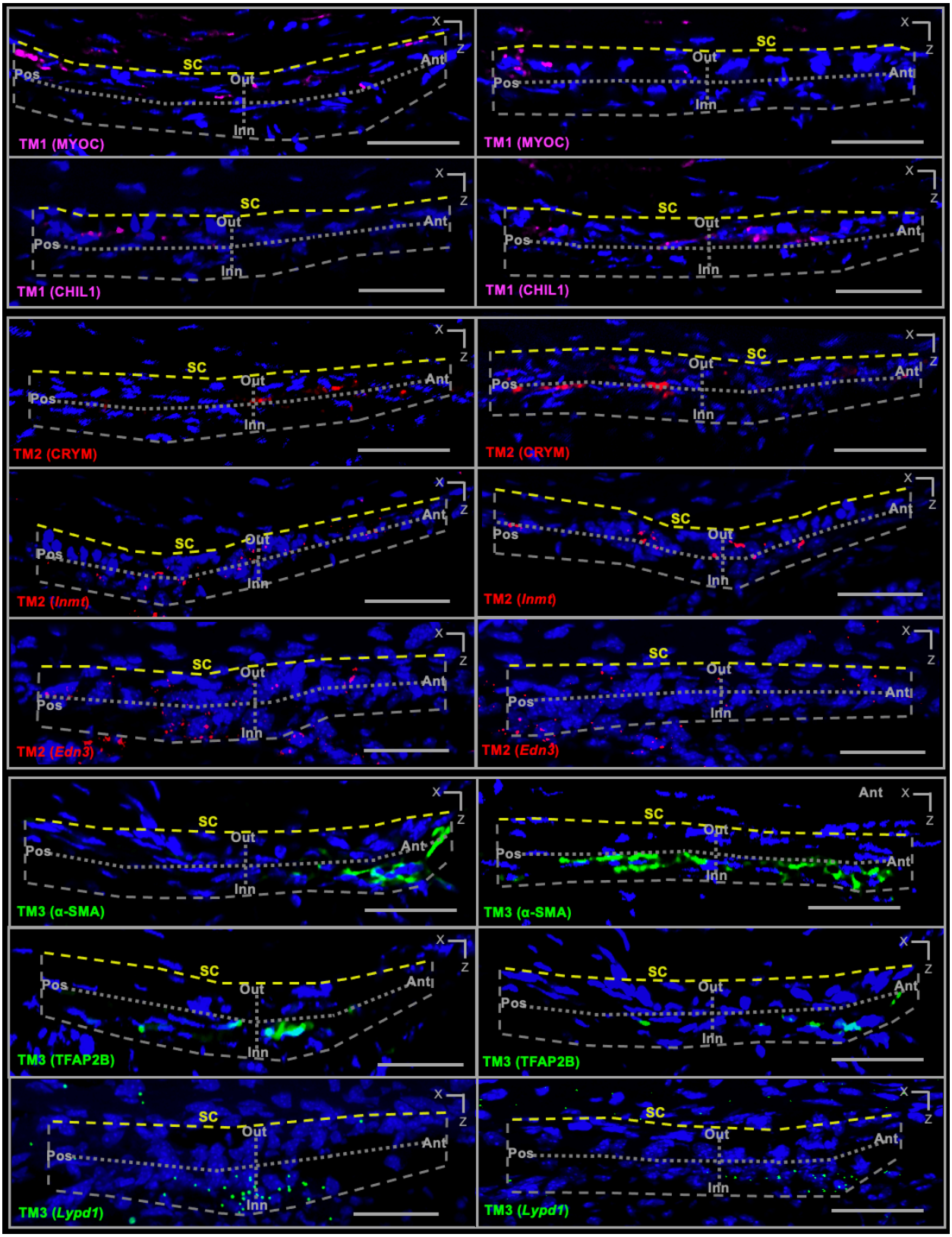
TM1 (MYOC)
TM1 (MYOC)
TM1 (CHIL1)
TM1 (CHIL1)
TM2 (CRYM)
TM2 (CRYM)
TM2 (Inmt)
TM2 (Inmt)
TM2 (Edn3)
TM2 (Edn3)
TM3 (α-SMA)
TM3 (α-SMA)
TM3 (TFAP2B)
TM3 (TFAP2B)
TM3 (Lypd1)
TM3 (Lypd1)
SC
Pos
Ant
Out
Inn
X
Z

388 **S9 Fig. Additional examples of TM subtype marker localization.** Although there is variability
389 in expression between sections, the aggregate of all sections reveals the biased distributions of
390 TM cell subtypes as summarized in Figures 2. Here we focus on TM expression. However,
391 some of the markers are also expressed outside of the TM. For examples, *Edn3* is expressed in
392 vasculature, while both *Lypd1* and *Inmt* are expressed at low levels in scleral and iris cells (but
393 are higher in TM cells). All scale bars: 50 μm. Markers assessed by IF: MYOC, CHIL1, CRYM,
394 α-SMA, TFAP2B. Markers assessed by ISH: *Inmt*, *Edn3*, *Lypd1*. All scale bars: 50 μm.
395
396
397
398
399
400
401
402
403
404
405
406
407
408
409
410
411

412 # Molecular comparison of TM cell subtypes

413

414 To determine the molecular functions of TM cells, we first conducted gene ontology (GO)
415 analysis using genes that were differentially expressed genes (DEGs) in all TM cells as a group
416 compared to other sequenced cells (S2 Table). Additionally, we used gene set enrichment
417 analysis (GSEA) to assess whether these GO pathways are relatively enriched or
418 underrepresented in TM cells. Compared to other cells, TM cells were enriched for pathways
419 associated with extracellular matrix (ECM) structure and function, including signaling associated
420 with collagens, proteases, integrins, and glycosaminoglycans (Fig 3A, S10A Fig, S3 Table). TM
421 cells were also enriched for growth factor signaling. Conversely, underrepresented pathways in
422 TM cells were associated with desmosomes, peroxisomes, and certain cytoskeletal and plasma
423 membrane elements. These pathways help define TM cells relative to other cells in the region.

424

425 Next, we compared TM cell subtypes to each other (Fig 3B-D). TM1 cells were most enriched
426 for ECM pathways, particularly structural components such as collagens, integrins, and other
427 ECM elements (Fig 3B, S10B Fig). The expression of several ECM genes that are reported to
428 impact IOP are heightened in TM1 cells, including Type VIII collagens, fibronectin, and *Ltbp2*
429 [53-55]. Both TM1 and TM2 cells have enriched expression of glycosaminoglycan (GAG) genes
430 (Fig 3B-C, S10B-C Fig). GAGs in the JCT and intertrabecular spaces form a gel-like
431 consistency and changes in GAG abundance correlate with altered AH outflow resistance [56-
432 58]. TM2 cells are uniquely enriched for the laminin complex, a key component of basement
433 membranes [59]. Pathways related to clearing debris and monitoring the extracellular
434 environment including phagocytic vesicles, antigen presentation, and lysosomal function are
435 also enhanced in TM2 cells. In contrast, TM3 cells are underrepresented for ECM-related
436 pathways compared to other TM cells but are enriched for pathways related to actin binding and

437 mitochondrial metabolism (Fig 3D, S10D Fig). The actomyosin system plays a crucial role in
438 maintaining TM cell contractility and in regulating outflow facility [16-20]. The enrichment of
439 mitochondrial metabolism pathways in TM3 cells emphasizes their energetic needs and their
440 expected heightened susceptibility to genetic and environmental contexts that compromise
441 metabolic functions. Importantly, genetic variation in mitochondrial/ metabolic pathways
442 contributes risk for IOP elevation and glaucoma [60-62].
443
444 We next compared growth factor signaling and ligand-target interactions between TM cells
445 subtypes and other cells. TM1 cells were enriched for transforming growth factor beta (TGF-β)
446 pathway signaling (Fig 3B). Receptor ligand activity was enriched in TM2 cells while the
447 membrane raft pathway (a site of signal transduction) was enriched in TM3 cells (Fig 3C-D).
448 Next, we used LRLoop [63], which was developed based on NicheNet [64], to predict significant
449 ligand-target interactions between TM cells and other local endothelial cells that are relevant to
450 AH drainage (Figure 4A-D). TGF-β ligands (*Tgfb1*, 2, & 3) were predominantly expressed in
451 TM1 cells. By contrast, TM2 cells expressed molecules critical for vascular function, such as
452 *Angpt1*, *Vegfa*, and *Edn3* (S11A-D Fig) [65-67]. These TM-secreted molecules have been
453 directly associated with SC maintenance and IOP [68-71].
454

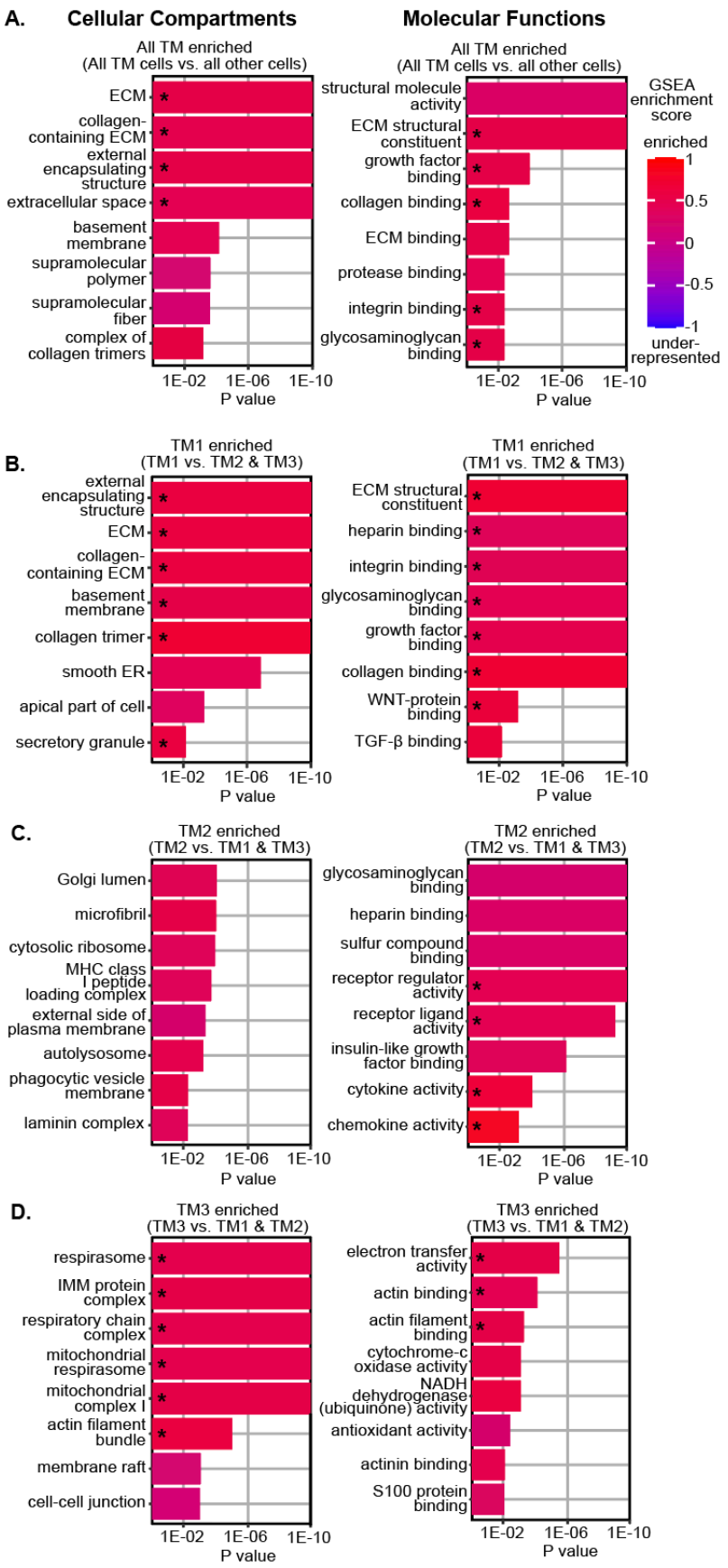
A.
Cellular Compartments
Molecular Functions
All TM enriched
(All TM cells vs. all other cells)
ECM
collagen-containing ECM
external encapsulating structure
extracellular space
basement membrane
supramolecular polymer
supramolecular fiber
complex of collagen trimers
structural molecule activity
ECM structural constituent
growth factor binding
collagen binding
ECM binding
protease binding
integrin binding
glycosaminoglycan binding
GSEA enrichment score
enriched
1
0.5
0
-0.5
-1
under-represented
1E-02
1E-06
1E-10
P value
B.
TM1 enriched
(TM1 vs. TM2 & TM3)
external encapsulating structure
ECM
collagen-containing ECM
basement membrane
collagen trimer
smooth ER
apical part of cell
secretory granule
ECM structural constituent
heparin binding
integrin binding
glycosaminoglycan binding
growth factor binding
collagen binding
WNT-protein binding
TGF-β binding
C.
TM2 enriched
(TM2 vs. TM1 & TM3)
Golgi lumen
microfibril
cytosolic ribosome
MHC class I peptide loading complex
external side of plasma membrane
autolysosome
phagocytic vesicle membrane
laminin complex
glycosaminoglycan binding
heparin binding
sulfur compound binding
receptor regulator activity
receptor ligand activity
insulin-like growth factor binding
cytokine activity
chemokine activity
D.
TM3 enriched
(TM3 vs. TM1 & TM2)
respirasome
IMM protein complex
respiratory chain complex
mitochondrial respirasome
mitochondrial complex I
actin filament bundle
membrane raft
cell-cell junction
electron transfer activity
actin binding
actin filament binding
cytochrome-c oxidase activity
NADH dehydrogenase (ubiquinone) activity
antioxidant activity
actinin binding
S100 protein binding

455

456 **Fig 3. Pathway analysis suggests differential involvement of TM cell subtypes in**
457 **extracellular matrix regulation, growth factor signaling, and actin-binding**
458 **(A-B)** Molecular comparison of all three TM cell subtypes to all other sequenced cells using
459 gene ontology (GO) of differentially expressed genes (DEGs). The top five most significant
460 pathways as well as three additional pathways of interest are shown for each indicated
461 comparison (adjusted P values, X-axis was cutoff at P < 1E-10). GSEA analysis was also used
462 to assess the enrichment or underrepresentation of these GO pathways with GSEA scores color
463 coded on the GO charts above. Pathways significantly different by GSEA analysis are indicated
464 by asterisks. Overall, TM cells have over-representation of various extracellular matrix (ECM)
465 molecules/ pathways including collagens, glycosaminoglycans, and integrins compared to non-
466 TM cells. Growth factor signaling is also enriched in TM cells compared to other cell types. **(C-**
467 **D)** When comparing TM cell subtypes, TM1 cells are further enriched for ECM molecules such
468 as collagens, glycosaminoglycans, and integrins as well as TGF-β signaling. **(E-F)** TM2-
469 enriched ECM pathways include glycosaminoglycan binding and the laminin complex. TM2 cells
470 are also enriched for receptor-ligand signaling and insulin growth factor binding. **(G-H)** Actin-
471 binding and mitochondrial metabolism genes are enriched in TM3 cells. ECM = extracellular
472 matrix. ECS = extracellular structure. ER = endoplasmic reticulum. IMM = inner mitochondrial
473 membrane.
474
475
476
477

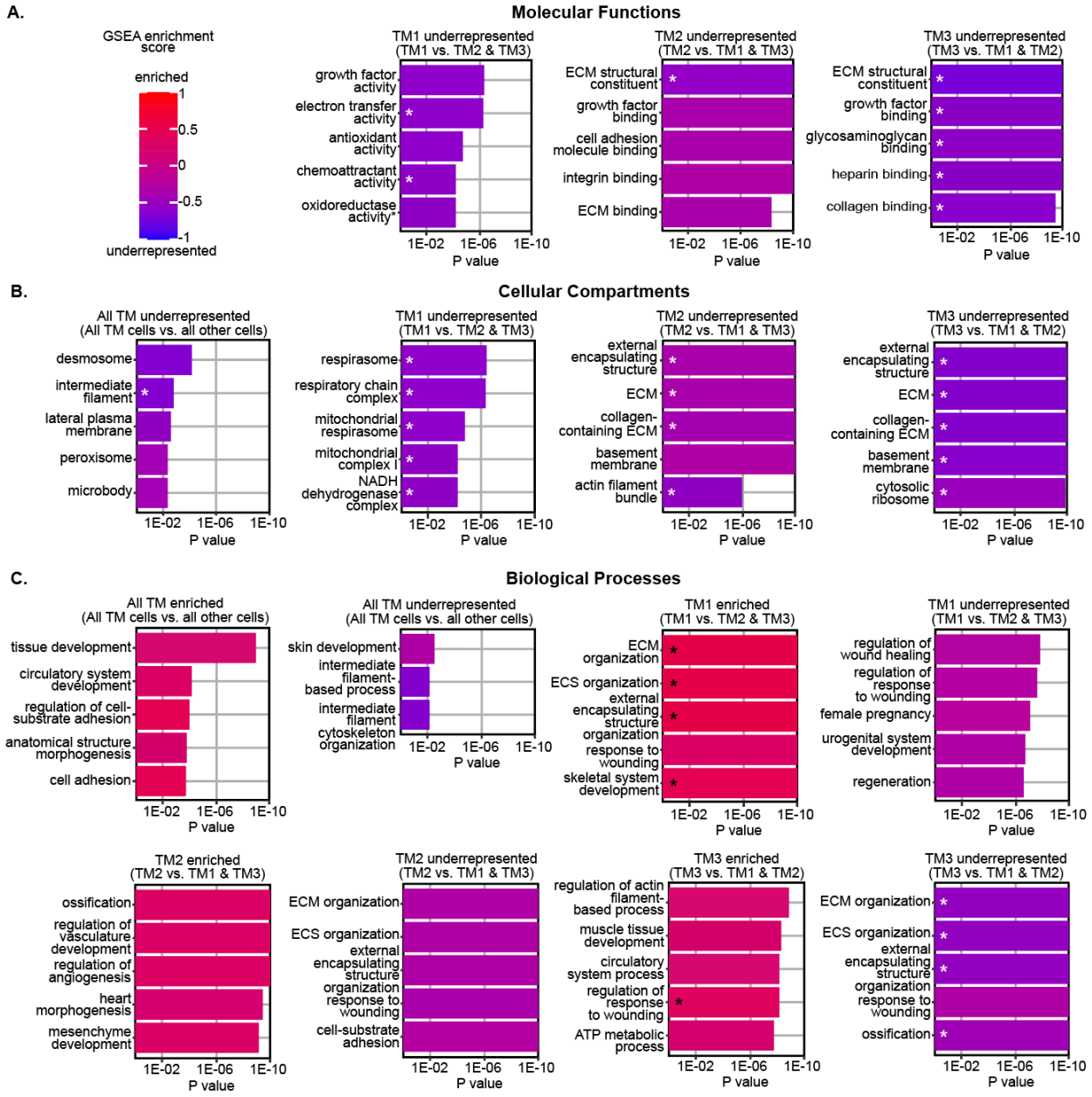

S10 Fig. TM cell pathway analysis. (A-C) Additional analyses showing the most significant pathways (by gene ontology (GO) analysis. Pathways are further separated into enriched or underrepresented categories based on gene set enrichment analysis (GSEA) score. Asterisks indicate pathways that are significantly enriched or underrepresented based on GSEA score. ECM = extracellular matrix. ECS = extracellular structure.

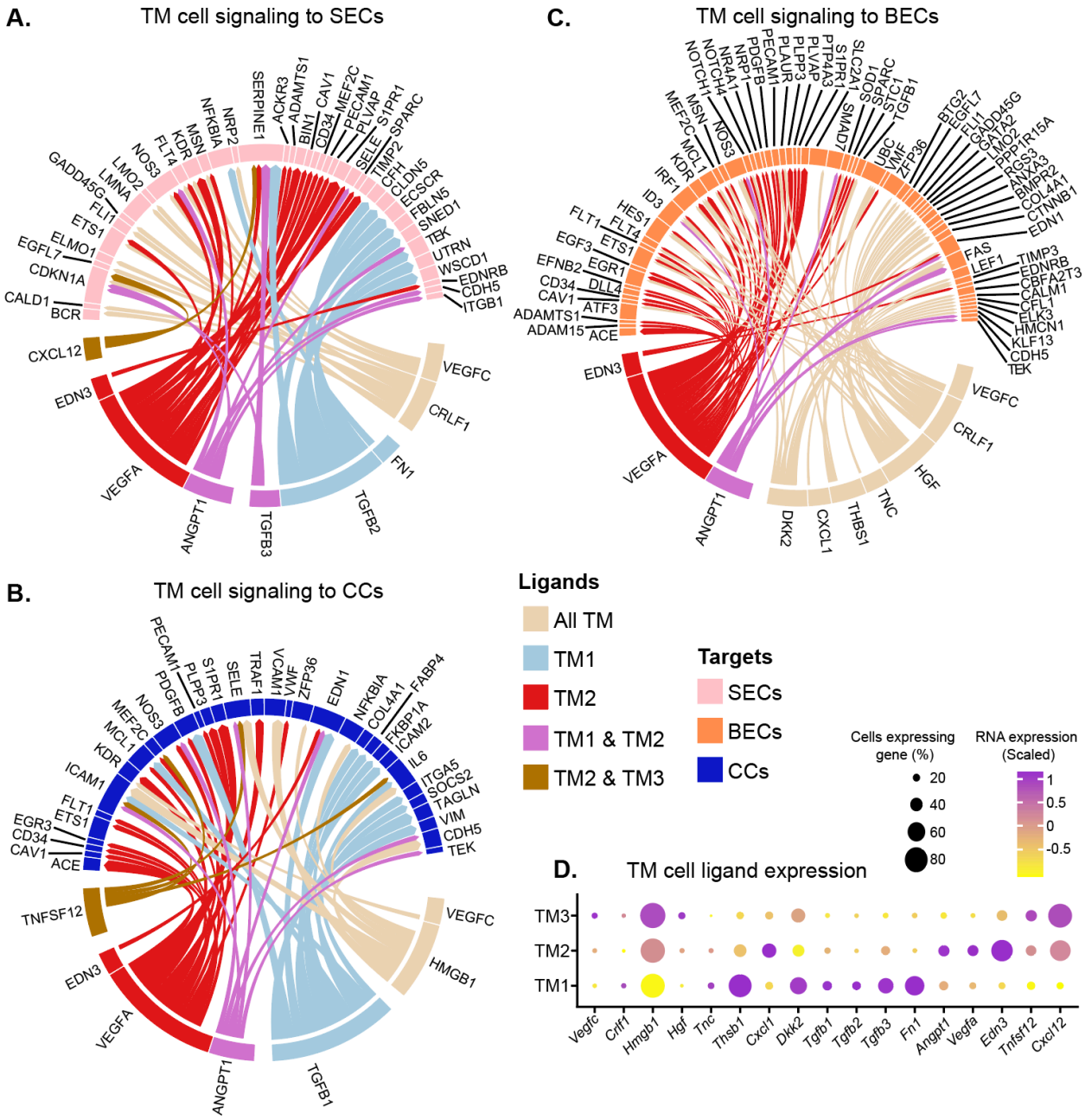

Fig 4. Signaling interactions directed from TM cells to Schlemm's canal and vascular endothelial cells differ across TM subtypes. (A) Circos plot showing the top predicted interactions between TM cell ligands and Schlemm's canal endothelial (SEC) target molecules. The top predicted targets in all TM cells are split by their expression across subtypes. TM1 and TM2 participate in more predicted signaling events compared to TM3. TM1-biased ligands include members of the *Tgf-β* and fibronectin signaling families. Various endothelial trophic

493 factors are predominantly expressed in TM2 including endothelin 3, vascular endothelial growth
494 factor A, and angiopoietin 1. See Table S4 for comprehensive list of ligand-target interaction
495 data. **(B-C)** TM cell ligands that signal to collector channel (CC) endothelial cells (B) or blood
496 endothelial cells (BECs, C). **(D)** The expression of all ligands predicted to have signaling
497 interactions with SECs, CCs, or BECs, are displayed across TM cell subtypes (Dot plot).
498
499

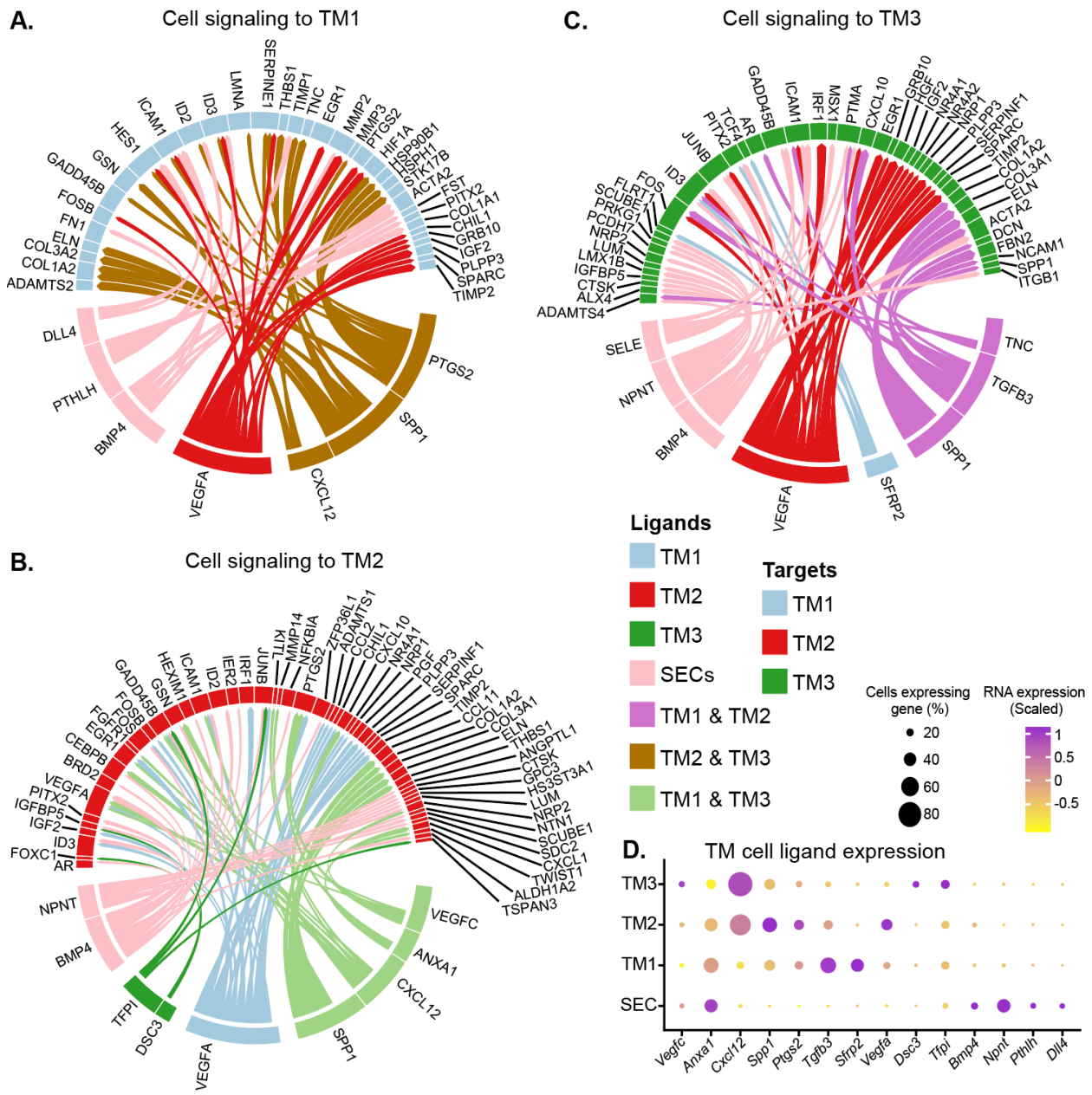

S11 Fig. TM-TM and SEC-TM signaling. (A-C) Analyses showing the top predicted interactions between TM and Schlemm's canal endothelial (SEC) ligands and individual TM cell target molecules (Circos plots). The three plots show target molecules in each individual TM cell subtype respectively. **(D)** The expression of all ligands predicted to have signaling interactions with TM cell subtypes (Dot plot).

507 ## Comparison to human TM cells

508

509 We next worked to relate our findings to human data. We compared marker genes for each of
510 our TM cell subtypes to sequenced human TM cells from two previous studies [31, 33]. These
511 previous studies differed in the number of human TM cell subtypes that they reported and in the
512 identities of their clusters. Van Zyl et al. identified three TM cell subtypes that they called JCT,
513 beam A, and beam B [31], whereas Patel et al. identified two subtypes that they called
514 fibroblast-like and myofibroblast-like [33]. TM1 marker genes were most enriched in Van Zyl et
515 al's human JCT cells (S12A Fig). Similarly, *Dcn* was expressed in mouse TM1 cells and was
516 localized to fibroblast-like TM cells adjacent to SC by Patel et al. TM1 cell nuclei were typically
517 shorter with greater sphericity than the elongated endothelial-like nuclei of TM3 cells (S13A-D
518 Fig). This nuclear morphology was more consistent with a JCT than beam cell identity.
519 Together, these data support a JCT identity for TM1 cells. TM2 cells were more closely related
520 to human beam A and beam B cells than to the JCT cells reported by Van Zyl et al (S12B Fig).
521 TM2 cells also shared expression of the *RSPO2* marker gene with the human myofibroblast-like
522 cells reported by Patel et al. Together, this suggests that TM2 cells are myofibroblast-like beam
523 cells. TM3 cells also shared marker genes with Patel et al's myofibroblast-like cells (*TAGLN* and
524 *ACTA2*), suggesting TM3 cells are also beam cells. There was relatively equal TM3 marker
525 gene enrichment across all human TM cell subtypes of Van Zyl et al (S12C Fig). Nuclei
526 immediately adjacent to TM2 and TM3 cell marker staining had an elongated, endothelial-like
527 shape (S13A-C Fig). This nuclear morphology was also consistent with the location of TM2 and
528 TM3 cells on beams and analogous to the endothelial-like morphology of human beam cells [2].
529

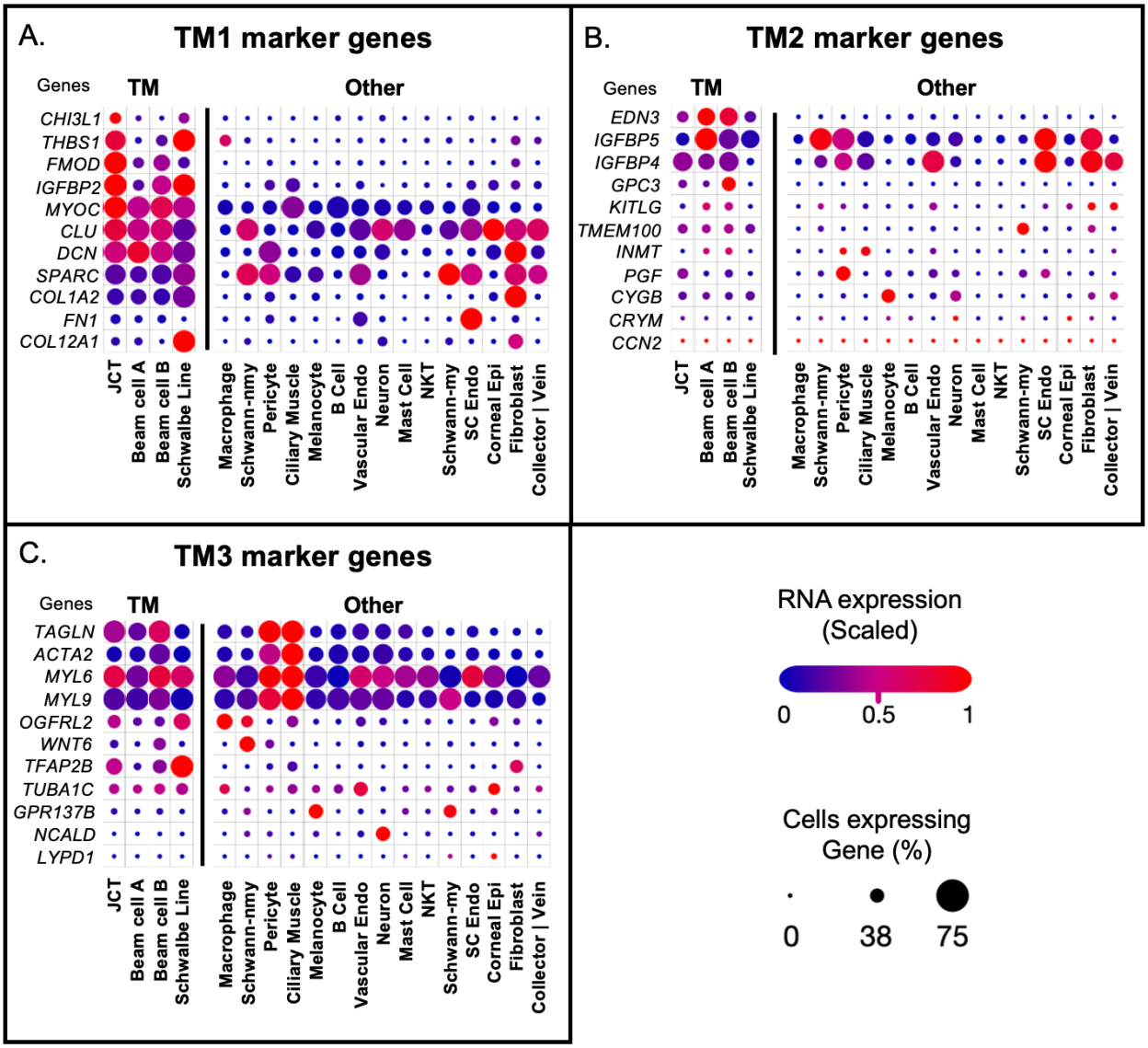

S12 Fig. Mouse TM subtype marker expression in human TM cells. (A-C) Dot plots of the expression of the top 11 marker genes for each of our mouse TM cell subtypes that have human orthologues expressed in the Van Zyl et al human dataset. TM1 marker genes generally have higher expression in the human JCT cluster than in any other cluster of cells. Other than EDN3, TM2 and TM3 marker genes do not show a strong enrichment for the annotated TM cells compared to other cells. Among TM cells, TM2 marker genes are more enriched in beam A and beam B cells. TM3 markers are mostly expressed in relatively equal levels across all the human TM cells. Schwalbe's line cells are also similar to TM. The anterior insertion of the TM is near

539 Schwalbe's line, where TM stem cells are reported to reside. Therefore, the Schwalbe's line
540 cells maybe TM stem cells.
541
542
543
544
545
546
547
548

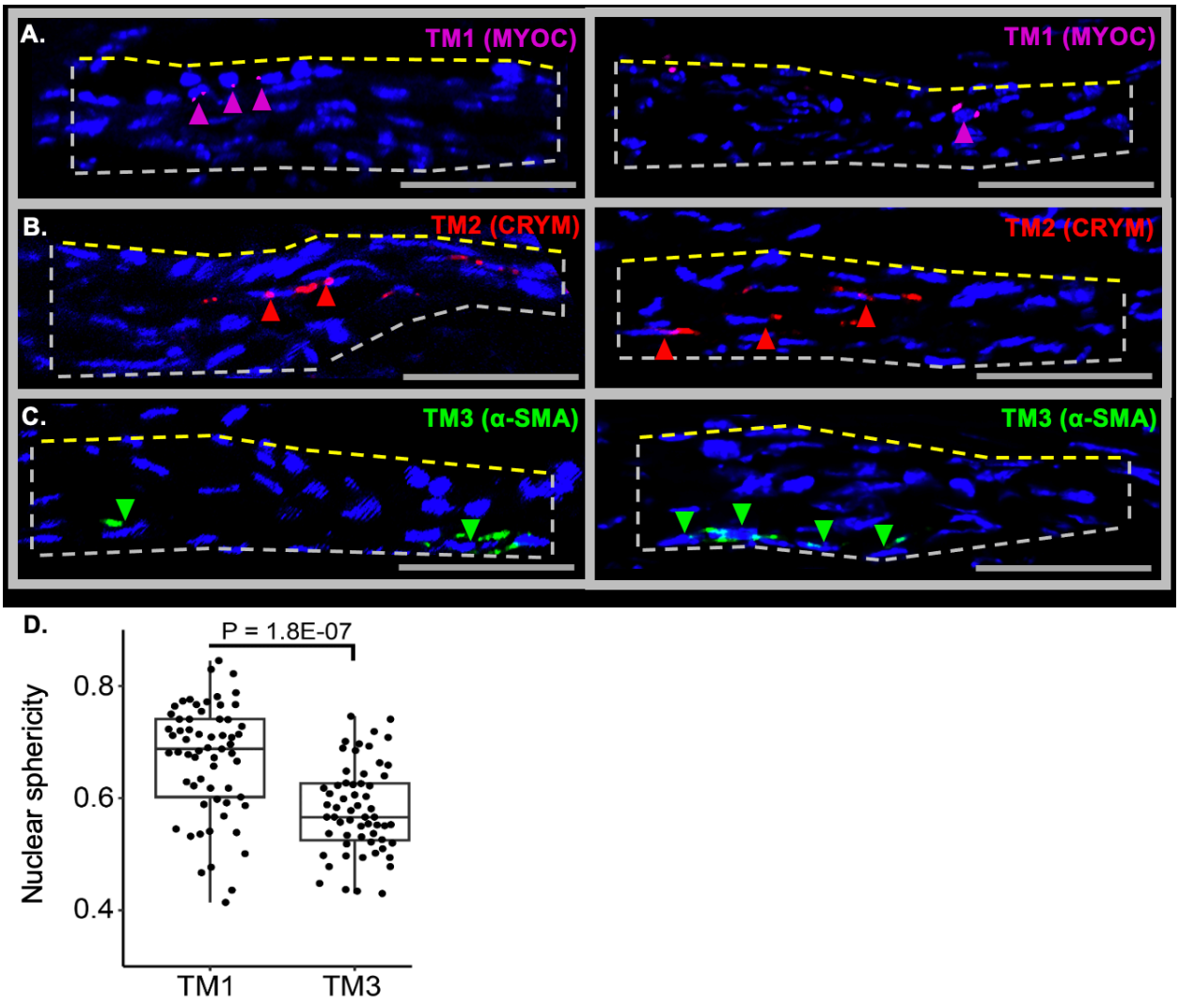

S13 Fig. Nuclear morphology of each TM subtype. (A-C) 2D section view of TM cell subtype nuclei. TM1 nuclei adjacent to the SC appear shorter than TM2 and TM3 nuclei and lack the typical elongated, endothelial-like morphology of beam cells. This shorter morphology gives TM1 nuclei a more spherical appearance. All scale bars: 50 μm. **(D)** To rigorously assess whether TM1 nuclei are more spherical, we analyzed their reconstructed 3D shapes from whole mounts images by confocal microscopy, comparing them to TM3 nuclei using the 'Sphericity' tool in Imaris. The data show that TM1 cells indeed have more spherical nuclei, consistent with a JCT identity. However, some TM1 cells exhibit more elongated nuclei, especially when located further from the SC. A higher sphericity score indicates a more rounded nucleus (with a

559 completely spherical shape scoring 1). We characterized 60 randomly selected nuclei for each
560 TM cell subtype. Groups were compared using Student's t-test.
561
562
563
564
565
566
567
568
569
570
571
572
573
574
575
576
577
578
579
580
581
582
583

584 Next, we evaluated the expression of genes implicated in elevated IOP and glaucoma by
585 genome-wide association studies (GWAS). TM1 and TM2 cells had similar expression levels of
586 GWAS genes associated with IOP elevation and primary open-angle glaucoma (POAG)
587 respectively (S14A Fig). TM3 cells had slightly less expression of these GWAS genes compared
588 to TM1 and TM2. To better understand the genes driving GWAS gene enrichment in different
589 TM subtypes, we studied pathways that are significantly enriched for GWAS genes (S14B-C
590 Fig, see Table S5 for complete list). TM1 cells were the most enriched for genes involved in
591 ECM organization, cell-substrate adhesion, and growth factor stimulus (S14D Fig). All 3 TM
592 subtypes had similar expression of GWAS genes associated with hormone stimulus, *Vegf*
593 signaling, and *Rho* kinase signaling. TM3 cells expressed lipid and carbohydrate mitochondrial
594 metabolism pathway genes at higher expression levels and in more cells than did TM1 and TM2
595 cells (S14E Fig). The same was true for actin binding-associated GWAS genes in TM3 cells
596 versus TM1 and TM2. Genetic variation in lipid and carbohydrate mitochondrial metabolism
597 pathways is associated with IOP elevation and glaucoma [61].
598

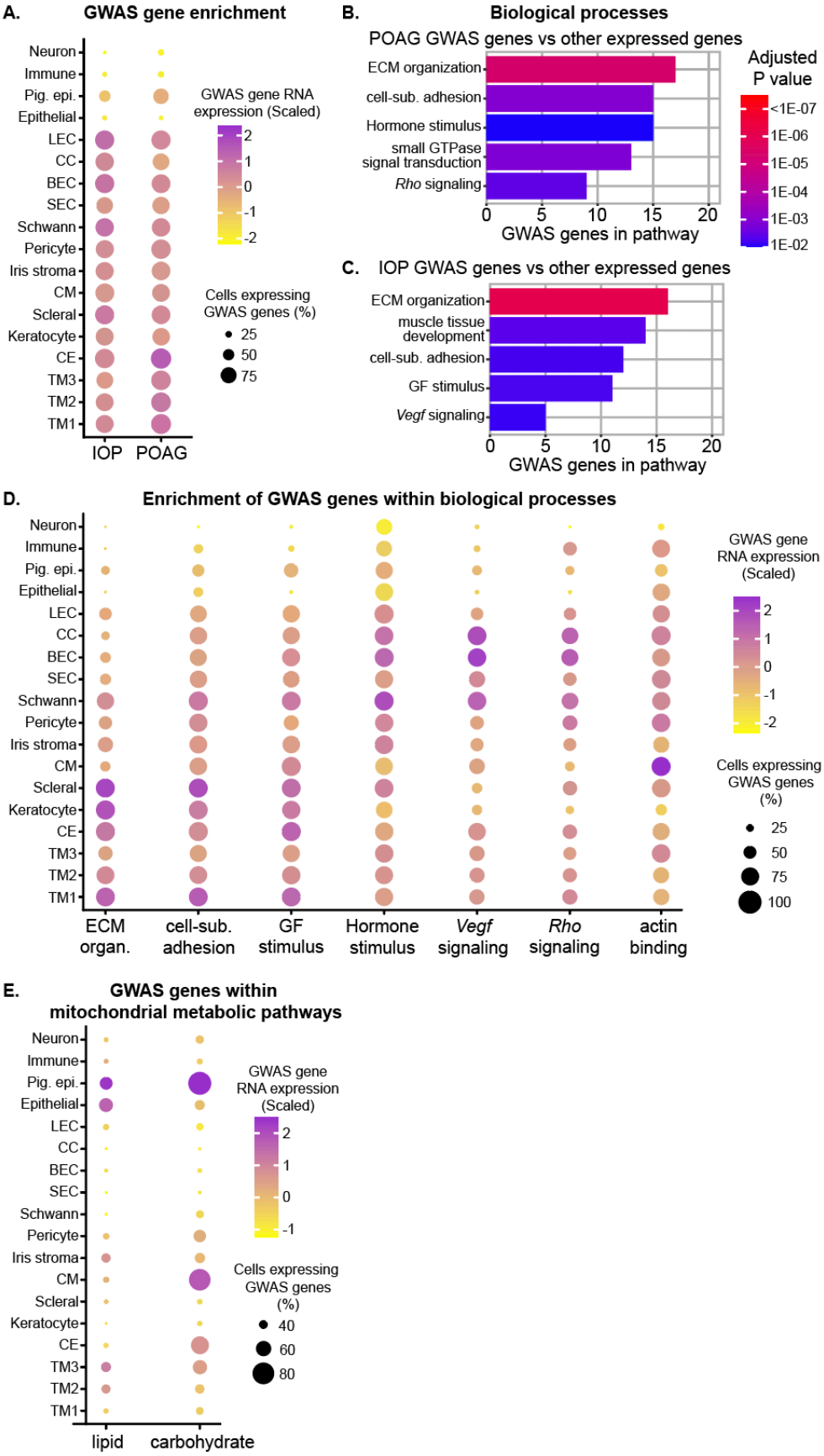
A.
GWAS gene enrichment
Neuron
Immune
Pig. epi.
Epithelial
LEC
CC
BEC
SEC
Schwann
Pericyte
Iris stroma
CM
Scleral
Keratocyte
CE
TM3
TM2
TM1
IOP
POAG
GWAS gene RNA expression (Scaled)
2
1
0
-1
-2
Cells expressing GWAS genes (%)
25
50
75
B.
Biological processes
POAG GWAS genes vs other expressed genes
ECM organization
cell-sub. adhesion
Hormone stimulus
small GTPase signal transduction
Rho signaling
0
5
10
15
20
GWAS genes in pathway
Adjusted P value
<1E-07
1E-06
1E-05
1E-04
1E-03
1E-02
C.
IOP GWAS genes vs other expressed genes
ECM organization
muscle tissue development
cell-sub. adhesion
GF stimulus
Vegf signaling
0
5
10
15
20
GWAS genes in pathway
D.
Enrichment of GWAS genes within biological processes
Neuron
Immune
Pig. epi.
Epithelial
LEC
CC
BEC
SEC
Schwann
Pericyte
Iris stroma
CM
Scleral
Keratocyte
CE
TM3
TM2
TM1
ECM organ.
cell-sub. adhesion
GF stimulus
Hormone stimulus
Vegf signaling
Rho signaling
actin binding
GWAS gene RNA expression (Scaled)
2
1
0
-1
-2
Cells expressing GWAS genes (%)
25
50
75
100
E.
GWAS genes within mitochondrial metabolic pathways
Neuron
Immune
Pig. epi.
Epithelial
LEC
CC
BEC
SEC
Schwann
Pericyte
Iris stroma
CM
Scleral
Keratocyte
CE
TM3
TM2
TM1
lipid
carbohydrate
GWAS gene RNA expression (Scaled)
2
1
0
-1
Cells expressing GWAS genes (%)
40
60
80

599

600 **S14 Fig: GWAS gene expression in limbal cells. (A)** Expression of genes implicated in risk
601 for IOP elevation (left) and primary open-angle glaucoma (POAG, right) in humans GWAS
602 plotted against mouse limbal cell type. There is similar GWAS gene expression across TM cell
603 subtypes and other limbal cell types. TM1 and TM2 have a slightly higher expression of GWAS
604 genes compared to TM3. **(B-C)** Pathway analysis (Gene ontology, GO) shows enrichment of
605 biological pathways for the POAG (B) or IOP (C) genes vs other expressed genes considering
606 all cell types (see Table S5 for full list of GWAS gene-enriched pathways). **(D)** Enriched
607 biological pathways among POAG GWAS genes within the indicated cell types. **(E)** Cell type
608 enrichment of lipid and carbohydrate metabolism pathway genes that are significantly
609 associated with POAG (Khawaja et al.). ECM organ. = extracellular matrix organization, cell-
610 sub. = cell-substrate adhesion, Hormone stimulus = cellular response to hormone stimulus,
611 small GTPase signal transduction = regulation of small GTPase mediated signal transduction,
612 *Rho* signaling = regulation of Rho protein signal transduction, GF stimulus = regulation of
613 cellular response to growth factor stimulus, *Vegf* signaling = vascular endothelial growth factor
614 receptor signaling pathway.
615
616
617
618
619
620
621
622
623
624
625

626 # Regulation of TM cell gene expression

627

628 To better understand the overlap and differences in transcriptional control of TM cell gene
629 expression, we performed single-cell resolution multiome sequencing. Using limbal strip tissue
630 isolated from a separate cohort of mice than those used for scRNA-seq, we simultaneously
631 performed both single nucleus RNA sequencing (snRNA-seq) and snATAC-seq. We thus
632 captured both gene expression and open chromatin data throughout the genome in the same
633 cell. Using the snRNA-seq data, we clustered cells into various cell types. The generated
634 clusters and their marker genes generally agreed with our scRNA-seq analyses (Fig 5A-B,
635 S15A Fig). Notably, there was a significant correlation between gene expression (RNA-based
636 clustering) and chromatin accessibility (ATAC-based clustering) with adjusted Rand index of
637 0.20 ($p < 0.001$, permutation test, S15B-D Fig). This included an increase in chromatin
638 accessibility at the promoters of marker genes in their respective TM cell subtypes (Fig 5C-E).
639 To discover the key transcriptional regulators within TM cells, we examined the correlation
640 between the expression of each transcription factor (TF) and their chromatin accessibility at
641 predicted binding sites within all TM cells. Various TFs that either activated or repressed
642 transcriptional activity exhibited good correlations with gene expression across TM cells (Fig
643 5F). Such activating TFs include *Tcf21*, *Arid3b*, and *Myc*, while repressing TFs include *Meox2*,
644 *Junb*, and *Sox6*. Notably, *LMX1B*, an important gene in glaucoma GWAS [28, 34-38], is among
645 the most strongly activating TFs in TM cells.

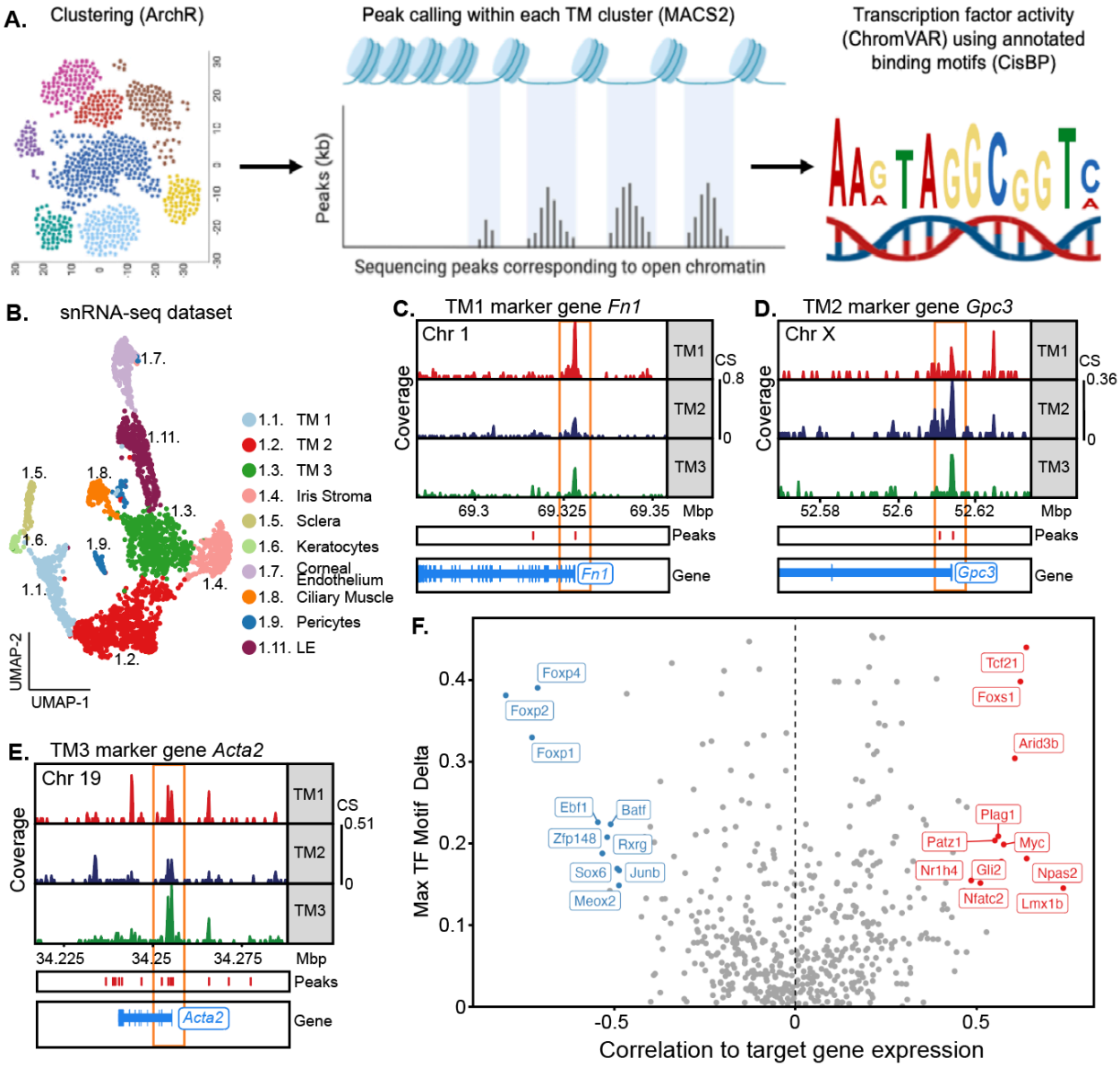

Fig 5. Transcription factors dictating gene expression in TM cells (A) A schematic representation of the pipeline used to identify open chromatin sites and active transcription factors (TFs). Individual cells were profiled using both single nucleus (sn) RNA and ATAC sequencing (multiome). TM cell clusters were identified using the snRNA-seq data, while significantly open chromatin regions were identified using the snATAC-seq data. Active TFs were determined based on the odds ratio of TF binding motifs within these open chromatin regions. Schematic created with BioRender.com **(B)** UMAP of subclusters derived from TM cell

654 containing cluster (cluster 1) in the snRNA-seq data. **(C-E**) Example ATAC tracts for the
655 promotor regions of selected marker genes for TM1 (C), TM2 (D), and TM3 (E). Each of these
656 marker genes has greater promoter accessibility in the TM cell subtype in which its RNA
657 expression is enriched (orange box). The aligned marker gene positions are shown. Coverage =
658 normalized ATAC signal reads in transcription start site. CS = coverage scale. **(F)** Correlations
659 between RNA expression levels (snRNA-seq dataset) of each TF and the chromatin
660 accessibility levels (snATAC-seq dataset) of their respective predicted target binding motifs
661 across all TM cell subtypes (see Methods). Select TFs with strong positive (red) or negative
662 correlations (blue) are named.

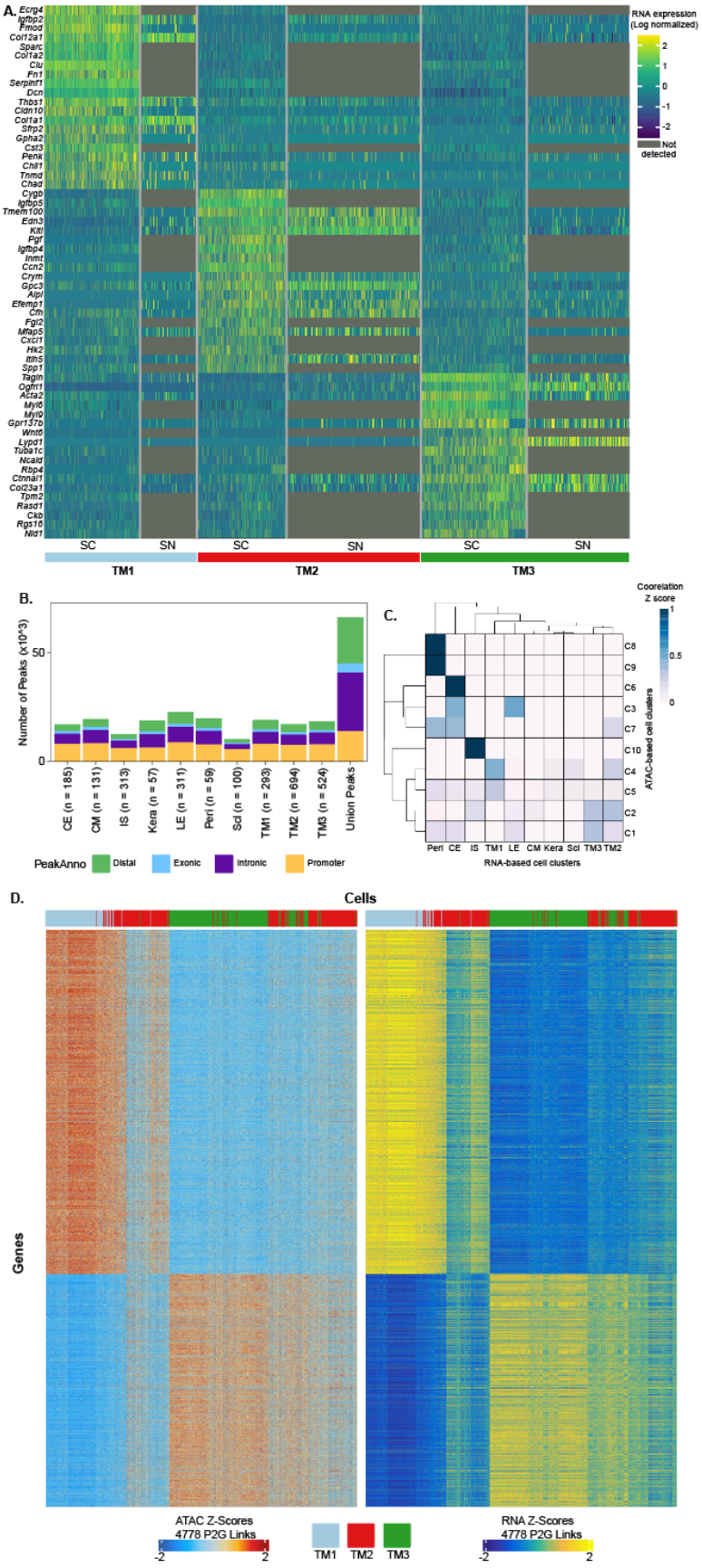
A.
RNA expression (Log normalized)
Not detected
SC
SN
TM1
TM2
TM3
B.
Number of Peaks (x10^3)
CE (n = 185)
CM (n = 131)
IS (n = 313)
Kera (n = 57)
LE (n = 311)
Peri (n = 59)
Scl (n = 100)
TM1 (n = 293)
TM2 (n = 694)
TM3 (n = 524)
Union Peaks
PeakAnno
Distal
Exonic
Intronic
Promoter
C.
Coorelation Z score
ATAC-based cell clusters
RNA-based cell clusters
D.
Cells
Genes
ATAC Z-Scores 4778 P2G Links
RNA Z-Scores 4778 P2G Links

663

S15 Fig. Analysis of ATAC dataset (A) Overlap of marker gene expression for each TM cell subtype between single-cell (sc) and single-nucleus (sn) RNA sequencing (RNA-seq). Other than the expected technical drop out of genes (no detected expression) in the snRNA-seq dataset, there is general agreement. **(B)** Localization of significantly open chromatin regions (snATAC-seq). **(C)** Confusion matrix of clusters identified by snRNA-seq and snATAC-seq after separately clustering each data type using unbiased dimensional reduction. Colors indicate the fraction of cells identified in each ATAC cluster (row) which are also identified in each RNA cell type (columns), where darker colors represent stronger correspondence between RNA and ATAC clusters. There is a significant correlation between gene expression (RNA-based clustering) and chromatin accessibility (ATAC-based clustering) with adjusted Rand index of 0.20 ($p < 0.001$, permutation test). **(D)** Heatmaps comparing the open chromatin score at a gene promoter (left panel, snATAC-seq) to the RNA expression (right panel, snRNA-seq). Individual genes are represented on the y-axis and individual cells are plotted on the x-axis (only TM cells included). The consistent heatmap patterns indicate a strong overlap between promoter chromatin states and RNA expression for individual genes across cell types, validating the quality of these multiome datasets.

688 # Metabolism-supporting treatment lessens IOP elevation in

689 # *Lmx1b*^{V265D} mice

690

691 To evaluate the utility of our new TM cell atlas, we used it to examine how *Lmx1b* mutations
692 affect the TM cell transcriptome and to identify potential mechanisms underlying IOP elevation.
693 We selected LMX1B because it causes IOP elevation and glaucoma in humans and was
694 identified as a highly active transcription factor in our TM cell dataset. To do this, we analyzed
695 scRNA-seq data generated for limbal cells from mice with a dominant mutation in *Lmx1b*
696 (*Lmx1b*$^{V265D/+}$), which included 2,491 *Lmx1b* mutant TM cells. These mutant C57BL/6J mice
697 develop early onset IOP elevation [39, 40, 72]. We compared gene expression in *V265D* mutant
698 TM cells after integration with our wild-type data (all data B6 background and postnatal day 60,
699 Fig 6A, S16A Fig). Results show that *Lmx1b* is minimally expressed in TM1 and TM2 but is
700 highly expressed in TM3 cells (Fig 6B). Next, we analyzed DEGs and pathway differences
701 between WT and *V265D/+* cells across each TM cell subtype. Across all TM subtypes, various
702 genes related to ECM function and growth factor signaling were downregulated in mutants,
703 including glycosaminoglycans and insulin growth factor binding proteins (Fig 6C, S6 Table for
704 complete list of pathways). Pathways enriched in mutant TM cells were associated with
705 ribosome and calcium signaling. We then examined the differential responses to the *Lmx1b*
706 mutation by analyzing pathways dysregulated in each TM subtype that were not common
707 across all TM cells (Fig 6D-F, S16B Fig). *V265D* mutant TM1 cells had a downregulation of
708 collagen synthesis/metabolism gene expression relative to WT cells, particularly in the
709 production and turnover of fibrillar collagens. TM2 cells with *Lmx1b* mutations had upregulation
710 of immune signaling pathways. The highly *Lmx1b* expressing TM3 cells exhibited perturbed
711 mitochondrial metabolism, with a downregulation of genes in complex I and ATP synthase. In
712 addition, mutant TM3 cells showed an upregulation of protein tagging genes. However, there is

713 a downregulation of the polyubiquitin precursor gene (*Ubb*, P = 4.5E-30), indicating a general
714 dysregulation of pathways that tag proteins for degradation. These results document altered
715 mitochondrial function and proteostasis in TM3 cells. Although the documented gene expression
716 changes strongly suggest metabolic and mitochondrial dysfunction, they do not directly prove it.
717 Using electron microscopy to directly evaluate mitochondria in the TM, we found a reduction in
718 total mitochondria number per cell in mutants (P = 0.015, Figure 6G). In addition, mitochondria
719 in mutants had increased area and reduced cristae (inner membrane folds) in mutants
720 consistent with mitochondrial swelling and metabolic dysfunction (all P < 0.001 compared to
721 WT, Figure 6G-H).
722
723
724
725
726
727

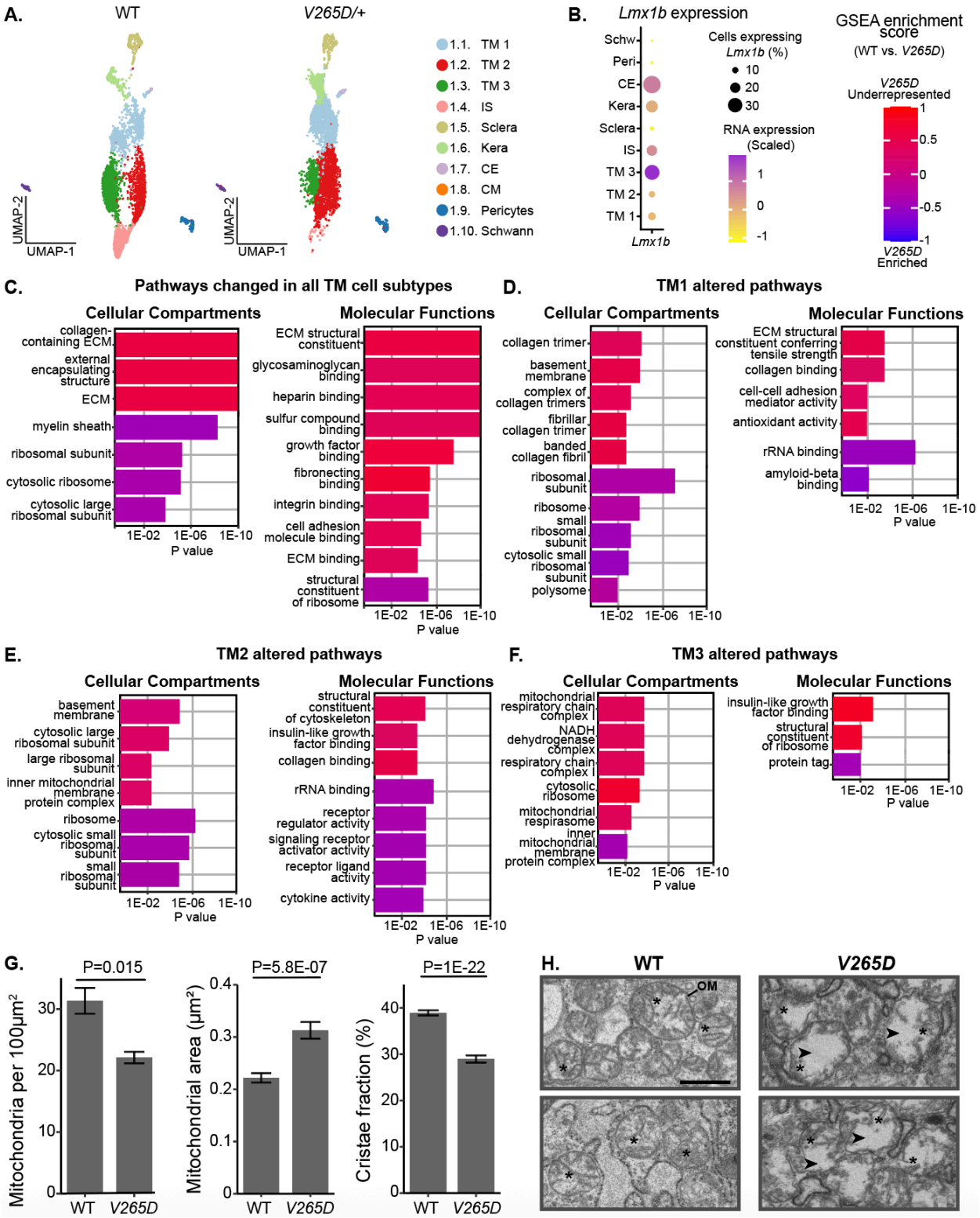

Fig 6. Differential molecular responses of TM cell subtypes to an *Lmx1b* mutation (A) UMAPs of limbal cells from WT and *Lmx1b*$^{V265D/+}$ (*V265D*) mutant mice (both genotypes B6 background). **(B)** *Lmx1b* expression across limbal cell types. *Lmx1b* expression is highest in

732 TM3 cells. **(C)** Pathways that are changed in all TM cell subtypes. **(D-F)** Top pathways that are
733 significantly altered when comparing each indicated TM cell subtype across genotypes. Many of
734 these pathways were not significantly changed when comparing all TM cell subtypes as a
735 group, indicating that the *V265D*-induced changes are strongest within each TM cell subtype.
736 *V265D* has a pronounced effect on mitochondrial pathways in TM3 cells but much less so in
737 other TM cells. ECM = extracellular matrix. ECS = extracellular structure. **(G)** Mitochondria in
738 *V265D* mutant TM cells are reduced in number per cell, have increased area, and decreased
739 cristae area (cristae fraction is ratio of area occupied by cristae: total area of mitochondria;
740 shown as bar plots with standard error). A total of 160–180 mitochondria were analyzed across
741 3 eyes per genotype (approximately 60 mitochondria per eye). Groups were compared using
742 Student's t-test. **(H)** Representative images show mitochondria defined by their outer
743 membranes (OM) and inner membrane folds (cristae). Asterisks indicate a subset of
744 representative cristae for each genotype. Mutant mitochondria exhibit increased area (space
745 enclosed by the OM) and disorganized cristae structure. Arrows highlight regions in mutant
746 mitochondria that lack cristae. Scale bar = 500 nm.

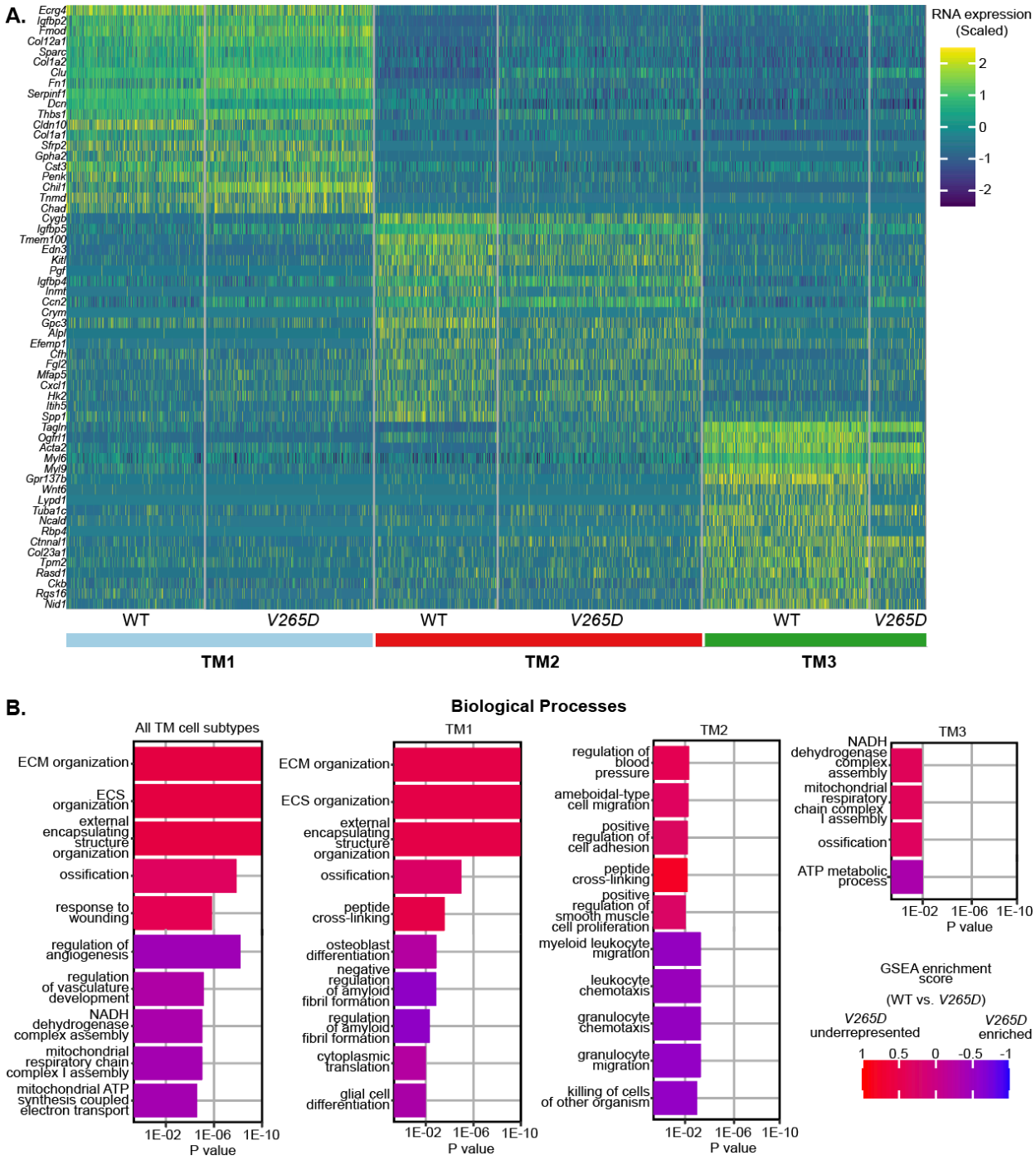

S16 Fig. Further pathway analyses of *Lmx1b*^{V265D} vs WT. (A) Heatmaps comparing marker genes for all TM cell subtypes across genotype. **(B)** The top 10 *V265D* upregulated and downregulated biological processes for the indicated comparisons across genotype are shown (all scRNA-seq data, Adjusted P values, axis cut of at 1E-10). ECM = extracellular matrix. ECS = extracellular structure.

753 Our findings most strongly implicate perturbed metabolism within TM3 cells as responsible for
754 IOP elevation in an *Lmx1b* glaucoma model. Nicotinamide (NAM) is known to boost
755 nicotinamide adenine dinucleotide (NAD), supporting healthy metabolism/ mitochondrial function
756 [73, 74]. Thus, we hypothesized that the metabolic abnormalities in TM3 cells underlie the IOP
757 elevation that causes glaucoma, and that NAM treatment may protect the *Lmx1b* mutant TM.
758 Beyond *LMX1B*, this hypothesis is relevant more commonly to POAG treatment because
759 metabolism-relevant genes are implicated by GWAS (and their expression is enriched in TM3
760 cells, S14E Fig). To test our hypothesis, we treated mice by adding NAM to their drinking water
761 starting at postnatal day 2 and continuing into adulthood. Results showed that NAM
762 supplementation significantly protected against anterior chamber deepening (ACD, a symptom
763 of IOP elevation, Fig 7A-B) and IOP elevation (Fig 7C-D). These results support NAM as a
764 treatment to prevent TM damage and IOP elevation in LMX1B-mediated glaucoma with
765 potential general relevance to POAG.
766
767
768
769

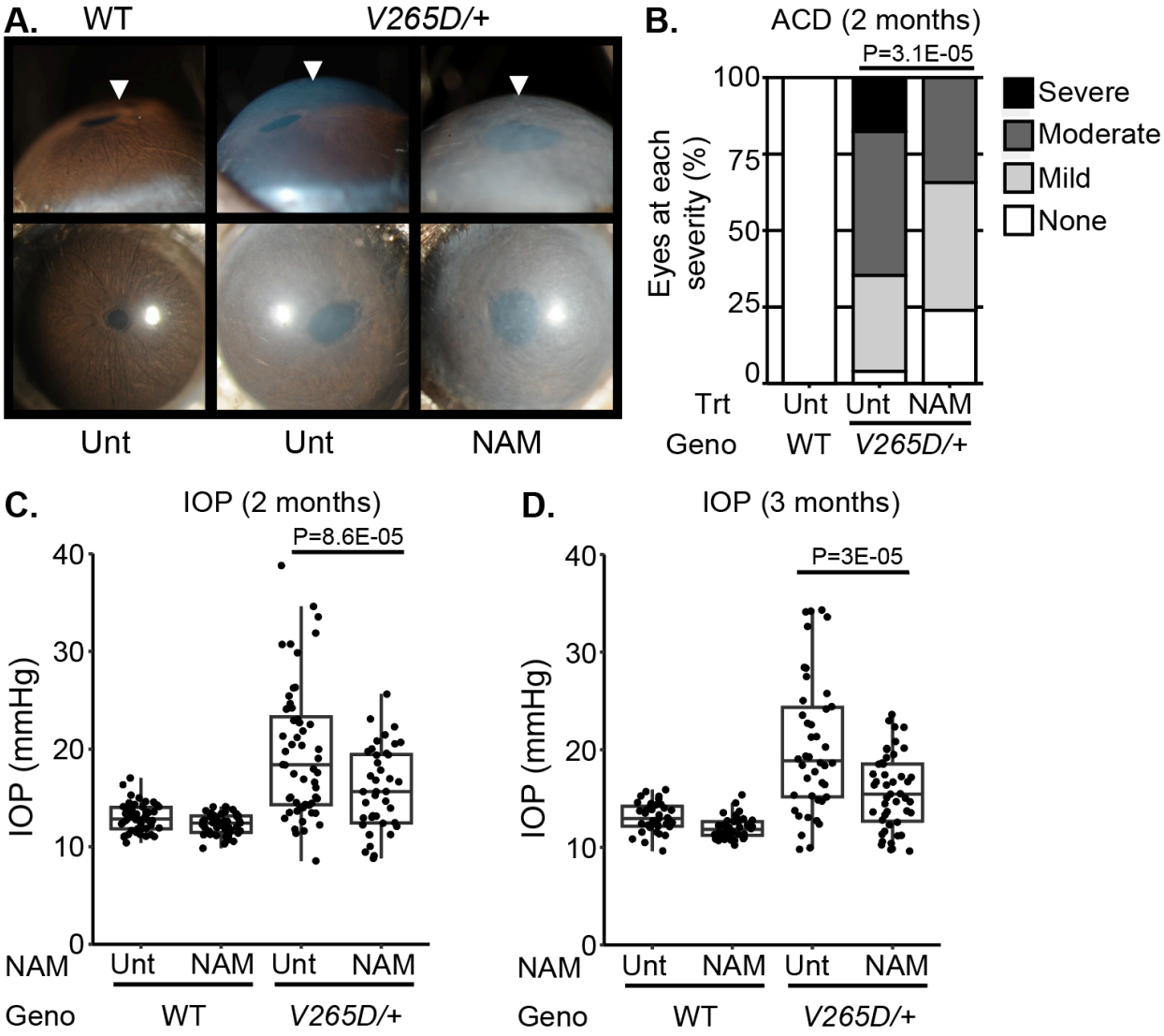

Figure 7: Nicotinamide treatment protects from IOP elevation in *Lmx1b* mutants. (A) Representative photos of eyes from mice of the indicated genotypes and treatments (UNT = untreated, NAM = nicotinamide treated, 550mg/kg/day provided in drinking water). NAM treatment substantially lessens anterior chamber deepening (ACD), a sensitive indicator of IOP elevation in mice. The WT and NAM-treated mutant eyes have very shallow anterior chambers while the untreated mutant eye has an obviously deepened chamber (arrowheads). **(B)** Distributions of anterior chamber depth based on previously defined scoring system [40]. Groups compared by Fisher's exact test. **(C-D)** Boxplots of IOP (interquartile range and median line) in WT and mutant eyes of both NAM treated and untreated groups. NAM treatment

780 significantly lessens IOP elevation in mutants compared to untreated mutant controls. Groups
781 compared by ANOVA followed by Tukey's honestly significant difference (see Table S7 for
782 additional statistics). n ≥ 35 eyes examined in each WT group and n ≥ 40 in *V265D* mutant
783 groups. Geno = genotype.

Discussion

This study provides a comprehensive multimodal analysis of mouse limbal cells that focuses on the TM. We defined three TM cell subtypes with unique marker panels that can be used for their identification across different strains, laboratories, and processing methods. We validated key marker gene expression by IF and ISH, discovering biases for specific TM subtypes to reside in different parts of the TM. For example, TM1 cells have a location bias for the outer, posterior TM while TM3 cells are more abundant in the inner, anterior TM. Importantly, our pathway analyses suggest that the different TM subtypes have overlapping roles. All 3 TM subtypes are enriched in ECM synthesis and ECM metabolism compared to other limbal subtypes. However, there is also compartmentalized enrichment of some processes to specific subtypes. For example, ECM production and turnover, secreted ligand signaling, debris removal, immune surveillance, actin-associated cell contraction and increased metabolic gene activity (as discussed below) are enriched in specific cell-subtypes. Using ATAC-seq data, we discovered key TFs controlling gene expression in TM cells, including LMX1B. Importantly, we implicate LMX1B in metabolic control in TM cells. More specifically, we demonstrate that *Lmx1b* is the most active TM cell TF and is enriched in TM3 cells, while mutation of *Lmx1b* induces prominent mitochondrial defects in TM3 cells. Finally, we show that therapeutically targeting TM3 dysfunction with a mitochondrial/ metabolism supporting nutrient (nicotinamide) protects from IOP elevation in the *Lmx1b* glaucoma model. We also suggest that a TM3-like cell is generally relevant to metabolic pathways in human glaucoma based on enriched expression of human glaucoma GWAS gene in TM3 cells. Together these data provide a wealth of new molecular information about TM cells and suggest a new approach for preventing IOP elevation.

Mouse trabecular meshwork subtype classification

809

810 Here we provide evidence for three TM cell subtypes in mice that are robust across datasets
811 from different institutions, using different tissue processing and sequencing protocols. Although
812 others [24, 51] subdivided TM cell subtypes beyond the three defined in the present study, at
813 this point we decided against further subdivision (See Figure S5) for the following reasons. We
814 lacked confidence in the higher resolution clustering, as it was not consistent across datasets,
815 did not produce unique marker gene sets, and could have resulted in over-clustering due to
816 stochastic or stress-induced differences between subpopulations of cells. Moreover, the number
817 of reported mouse TM cell clusters in previous studies were inconsistent. Although three TM
818 subtypes were reported by Van Zyl et al. and Ujiie et al. [31, 51], the molecular features of cells
819 in these clusters were not the same across these studies. Differences between studies may be
820 due to batch effects, different computational methods and possibly over-clustering. Most
821 importantly, there was very limited validation by IF, IHC, or other methods in previous studies.
822 Only the JCT type of TM cell in these previous studies was assessed by means other than
823 scRNA-seq (IF and ISH) [31]. Additionally, Thompson et al. treated cells with Y27632, a ROCK
824 inhibitor, which could alter TM cell transcriptomes. It is also important to point out that both
825 Thompson et al. and Van Zyl et al. used albino mouse strains, which can impact TM cell
826 development and function [75]. Finally, Ujiie et al. sequenced TM cells at 3-4 weeks, which is
827 prior to full maturation of the TM structure [30], while our ongoing developmental studies show
828 substantial molecular maturation of TM cells between P21 and P60.

829

830 As Van Zyl et al's data is deposited in the Broad Institute's single-cell portal, we further
831 compared their data with ours. Although both Van Zyl et al. and our current paper identified 3
832 TM subtypes, our work does not fully agree. Some of the cells named beam A and beam Y by
833 Van Zyl et al. express markers present in our TM2 cell subtype, while others express markers
834 that are absent in TM2 cells but present in our scleral cells. Our IF studies confirm that these

835 discordant markers are not expressed in TM cells, but instead show that they are in fact scleral
836 cells. These scleral cells highly express fibroblast markers including *Mfap5*, *Clec3b*, and *Tnxb*,
837 suggesting they are scleral fibroblasts. Cells initially named uveal cells by Van Zyl et al. (and
838 subsequently by Ujiie et al. and Thompson et al.) express markers of our TM3 cells. Consistent
839 with our gene expression data, our IF shows that these Van Zyl markers are expressed by cells
840 that are primarily located in the TM region that is closer to the cornea and not in the uvea or the
841 TM region adjacent to the uvea. Thus, our current study resolves some previous inconsistencies
842 in classifying mouse TM cell subtypes. It lays a firmer foundation for continued understanding of
843 TM cell types and their biology. Moving ahead, sequencing cells at greater depths will enhance
844 TM cell characterization and improve comparisons between datasets.
845

846 Differential roles of specific mouse TM cell subtypes and 847 comparison to human

848

849 As a group, all TM cells share various molecular properties that distinguish them from other
850 ocular cells. Our analyses determine the expression of IOP, and glaucoma genes identified by
851 GWAS in TM cell subtypes as well as in other limbal cells. Pathways enriched across all TM cell
852 subtypes based on RNA-seq are largely related to ECM (including collagens, integrins, and
853 glycosaminoglycan pathways), cell-cell signaling, and growth factor signaling. This fits with an
854 essential role of the TM in both ECM synthesis/turnover and in signaling to the SC to maintain
855 IOP [24, 26, 27, 76, 77]. In addition, the expression of genes that we document generally agrees
856 with the literature. For example, the following genes and signaling molecules have been
857 reported in TM cells, WNT signaling [78], TGF-β signaling [79-85], integrin binding [86-88], actin
858 cytoskeletal networks [89], calcification genes [90, 91], and Myocillin [91-94].
859

860 Additionally, genes associated with intermediate filaments, which function in determining cell
861 shape and structure and can also act as mechanical stress absorbers [95], are
862 underrepresented in TM cells. Lower levels of intermediate filaments may enable TM cells to
863 alter their shape to respond to changes in IOP.
864
865 Mouse TM1 cells closely resemble sequenced human JCT cells. Like human JCT cells, the
866 majority of TM1 cells are located nearest to the SC inner wall, particularly adjacent to the
867 posterior of the mouse SC. Human JCT cells are generally accepted to be embedded in a more
868 diffuse ECM and to not cover the collagenous trabecular beams [2, 10, 11]. In vivo, a proportion
869 of TM1 cells have a shorter, more spherical nuclear morphology, consistent with JCT cell
870 identity. Importantly, the JCT region is critical in determining resistance to AH outflow and in
871 regulating IOP [5, 12, 27, 96]. JCT cells have fibroblast-like properties, including the secretion of
872 ECM proteins and degradation enzymes to support continuous ECM remodeling [2, 76, 97]. The
873 subset of TM1 cells that lie distant from SC have more beam cell-like, elongated nuclear
874 morphology. This suggests that either our TM1 cluster contains more than 1 TM cell subtype or
875 that the morphology of a single TM1 cell subtype is influenced by local environment. This needs
876 to be resolved by future studies. Compared to the other TM cell subtypes, TM1 cell pathways
877 are enriched in both ECM structural molecules, such as collagens and integrins, and TGF-β
878 signaling, which increases ECM production [98]. Notably, excessive TGF-β signaling and ECM
879 production can lead to fibrosis and elevate IOP [82, 99-102]. TGFβ2 has also been shown to
880 cause ocular hypertension both *in vivo* [79-81] and *ex vivo* [82, 83] and is elevated in POAG
881 patients [103, 104]. These data suggest that TM1 cells play an important role in the constant
882 remodeling of the ECM. However, dysregulation of these pathways can be pathogenic.
883
884 TM2 cells molecularly resemble previously sequenced human TM beam cells [31, 33]. This
885 includes overlap of expression of top TM2 signature gene expression with sequenced human

886 beam cells. Consistent with a beam cell identity, TM2 cells are located more towards the mid
887 and inner TM than most TM1 cells. TM2 cells have an elongated nuclear morphology,
888 consistent with the previously established beam cell morphology of cells in the regions they
889 occupy [2, 30, 105]. Beam cells have endothelial-like properties, such as maintaining the
890 patency of the AH outflow tract through the production of antithrombotic molecules. Proteases
891 and molecules classically known as antithrombotic and thrombolytic maintain fluid flow through
892 the TM by preventing build-up of protein aggregates to maintain fluid drainage [5, 27]. Such
893 molecules include glycosaminoglycans, like heparin, the serine protease tPA and matrix
894 metalloprotease that are all highly expressed in TM2 cells. Beam cells are also phagocytic and
895 this activity along with turnover of ECM further cleans the TM (called filtering) to enhance fluid
896 drainage [2]. Human Beam cells also participate in antigen presentation and modulation of
897 inflammation through cytokines and major histocompatibility proteins [2, 106], consistent with
898 TM2 cells being enriched for these immune pathways/ molecules. Additionally, our data suggest
899 that signaling from TM2 cells to SC endothelial cells is mediated by soluble molecules including
900 *Vegfa*, *Edn3*, and *Angpt1*, which are critical for SC maintenance and function. This links TM2
901 cells to ocular development and glaucoma. VEGF receptor and ANGPT signaling genes
902 modulate SC development/ function as well as contribute to developmental and primary open-
903 angle glaucoma [25, 34, 35, 68, 107-109].
904
905 TM3 cells also have a location and elongated nuclear morphology resembling beam cells with
906 enriched localization in the inner, anterior TM. TM3 cell-enriched processes include actin
907 binding, and modulation of the actomyosin system, which is known to modulate outflow
908 resistance and IOP [21, 22]. As such, TM3 cells express a large percentage of glaucoma-
909 associated genes involved in actin binding at a high level. Importantly, TM3 cells are enriched
910 for various mitochondrial metabolic and antioxidant pathways, including those associated with
911 IOP elevation and glaucoma [60, 61]. Inhibiting metabolic pathways alters AH outflow resistance

912 [89]. Since maintaining contractile tone is an energy-intensive process [110], this could explain
913 the enrichment of energy metabolism pathways in TM3 cells compared to other TM cells.
914

915 TM3 cells have a unique susceptibility to mitochondrial 916 dysfunction

917

918 In addition to being enriched in mitochondrial/ energy metabolism processes, TM3 cells express
919 *Lmx1b* at significantly higher levels than both the other TM cell subtypes and other limbal cells.
920 Importantly, in heterozygous mutant *V265D/+* mice, TM3 cells had pronounced gene expression
921 changes that implicate mitochondrial dysfunction, but that were absent or much lower in other
922 cells including TM1 and TM2. In sections of the inner TM (enriched for TM3 cells), we show that
923 the inner membrane folds known as cristae are disrupted or lacking in mutant mitochondria.
924 Cristae disruptions are well established to disrupt cellular metabolism, impair oxidative
925 phosphorylation, reduce ATP synthesis, alter mitochondrial membrane potential, and elevate
926 ROS production [111-115]. Together, these data suggest that mutation of *Lmx1b* has a primary
927 effect on metabolism in TM3 cells that subsequently leads to IOP elevation and then glaucoma.
928 Relevantly, homozygous conditional knockout of both *Lmx1b* and *Lmx1a* as well as siRNA
929 knockdown of *Lmx1b* alone impact mitochondrial functions in neurons and may contribute to
930 Parkinson's disease [116-118]. Our data extend these published findings by showing that
931 inheritance of a single dominant mutation in *Lmx1b* similarly affects mitochondria in TM cells.
932 Although our studies show a clear effect of the *Lmx1b* mutation on mitochondria, future studies
933 are needed to determine if LMX1B directly modulates mitochondrial genes in *V265D* mutant TM
934 cells.
935

936 In addition to modulating mitochondria, LMX1B was recently identified as a TF that regulates
937 responses to cell stress. This includes promotion of autophagy under stress conditions to
938 enable recycling of cellular resources to maintain cellular functions and enable survival [116].
939 Thus, mutation of *Lmx1b* may also result in a deficiency of the beneficial autophagic response
940 to stress [116]. Although further experiments are needed, dysfunctional autophagy may further
941 prolong and exacerbate TM cell stress, resulting in more extensive depletion of cellular
942 resources, exacerbated cellular dysfunction, and IOP elevation. Other consequences of the
943 *Lmx1b* mutation that were evident in the *V265D/+* cells may also contribute to IOP elevation,
944 including the overexpression of genes associated with ribosomes and calcium signaling, and
945 depletion of genes involved with ECM synthesis and metabolism. However, these processes
946 were not limited to TM3 cells or even to cell types that express detectable *Lmx1b*, suggesting
947 that they are secondary damaging processes that are subsequent to the initiating, *Lmx1b*-
948 induced perturbations in TM3 cells. Thus, we hypothesize that mitochondrial abnormalities in
949 TM3 cells are of primary importance to IOP elevation in *V265D/+* glaucomatous mice.
950

951 Nicotinamide protects against IOP elevation in *Lmx1b*^{V265D}-
952 mutant mice

953

954 Based on our findings in TM3 cells, we tested if mitochondrial and metabolic disturbances are
955 important in IOP elevation by administering nicotinamide (NAM). NAM is a form of vitamin B3
956 that is well-established to boost NAD^+ levels, promote mitochondrial health and energy
957 metabolism, relieve oxidative stress and thus promote cellular resilience [74, 119-125].
958 Supporting our hypothesis of primary metabolic dysfunction in TM3 cells, NAM treatment
959 strongly protected *V265D/+* mice from IOP elevation. Thus, treatments that support normal
960 metabolism may protect from IOP elevation in individuals with *LMX1B* variants including both

961 developmental glaucoma and POAG patients [28, 34-37, 126-129]. As NAM and other NAD^+
962 boosting treatments are also known to be directly neuroprotective in glaucoma [74, 130-133],
963 our current data suggest that such treatments will have a double benefit for patients. As
964 mitochondrial defects are becoming broadly associated with glaucoma risk and progression
965 [134-138], these treatments could have wide-ranging potential to complement and augment
966 existing IOP-lowering therapeutics through a completely distinct mechanism.
967
968 Our results provide a thorough molecular characterization of mouse TM cells, providing much
969 needed molecular information on subtype specializations in regulating IOP and the roles of
970 specific subtypes in glaucoma. This comprehensive TM atlas provides a new foundation to
971 guide development of new glaucoma treatments. We validate its utility by implicating metabolic
972 changes in a single TM cell subtype in both mouse and human glaucoma, with success of a
973 metabolic treatment targeting this subtype in a glaucoma model.
974

975 # Materials and Methods

976

977 ## Animal husbandry and ethics statement

978

979 Experimental animals were either C57BL/6J (Stock# 664) or 129/Sj (unique substrain of 129)
980 [40] inbred mice. The *Lmx1b*^{V265D} mutation was discovered in an N-ethyl-N-nitrosourea (ENU)
981 mutagenesis screen [39, 40, 139]. These mice were then backcrossed to the C57BL/6J (Stock
982 #000664) for at least 30 generations. All mice were treated in accordance with the Association
983 for Research in Vision and Ophthalmology's statement on the use of animals in ophthalmic
984 research. The Institutional Animal Care and Use Committee of either Columbia University or
985 Duke University approved all experimental protocols performed at their respective institutions.

986 Mice were maintained on PicoLab Rodent Diet 20 (5053, 4.5% fat) and provided with reverse
987 osmosis-filtered water. Mutant and control littermates were housed together in cages containing
988 ¼-inch corn cob bedding, covered with polyester filters. The animal facility was maintained at a
989 constant temperature of 22°C with a 14-hour light and 10-hour dark cycle.
990

991 ## Genotyping of the *Lmx1b* allele

992

993 *Lmx1b*^{V265D} and *Lmx1b*$^{+}$ genotypes were determined by direct Sanger sequencing of a specific
994 PCR product. Genomic DNA was PCR amplified with forward primer 5′-
995 CTTTGAGCCATCGGAGCTG-3′ and reverse primer 5′-ATCTCCGACCGCTTCCTGAT-3′ using
996 the following program: (1) 94 °C for 3 min; (2) 94 °C for 30 s; (3) 57 °C for 30 s; (4) 72 °C for
997 1 min; (5) repeat steps 2–4 35 times; and (6) 72 °C for 5 min. PCR products were purified and
998 sequenced by the Genewiz (Azenta Life Sciences).
999

1000 ## Slit-lamp examination

1001

1002 Anterior eye tissues were initially examined approximately at 2 months of age. Balanced groups
1003 of males and females were examined. Photographs were taken with a 40× objective lens.
1004 Phenotypic evaluation included the same disease features found in past studies of *Lmx1b*-
1005 mutant mice [39, 40]. Anterior chamber deepening was graded based on a semiquantitative
1006 scale of phenotype being not present, mild, moderate, or severe in presentation [40]. Groups
1007 were compared statistically by Fisher's exact test. n > 30 eyes examined in each group.
1008

1009 ## IOP measurement

1010

1011 IOP was measured with the microneedle method as previously described in detail [140, 141].
1012 Prior to cannulation, mice were acclimatized to the procedure room and anesthetized via an
1013 intraperitoneal injection of a mixture of ketamine (99 mg/kg; Ketlar, Parke-Davis, Paramus, NJ,
1014 USA) and xylazine (9 mg/kg; Rompun, Phoenix Pharmaceutical, St Joseph, MO, USA)
1015 immediately prior to IOP assessment, a procedure that does not alter IOP in the experimental
1016 window [141]. IOP was measured at both 2 months and 3 months of age in WT and
1017 *Lmx1b*$^{V265D/+}$ eyes. Balanced groups of males and females were examined. During each IOP
1018 measurement period, eyes of independent WT B6 mice were assessed in parallel with
1019 experimental mice as a methodological control to ensure proper calibration and equipment
1020 function. *Lmx1b* mutant groups compared by ANOVA followed by Tukey's honestly significant
1021 difference. n ≥35 eyes examined in each WT group and n ≥ 40 in *V265D* mutant groups.
1022

1023 ## NAM administration

1024

1025 Nicotinamide (NAM or niacinamide; Sigma-Aldrich, St. Louis, Missouri) was dissolved in the
1026 standard institutional drinking water to a dose of 550 mg/kg/day (low dose) based on the
1027 average volume adult mice consume. Untreated groups received the same drinking water
1028 without NAM. Water was changed once per week. Treatment was started at postnatal day 2 and
1029 continued throughout the experiment. Births were checked daily between 9am-12pm to
1030 determine the pup's age.
1031

1032 # Sequencing

1033

1034 ## Preparation of ocular cells

1035

1036 Columbia animals: Eyes were pooled from 4 animals to generate 1 sample (8 eyes total per
1037 pool). Two independent samples were processed. Mice were 2 months of age. Sex was
1038 balanced in each group.
1039
1040 Duke animals: One sample was generated from a pool of 4 animals (8 eyes total). All mice were
1041 male. Mice were 3 months of age.
1042
1043 Dissections: After euthanizing the animals, eyes were enucleated into fresh Dulbecco's Modified
1044 Eagle Medium (DMEM; Gibco) and subsequently dissected in DMEM. All dissection tools and
1045 surfaces were treated with RNAse zap (Ambion). For dissections, we removed the posterior eye
1046 by cutting between the limbus and sclera. The lens was then removed. Finally, we made a small
1047 circular cut in the anterior cornea, removing the middle 1/3rd of the area. Only limbal tissues
1048 were collected and all other tissues were removed. The remaining limbal tissue was minced and
1049 prepared for digestion.
1050

1051 Single Cell RNA Sequencing

1052
1053 Single-cell RNA sequencing (Columbia University): Tissues were digested enzymatically using
1054 Papain and Deoxyribonuclease I (Worthington Biochemical Corporation, Cat. no. LK003153) for
1055 20 min at 37°C and stopped using Earl's balanced salt solution (EBSS, Thermo Fisher
1056 Scientific, Cat no. 24010-043). Cells were triturated using an 18-gauge needle, centrifuged at
1057 300g at 4 °C, washed with cold DMEM, and filtered using a 100 µm Flowmi Cell Strainer
1058 (H13680-0040, Bel-Art. Cells were resuspended in cold DMEM and placed on ice immediately.
1059 Cells were counted using Countess II automated cell counter and processed for 10x library

1060 preparation immediately (see below). All data will be deposited in the Gene Expression
1061 Omnibus (GEO) database and single cell portal.
1062
1063 Single-cell RNA sequencing (Duke University): Single cell dissociation was performed using
1064 Collagenase IV (Worthington Biochemical Cat. no. LS004188), Dispase II (Sigma Cat. No.
1065 D4693) and DNAse I (Roche Cat no. 50225500) for 60 min and then trypsin/EDTA for 10 min at
1066 37°C. Cells were triturated using a 1 ml pipette tip, centrifuged at 300g at 4°C, washed with cold
1067 DMEM containing 10% FBS, and filtered using a 70 µm cell strainer (Fisher). Cells were
1068 resuspended in cold DMEM containing 5% FBS and placed on ice immediately and sent to
1069 Duke Genome Core Facility. Cells were counted using Countess II automated cell counter (the
1070 cell viability was 88%) and then immediately processed immediately (see below). All data will be
1071 deposited in the Gene Expression Omnibus (GEO) database and single cell portal.
1072
1073 Multiome (Columbia University): Limbal strip samples for multiome analysis were snap-frozen
1074 on dry ice immediately following dissection and stored at -80C until processing. To isolate
1075 nuclei, tissue was homogenized in 100 µL of chilled lysis buffer (10 mM Tris-HCl, pH 7.4, 10 mM
1076 NaCl, 3 mM MgCl2, 0.1% NP40, 0.1% Tween20, and 0.01% digitonin – from [142]
1077 supplemented with 1% BSA). Afterwards, samples were incubated for 5 min on ice, gently
1078 agitated by pipetting, and incubated for an additional 10 minutes on ice. We then added 1 mL of
1079 chilled wash buffer (10 mM Tris-HCl, pH 7.4, 10 mM NaCl, 3 mM MgCl2, 0.1% Tween 20, 1%
1080 BSA) to the cells and centrifuged at 500 rcf for 5 min at 4°C. Cells were resuspended in chilled
1081 Diluted Nuclei Buffer (PN-2000153, 10x Genomics) and filtered through a 40 µm Flowmi Cell
1082 Strainer (H13680-0040, Bel-Art). Cells were resuspended in cold DMEM and placed on ice
1083 immediately. An aliquot of nuclei suspension was stained with SYTOX green to count nuclei
1084 using Countess II automated cell counter and processed for 10x library preparation immediately

1085 (see below). All data will be deposited in the Gene Expression Omnibus (GEO) database and
1086 single cell portal.
1087
1088 Single-cell and single-nucleus RNA-seq was performed at the single-cell sequencing core in
1089 Columbia Genome Center (Columbia University) or Duke Molecular Genomics Core (MGC,
1090 Duke University). Single cells or nuclei were loaded into chromium microfluidic chips with v3
1091 chemistry and barcoded with a 10x chromium controller (10x Genomics). RNA from the
1092 barcoded cells was reverse-transcribed, and sequencing libraries were constructed with a
1093 Chromium Single Cell v3 reagent kit (10x Genomics). Sequencing at both institutions was
1094 performed on NovaSeq 6000 (Illumina).
1095

1096 Sequencing data processing

1097
1098 **Single cell and single nucleus sequencing**: Raw reads were mapped to the mm10 reference
1099 genome by 10x Genomics Cell Ranger pipeline. “Seurat” (Version 4.0.1) [143] was used to
1100 conduct all single-cell and single-nucleus sequencing analyses. Briefly, the dataset was filtered
1101 to contain cells with at least 200 expressed genes and genes with expression in more than three
1102 cells. Cells were also filtered for mitochondrial gene expression (<20% for single-cell and <5%
1103 for single-nucleus). The dataset was log-normalized and scaled. Biological incompatibility based
1104 on gene expression was used to identify doublets. For the scRNA-seq dataset generated at
1105 Columbia scRNA-seq, we performed unsupervised clustering followed by comparison to
1106 previous annotations [24, 26, 31-33]. A resolution parameter of 0.03 was used to match these
1107 data and previous annotations. Cluster 1 was then subclustered using unsupervised methods
1108 with a resolution parameter of 0.3. All cluster identities based on a combination of known marker
1109 genes and validation experiments. For additional datasets (Duke scRNA-seq, and Columbia

1110 snRNA-seq), parameters were manually adjusted cluster cells based on the Columbia scRNA-
1111 seq dataset. Marker genes were identified using Wilcoxon test implemented in Seurat using
1112 default parameters.
1113
1114 **Multiome:** Single-nucleus multiome data were quantified by 10x CellRanger and preprocessed
1115 according to integratedSeurat v4 [143] and Signac [144]. We filtered cells which have <500 and
1116 >80000 ATAC reads, have <500 and >25000 RNA reads, and have >10% mitochondrial reads.
1117 RNA-seq processing was performed using the same methods as scRNA-seq (above). ATAC-
1118 seq processing was performed using ArchR (version 1.0.2) [145], where we used default latent
1119 semantic indexing (LSI) approach to derive low-dimensional embedding followed by single-cell
1120 neighborhood construction and graph-based clustering using the top 50 LSI dimensions
1121 excluding the first dimension. We assigned cell types using similar process based on marker
1122 peak accesibility and transferred cell type labels to the ATAC data.
1123
1124 ***Lmx1b^{V265D}* analysis**: Data from limbal cells with the *Lmx1b^{V265D}* mutation (C57BL/6J
1125 background) were integrated with Wild-Type (WT) cells from the C57BL/6J strain only. Multiple
1126 approaches were used for normalizing data for integration in Seurat, including log normalization
1127 and SC transform. The relative number of cells in each cell cluster between WT and *V265D*
1128 mutant cells changed based on the integration technique. Therefore, we chose not to assess
1129 TM or other cell proportions between genotypes. Log normalization was selected for
1130 downstream analysis based on the log-transformed integrated WT clusters being more
1131 molecularly similar to the WT only clusters compared with the SC transform results.
1132

1133 Statistical data analysis

1134

1135 **Hierarchical clustering**: TM-containing cells were assessed by hierarchical clustering based
1136 on the similarity of the expression of the top 500 marker genes (ranked by P value) of each
1137 individual cluster. This analysis filtered out low-expressing genes (expressed in >10% of cells,
1138 with a logFC > 0.25 compared to other cells).
1139
1140 **GO analysis:** Gene ontology and pathway enrichment analysis were performed by comparing
1141 the differentially expressed genes in three scenarios:
1142 1) All TM cells versus all other sequenced cells.
1143 2) Each individual TM cell subtype against other TM cell subtypes.
1144 3) WT versus *Lmx1b*$^{V265D/+}$ TM cells.
1145
1146 For comparisons of all TM cells to all sequenced cells, pathway enrichment was compared
1147 against a background expression universe of genes expressed in any sequenced cell. For
1148 comparisons of individual TM cell subtypes, only genes expressed in trabecular meshwork cells
1149 were used as a background (P value cut-off 0.01) [146].
1150
1151 **Gene set enrichment analysis (GSEA)** was performed using the same set of differentially
1152 expressed genes from the above comparisons with the GseGO function. All pathways were
1153 assigned an enrichment score (< 0, underrepresented; > 0, enriched). Pathways that were
1154 significantly enriched or underrepresented were also analyzed (P value cut-off 0.01). The R
1155 package ClusterProfiler was used for analysis [147].
1156
1157 **Module score:** From genome-wide association studies of IOP elevation [34, 35, 37, 129, 148-
1158 154] or primary open-angle glaucoma [28, 36, 38, 155-158], we curated a list of genes
1159 associated with the disease. Seurat's AddModuleScore function was applied to assess

1160 glaucoma disease risk for each cell type, using default parameters (24 bins for aggregation with
1161 100 control features per analyzed feature).
1162
1163 **Predicted ligand-receptor interactions**: Predicted ligand-target links between interacting cells
1164 were identified using LRLoop [63], which was developed based on NicheNet [64]. Briefly, the
1165 expression of genes in cell types is linked to a database of signaling and gene regulatory
1166 networks curated from prior information, enabling viable predictions of potential interactions
1167 between cell types. These interactions were calculated using target molecules from one cell
1168 type and ligands from multiple cell types. The top interactions, regardless of the cell type origin
1169 of the ligand, are represented in a Circos plot. Ligands were assigned to an individual TM cell
1170 subtype/subtypes based on the following criteria:
1171
1172 1) Exclusively assigned to a TM cell subtype if expressed > 1 transcript per ten thousand in
1173 a given cell type and expressed on average 4X more in that subtype compared to all
1174 other TM cell subtypes.
1175 2) Assigned to multiple TM cell subtypes if expression is > 1 transcript per ten thousand in
1176 multiple cell types and average ligand expression is < 4X between those TM cell
1177 subtypes.
1178 3) If ligand expression is low (< 1 transcript per ten thousand) across TM cell subtypes, the
1179 ligand is assigned to all subtypes that express the ligand.
1180
1181 **Comparison to published datasets:** To compare TM cell clusters across datasets, the top 10
1182 marker genes (by P value) for TM cell subtypes in our dataset were compared to published
1183 marker genes in other TM cell datasets [24, 31-33, 51]. Comparisons to both human and mouse
1184 TM cell data in the Van Zyl et al. dataset were performed using the Broad Institute single-cell
1185 browser:

1186 https://singlecell.broadinstitute.org/single_cell/study/SCP780.

1187

1188 **ATAC:** To refine ATAC-seq analysis, we applied ArchR [145] to remove any additional doublet
1189 cells and iteratively estimated LSI embedding using 500bp peaks tiled across the genome,
1190 followed by ArchR clustering and UMAP projection workflows to generate ATAC-seq cell
1191 clusters and two-dimensional embeddings (same cluster resolutions as above). Using marker
1192 gene expression, clusters were named and related to the single cell cluster identities. Using
1193 single-cell RNA-seq data collected earlier with annotated cell types, we projected single-cell
1194 ATAC-seq data onto the reference using ArchR's addGeneIntegrationMatrix function with
1195 default parameters. The integrated data with RNA-seq defined clusters were used for peak
1196 calling with MACS2, followed by marker peak identification (getMarkerFeatures) and TF
1197 enrichment (addMotifAnnotations) using the CisBP database [159]. Finally, TF activity was
1198 quantified using chromVAR [160] and gene-peak links were inferred using the
1199 addPeak2GeneLinks function with default parameters. All significant TFs (VAR > 1) for each TM
1200 cell subtype were filtered by average RNA expression within the entire cluster using the
1201 Columbia University scRNA-seq data (better read depth than snRNA-seq). All significant TFs
1202 with no RNA expression were removed and all TFs with expression > 0.5 counts per 10,000
1203 were prioritized for analysis. For a schematic of the analysis workflow, see *Figure 4A*. We then
1204 performed integrative analysis correlating the activity of each TF with its gene expression profile
1205 (both directly measured from multiome data and integrated expression data from reference
1206 scRNA-sequencing data). We used ArchR's correlateMatrices function, which reports Pearson
1207 correlation of normalized counts (TF activity matrix and gene expression / gene integration
1208 matrix) across 100 randomly subsampled neighborhoods of cells. We designated influential TFs
1209 as those with correlation > 0.5, adjusted p-value of correlation < 0.01, and chromVAR deviation
1210 above 75% of all TFs.

1211

1212 ATAC tracts: We chose marker genes (TM1: *Fn1*, TM2: *Gpc3*, TM3: *Acta2*) and plotted
1213 accessibility tracks. Motif footprinting analysis was performed using ArchR getFootprints
1214 function using CisBP-defined motif positions for RNA-defined cell types with default parameters.
1215

1216 Immunofluorescence and in situ hybridization

1217

1218 **Sections with antibody staining:** Enucleated adult eyes were fixed for 1 hour at 4°C in 4%
1219 paraformaldehyde (PFA, Electron Microscopy Science, Hatfield, PA) prepared in phosphate-
1220 buffered saline (1X PBS, 137 mM NaCl, 10 mM phosphate, 2.7 mM KCl, pH 7.4). Following
1221 fixation, a small window was made through the optic nerve head so that eyes would not shrivel
1222 during dehydration. Eyes were dehydrated in a 30% sucrose (Sigma-Aldrich, St. Louis,
1223 Missouri) in 1X PBS at 4°C until eyes sunk to the bottom of a 2 ml glass vial. Once sunken,
1224 eyes were embedded in optimal cutting temperature embedding medium (Fisher Scientific,
1225 Waltham, MA) and flash frozen on dry ice. Eyes were cryosectioned at 10 μm thickness in the
1226 sagittal plane. Sections were evenly spaced throughout the peripheral and central ocular
1227 regions.
1228

1229 Sections were washed three times with 1× PBS with 0.3% Triton X-100 for 5 min to quench
1230 residual fixation. The sections were then incubated with 10% Donkey serum (Sigma-Aldrich, St.
1231 Louis, Missouri) and 0.3% Triton X-100 in 1× PBS (blocking buffer) at room temperature for 1 h
1232 to block nonspecific binding of antibody and to permeabilize the tissue. The sections were then
1233 incubated with primary antibodies (see S8 Table) in 200 μl blocking buffer overnight at 4°C. The
1234 sections were then washed three times for 5 m with 1× PBS with 0.3% Triton X-100. Primary
1235 antibodies were detected with the appropriate species-specific secondary antibody (all Alexa
1236 488, 594, or 647 at 1:1000 dilution, Life Technologies, Grand Island, NY) diluted in 1× PBS with

1237 0.3% Triton X-100 for 2 h at room temperature. The secondary detection solution also had DAPI
1238 at 1:1000 (Thermo Scientific, Waltham, MA) to label nuclei. The immunostained sections were
1239 washed three times for 5 m in 1× PBS with 0.3% Triton X-100. Sections were then cover-slipped
1240 using Flouromount (Sigma, St. Louis, MO).
1241
1242 **Tyramide signal amplification (TSA):** We performed a TSA reaction for a subset of antibodies
1243 (S8 Table). TSA was performed on slides containing serial transverse cryosections of
1244 enucleated mouse eyes using the Akoya Biosciences TSA Plus Cyanine 3 detection kit
1245 (NEL744001KT). Freshly cut sections were allowed to come to room temperature and were then
1246 quenched for 10 minutes in a 1% hydrogen peroxide, 10% methanol in 0.01M phosphate
1247 buffered saline solution (1X PBS). The slides were rinsed in 1X PBS and allowed to block for 1
1248 hour at room temperature in a blocking solution of 10% donkey serum, 0.3% Triton-X 100 in 1X
1249 PBS. Primaries for TSA were diluted 1:100 in blocking solution and approximately 200
1250 microliters were added to the slides overnight at 4 degrees Celsius. The slides were then rinsed
1251 using a 0.3% Triton-X 100 in 1X PBS solution before being blocked in Tris-NaCl-blocking (TNB)
1252 buffer for 1 hour at room temperature. Approximately 200 microliters of Horseradish peroxidase
1253 conjugated secondaries diluted 1:200 in TNB buffer were applied to the slides for 2 hours at
1254 room temperature. The slides were subsequently rinsed in Tris-NaCl-Tween (TNT) buffer. TSA
1255 Plus Working Solution was made by diluting the TSA Plus Stock Solution 1:50 in 1X
1256 Amplification Diluent. The TSA Plus Working Solution was added at a volume of 200 microliters
1257 for 7 minutes at room temperature. The slides were then washed in TNT buffer and
1258 approximately 200 microliters of non-amplified primaries for counterstaining diluted 1:200 in
1259 10% donkey serum, 0.3% Triton-X 100 in 1X PBS blocking solution was applied overnight at 4
1260 degrees Celsius. Secondary antibody detection and mounting were performed as above.
1261

1262 ***in situ* hybridization**: We used the RNAscope® Multiplex Fluorescent Reagent Kit v2-Mm
1263 (Advanced Cell Diagnostics a Bio Techne Brand, Newark, CA). Probes for mouse *Lypd1*
1264 (#318361-C2), *Inmt* (#486371-C2), *Edn3* (#505841-C1), *Acta2* (α-SMA) (#319531-C3), and
1265 *Myoc* (#460981-C1) (also purchased from ACD Bio) were used. Fluorescent dyes Opal 690
1266 (FP1497001KT) and Opal 620 (FP1495001KT) (Akoya Biosciences, Marlborough, MA) were
1267 used with each of these probes. Briefly, eyes from 3-month-old C57BL/6J were enucleated and
1268 fixed in 4% PFA for 24 h at 4°C. A window was made to the back of the eye cup, lens removed,
1269 and the anterior cup placed in 30% sucrose overnight at 4°C. Tissue was cryopreserved in OCT
1270 and placed at -80°C. Sections were cut at 12 μm thickness using SuperFrost Plus slides
1271 (Fisher Scientific, Hampton, NH).. RNAscope® was performed over two days as per
1272 manufacturer's protocol.
1273
1274 **Whole mounts**: Enucleated eyes were fixed for 2 hours at 4°C in 4% paraformaldehyde (PFA,
1275 Electron Microscopy Science, Hatfield, PA) prepared in phosphate-buffered saline (1× PBS, 137
1276 mM NaCl, 10 mM phosphate, 2.7 mM KCl, pH 7.4). The postnatal eyes were dissected out
1277 following fixation. The anterior part of the eye was cut just posterior to the limbus (transition
1278 zone between cornea and sclera) as described in Kizhatil et al. [25]. Briefly, the iris, lens, ciliary
1279 body, and thin strip of retina were carefully removed to obtain the anterior eye cup. The anterior
1280 cup includes the cornea, limbus, and a small portion of retinal pigmented epithelium. Four
1281 centripetal cuts were made to relax the eye-cup and facilitate eventual mounting onto a slide
1282 after immunofluorescence.
1283
1284 Anterior eye cups were rinsed multiple times with 1× PBS. The eye cups were incubated with
1285 3% bovine serum albumin and 1% Triton X-100 in 1× PBS (blocking buffer) at room temperature
1286 for 1 h in 2 ml glass vials to block nonspecific binding of antibody and to permeabilize the tissue.
1287 The anterior cups were then incubated with primary antibodies (S8 Table) in 200 μl blocking

1288 buffer for 2 days, with rocking, at 4°C. The anterior cups were then washed three times over a
1289 3-h period with 1× PBS. The primary antibodies were detected with the appropriate species-
1290 specific secondary antibody (all Alexa 488, 594, or 647 at 1:1,000 dilution, Life Technologies,
1291 Grand Island, NY) diluted in blocking buffer, which also had DAPI to label nuclei. The
1292 immunostained eye cups were washed three times over a 3-h period in 1× PBS. Eye cups were
1293 then whole-mounted on slides in Fluoromount (Sigma, St. Louis, MO).
1294

1295 Microscopy of drainage structures

1296
1297 Sections: Microscopy of sectioned postnatal eye slides was performed using an LSM SP8
1298 confocal microscope (Leica) and 40×1.1 NA water immersion objective.
1299
1300 *In situ*: Images were taken using a Nikon Eclipse 90i confocal laser-scanning microscope
1301 (Melville). Z-stack images of 1 μm thickness, using the 40X objective lens, were taken of each
1302 section and converted into maximum projection images that were used for analysis.
1303
1304 Whole mounts: Microscopy was performed using an LSM SP8 confocal microscope (Leica)
1305 using a 63×1.4 NA glycerol immersion objective. The Mark and Find mode was used to
1306 automate collection of images, generating a folder full of Z stacks (Z = 0.3 μm) at various
1307 individual overlapping positions around the limbus. We examined n = 6 eyes total. We imaged a
1308 certain distance around the ocular circumference, with an equal representation from each ocular
1309 quadrant (1.5-2.5 mm total).
1310

1311 Postprocessing of whole-mount images

1312

3D rendering: We followed the guidelines detailed in Kizhatil et al for visualizing SC and TM in 3D. Individual confocal Z stacks (.lsm files) were processed directly using Imaris 9.5 (Oxford Instruments, Carteret, NJ). The maximum intensity projection setting in Surpass mode of Imaris was used for 3D rendering. Controls and experimental image sets were treated identically. Images were oriented so that structures of interest were visible. For whole-mounted eyes, multiposition Z stacks generated using the Mark and Find setting on the confocal microscope were first imported into Imaris and converted into Imaris files (.ims files). The resulting Imaris files were then stitched to generate a comprehensive Z stack encompassing the limbus using ImarisStitcher 9.5 (BitPlane AG, Zurich, Switzerland). The stitch was exported as an Imaris file and processed appropriately. For sections, images were taken in the Z-plane in focus. When making figures, the snapshot feature of Imaris was used to collect images at high resolution (1024×1024 pixels, 300 dpi).

TM marker location analysis

We defined the TM as the region between the inner wall of Schlemm's canal (SC, outer TM) and the anterior chamber (inner TM), extending from the anterior edge of the pars plana (posterior TM) to the posterior edge of Descemet's membrane of the corneal endothelium (anterior TM). The SC was defined using a panel of validated markers that varied to allow for different antibody species and different secondary antibodies to be used in conjunction with the SC markers (See Table S8 for list of antibodies) [25]. Sections were only included in the scoring analysis if they met the following criteria:

1) Absence of obvious sectioning artifacts or abnormalities in the SC or TM region.
2) Distinguishability of all landmarks defining the TM.

1337 3) Acceptably low background signal and absence of staining for non-specific or non-
1338 biological entities within the section.
1339
1340 For each section, the TM was segmented and analyzed in two separate ways. The anterior-
1341 posterior distance was measured, and the TM was divided in half along this axis at the midway
1342 point (S7C-D Fig). Using the surface feature in Imaris, the area of individual marker staining was
1343 measured, and the total area in both the anterior and posterior zones was calculated. Because
1344 markers are expressed at different levels, we normalized across markers by calculating the
1345 percent of individual marker expression in the anterior and posterior halves within each section.
1346 These percentage values in anterior and posterior halves were compared both within markers
1347 and across all markers of a given TM cell subtype by Student's t-test. The same analysis was
1348 repeated for the inner-outer halves by measuring the inner-outer TM distance at the midpoint of
1349 the TM (anterior-posterior axis) and dividing the TM in half at this value. A total of 130-160
1350 sections were examined for markers of each individual TM cell subtype. These sections were
1351 from 10-12 individual eyes per cluster. All eyes were from WT mice of C57BL/6J background
1352 and between 3-6 months of age.
1353
1354 Additional analysis was performed by selecting a subset of examined sections with staining for
1355 select markers (TM1: MYOC antibody, TM2: CRYM antibody, *Inmt in situ*, TM3: α-SMA
1356 antibody). These sections were of exceptionally high quality and had: 1) Anterior-posterior TM
1357 length between 125-200 μm. 2) Inner-outer TM distance is between 15-30 μm.
1358
1359 With these selected sections, we subdivided the TM into eight different zones along both
1360 inner/outer and anterior/posterior axes (Figure S7F). For each individual section, we used Imaris
1361 to measure the anterior-posterior distance and divide the TM into three equal sectors (anterior,
1362 central, and posterior. Within each sector, the average depth of the TM was measured in Imaris.

1363 This calculation was used to divide the central and posterior sectors into three zones each
1364 (inner, intermediate, and outer). Because the anterior TM depth is thinner, we divided the
1365 anterior sector into two zones (inner and outer). In total, there were eight distinct zones.
1366
1367 The percent of total marker area was calculated for each of the eight zones for each individual
1368 section as described above. Percent of marker area in each zone was compared as shown in
1369 Figure 2 by one-way ANOVA followed by Tukey's honestly significant difference test.
1370

1371 Scleral cell marker analysis

1372
1373 For CD34 and LY6C1 expression, we examined greater than 60 sections from 4 eyes (CD34)
1374 and 3 eyes (LY6C1) respectively. The observed locations of these markers within the
1375 iridocorneal angle are described.
1376

1377 Whole mount marker location analysis

1378
1379 To analyze the expression of markers within the TM, we segmented the TM based on anatomy.
1380 Because various anatomical features including the pars plana were removed during the whole
1381 mount process, we used the SC (marked by PECAM) as the major anterior-posterior landmark.
1382 The TM was defined as the group of cells inner to the SC and not outside the anterior or
1383 posterior boundary of the SC.
1384

1385 Nuclear morphology

1386

1387 Anterior segment whole-mounts were used to examine nuclear morphology in 3D (TM1: MYOC,
1388 TM3: α-SMA, all antibodies). The TM was segmented as described above and the 'Surface'
1389 feature in Imaris used to demarcate TM cell nuclei. Nuclei that were analyzed were immediately
1390 adjacent to the immunolabeled TM marker and had to be well spaced from other nuclei. To
1391 ensure accuracy we used manual inspection to exclude: 1) Nuclei that were very close to other
1392 nuclei or groups of nuclei and 2) nuclei of cells that were labeled with a Schlemm's canal
1393 endothelial cell marker (PECAM) and/ or that projected into the lumen of SC. The 'Sphericity'
1394 tool was used to determine the degree of sphericity in Imaris. For each cell subtype, we
1395 assessed a total 60 nuclei from 6 eyes, assessing the first 10 randomly selected nuclei that met
1396 our inclusion criteria in each eye. Groups were compared by Student's t-test.
1397
1398 Electron microscopy
1399 Mice were euthanized, and eyes were enucleated into DBG buffer containing 1X Dulbecco's
1400 phosphate-buffered saline with 5.5 mM D-glucose (Sigma-Aldrich). Eyes were immediately
1401 dissected in DBG buffer to generate anterior segment eye cups, with centripetal relaxing cuts in
1402 the cornea to allow flattening (see Figure S1). The tissue was fixed at room temperature for 30
1403 minutes in a solution of 0.8% paraformaldehyde, 1.2% glutaraldehyde, and 0.08 M phosphate
1404 buffer (Smith-Rudt). Following fixation, each anterior segment was mounted on a slide and
1405 flattened under a coverslip overnight at 4 °C. A 1 g weight was placed on top of the coverslip to
1406 aid in flattening the limbal region. The eyes were then washed three times in 1X PBS for 15
1407 minutes each and stored in PBS under the same slide/coverslip setup to maintain flattening until
1408 embedding. Before further processing, individual limbal strips of the four quadrants of each were
1409 dissected from the surrounding cornea and sclera (see Figure S1). These strips were post-fixed
1410 in 2% aqueous osmium tetroxide, rinsed in PBS, and dehydrated for epoxy resin embedding
1411 using EMBED 812 (Electron Microscopy Sciences). Embedding was performed while preserving
1412 the orientation of the limbal strip, with the TM (inner side) and cornea / sclera (outer side) clearly

1413 maintained. Embedded strips were imaged using computed tomography to locate the tissue,
1414 confirm TM orientation and flattening for *en face* sectioning, and to guide the sectioning
1415 process. Ultrathin, 70 nm, *enface* sections of the inner side of the limbal strip were taken using a
1416 Leica ultramicrotome (inner TM is the most superficial tissue being sectioned). Sections were
1417 placed onto formvar coated slot grids then stained en grid using a combination of 5% Uranyl
1418 Acetate and Reynold's lead citrate (Reynold's 1963) for 17 and 7 minutes, respectively. Large
1419 mosaic regions of the TM were imaged at 5,000× magnification (2.18nm/px) using a JEOL
1420 1400FLASH TEM operating at 80 kV, equipped with a Gatan OneView camera. Mosaics were
1421 then computationally reconstructed using custom nornir-buildscripts (https://nornir.github.io/)
1422 and initially visualized in the Software suite Viking (http://connectomes.utah.edu)
1423
1424 From each TM section, 20 cells with sampled nucei were randomly selected from evenly spaced
1425 regions throughout the imaged area (approximately 25,000 μm² per eye). In the perinuclear area
1426 of each selected cell, up to 3 (typically 2-3) mitochondria were randomly selected and analyzed.
1427 The perimeter of the mitochondrial outer membrane (area) and inner membrane (cristae) were
1428 traced in ImageJ according to established protocols [161, 162]. The percentage of cristae area
1429 compared to the whole mitochondrial area was calculated (cristae fraction) for each
1430 mitochondrion. The number of mitochondria were counted in the perinuclear region of each
1431 analyzed cell. This number was normalized to an area of 100 μm² and averaged across cells.
1432 As each en face section sampled a large area of the TM. 3 sections from different eyes were
1433 examined for each genotype. All mice were 14 days old. A total of 178 mitochondria from WT
1434 eyes and 161 from *V265D* eyes were analyzed. Groups were compared by Student's t-test.
1435

1436 # Funding

1437

This project was supported by National Eye Institute grant EY032507 (to S.W.M.J). Partial support was provided by EY011721, EY032062, and EY018606 (to SWMJ), Brightfocus grants CG2020004 (to S.W.M.J.), and G2021007 (to R.B.), startup funds at Columbia University including the Precision Medicine Initiative, and the New York Fund for Innovation in Research and Scientific Talent (NYFIRST; EMPIRE CU19-2660). At Duke, the work was also supported by NEI grants EY028608, EY022359 (to WDS). Supported also came from Vision Core grants P30EY019007 (Columbia University), P30EY005722 (Duke University), The Glaucoma Foundation (Columbia University) and an unrestricted departmental award from Research to Prevent Blindness (Columbia University and Duke University). The content is solely the responsibility of the authors and does not necessarily represent the official views of the National Institutes of Health. SWMJ is the Robert Burch III Professor of Ophthalmic Sciences.

Acknowledgments

The authors would like to thank the members of the Simon John Laboratory for experimental and technical assistance, Drs. Krish Kizhatil and Chi Zhang for reading and editing the manuscript, the Institute of Comparative Medicine and Devanshi Ragha at Columbia University for animal and veterinary care, the JP Sulzberger Columbia Genome Center and Duke University Molecular Genomics Core for assistance with genomics studies, and the P30EY019007 Columbia Shared Resources grant for histological experiments.

References

1. Quigley HA, Broman AT. The number of people with glaucoma worldwide in 2010 and 2020. Br J Ophthalmol. 2006;90(3):262-7. Epub 2006/02/21. doi: 10.1136/bjo.2005.081224. PubMed PMID: 16488940; PubMed Central PMCID: PMCPMC1856963.
2. Stamer WD, Clark AF. The many faces of the trabecular meshwork cell. Exp Eye Res. 2017;158:112-23. Epub 2016/07/23. doi: 10.1016/j.exer.2016.07.009. PubMed PMID: 27443500; PubMed Central PMCID: PMCPMC5247412.

3. Keller KE, Peters DM. Pathogenesis of glaucoma: Extracellular matrix dysfunction in the trabecular meshwork-A review. Clin Exp Ophthalmol. 2022;50(2):163-82. Epub 2022/01/18. doi: 10.1111/ceo.14027. PubMed PMID: 35037377; PubMed Central PMCID: PMCPMC9199435.
4. Buffault J, Labbe A, Hamard P, Brignole-Baudouin F, Baudouin C. The trabecular meshwork: Structure, function and clinical implications. A review of the literature. J Fr Ophtalmol. 2020;43(7):e217-e30. Epub 2020/06/21. doi: 10.1016/j.jfo.2020.05.002. PubMed PMID: 32561029.
5. Acott TS, Kelley MJ. Extracellular matrix in the trabecular meshwork. Exp Eye Res. 2008;86(4):543-61. Epub 2008/03/04. doi: 10.1016/j.exer.2008.01.013. PubMed PMID: 18313051; PubMed Central PMCID: PMCPMC2376254.
6. Fuchshofer R, Welge-Lussen U, Lutjen-Drecoll E, Birke M. Biochemical and morphological analysis of basement membrane component expression in corneoscleral and cribriform human trabecular meshwork cells. Invest Ophthalmol Vis Sci. 2006;47(3):794-801. Epub 2006/03/01. doi: 10.1167/iovs.05-0292. PubMed PMID: 16505009.
7. Yue BY. The extracellular matrix and its modulation in the trabecular meshwork. Surv Ophthalmol. 1996;40(5):379-90. Epub 1996/03/01. doi: 10.1016/s0039-6257(96)80066-x. PubMed PMID: 8779084.
8. Vittal V, Rose A, Gregory KE, Kelley MJ, Acott TS. Changes in gene expression by trabecular meshwork cells in response to mechanical stretching. Invest Ophthalmol Vis Sci. 2005;46(8):2857-68. Epub 2005/07/27. doi: 10.1167/iovs.05-0075. PubMed PMID: 16043860.
9. Abu-Hassan DW, Acott TS, Kelley MJ. The Trabecular Meshwork: A Basic Review of Form and Function. J Ocul Biol. 2014;2(1). Epub 2014/10/31. doi: 10.13188/2334-2838.1000017. PubMed PMID: 25356439; PubMed Central PMCID: PMCPMC4209746.
10. Vranka JA, Kelley MJ, Acott TS, Keller KE. Extracellular matrix in the trabecular meshwork: intraocular pressure regulation and dysregulation in glaucoma. Exp Eye Res. 2015;133:112-25. Epub 2015/03/31. doi: 10.1016/j.exer.2014.07.014. PubMed PMID: 25819459; PubMed Central PMCID: PMCPMC4379427.
11. Keller KE, Acott TS. The Juxtacanalicular Region of Ocular Trabecular Meshwork: A Tissue with a Unique Extracellular Matrix and Specialized Function. J Ocul Biol. 2013;1(1):3. Epub 2013/12/24. PubMed PMID: 24364042; PubMed Central PMCID: PMCPMC3867143.
12. Johnson M. 'What controls aqueous humour outflow resistance?'. Exp Eye Res. 2006;82(4):545-57. Epub 2006/01/03. doi: 10.1016/j.exer.2005.10.011. PubMed PMID: 16386733; PubMed Central PMCID: PMCPMC2892751.
13. Tian B, Gabelt BT, Geiger B, Kaufman PL. The role of the actomyosin system in regulating trabecular fluid outflow. Exp Eye Res. 2009;88(4):713-7. Epub 2008/09/17. doi: 10.1016/j.exer.2008.08.008. PubMed PMID: 18793636; PubMed Central PMCID: PMCPMC2694502.
14. Tamm ER. The trabecular meshwork outflow pathways: structural and functional aspects. Exp Eye Res. 2009;88(4):648-55. Epub 2009/02/26. doi: 10.1016/j.exer.2009.02.007. PubMed PMID: 19239914.
15. Overby DR, Stamer WD, Johnson M. The changing paradigm of outflow resistance generation: towards synergistic models of the JCT and inner wall endothelium. Exp Eye Res. 2009;88(4):656-70. Epub 2008/12/24. doi: 10.1016/j.exer.2008.11.033. PubMed PMID: 19103197; PubMed Central PMCID: PMCPMC2744486.

1509 16. Zhang M, Rao PV. Blebbistatin, a novel inhibitor of myosin II ATPase activity, increases
1510 aqueous humor outflow facility in perfused enucleated porcine eyes. Invest Ophthalmol Vis Sci.
1511 2005;46(11):4130-8. Epub 2005/10/27. doi: 10.1167/iovs.05-0164. PubMed PMID: 16249490.
1512 17. Thieme H, Nuskovski M, Nass JU, Pleyer U, Strauss O, Wiederholt M. Mediation of
1513 calcium-independent contraction in trabecular meshwork through protein kinase C and rho-A.
1514 Invest Ophthalmol Vis Sci. 2000;41(13):4240-6. Epub 2000/11/30. PubMed PMID: 11095621.
1515 18. Rao PV, Deng P, Sasaki Y, Epstein DL. Regulation of myosin light chain
1516 phosphorylation in the trabecular meshwork: role in aqueous humour outflow facility. Exp Eye
1517 Res. 2005;80(2):197-206. Epub 2005/01/27. doi: 10.1016/j.exer.2004.08.029. PubMed PMID:
1518 15670798.
1519 19. Syriani E, Cuesto G, Abad E, Pelaez T, Gual A, Pintor J, et al. Effects of platelet-derived
1520 growth factor on aqueous humor dynamics. Invest Ophthalmol Vis Sci. 2009;50(8):3833-9. Epub
1521 2009/04/10. doi: 10.1167/iovs.08-2924. PubMed PMID: 19357356.
1522 20. Tian B, Kaufman PL. Effects of the Rho kinase inhibitor Y-27632 and the phosphatase
1523 inhibitor calyculin A on outflow facility in monkeys. Exp Eye Res. 2005;80(2):215-25. Epub
1524 2005/01/27. doi: 10.1016/j.exer.2004.09.002. PubMed PMID: 15670800.
1525 21. Rao PV, Deng PF, Kumar J, Epstein DL. Modulation of aqueous humor outflow facility
1526 by the Rho kinase-specific inhibitor Y-27632. Invest Ophthalmol Vis Sci. 2001;42(5):1029-37.
1527 Epub 2001/03/29. PubMed PMID: 11274082.
1528 22. Yu M, Chen X, Wang N, Cai S, Li N, Qiu J, et al. H-1152 effects on intraocular pressure
1529 and trabecular meshwork morphology of rat eyes. J Ocul Pharmacol Ther. 2008;24(4):373-9.
1530 Epub 2008/07/31. doi: 10.1089/jop.2008.0029. PubMed PMID: 18665808; PubMed Central
1531 PMCID: PMCPMC2810742.
1532 23. Wang K, Li G, Read AT, Navarro I, Mitra AK, Stamer WD, et al. The relationship
1533 between outflow resistance and trabecular meshwork stiffness in mice. Sci Rep. 2018;8(1):5848.
1534 Epub 2018/04/13. doi: 10.1038/s41598-018-24165-w. PubMed PMID: 29643342; PubMed
1535 Central PMCID: PMCPMC5895808.
1536 24. Thomson BR, Liu P, Onay T, Du J, Tompson SW, Misener S, et al. Cellular crosstalk
1537 regulates the aqueous humor outflow pathway and provides new targets for glaucoma therapies.
1538 Nat Commun. 2021;12(1):6072. Epub 2021/10/20. doi: 10.1038/s41467-021-26346-0. PubMed
1539 PMID: 34663817; PubMed Central PMCID: PMCPMC8523664 patents related to therapeutic
1540 targeting of the ANGPT-TEK pathway in ocular hypertension and glaucoma and owns stock in
1541 and is a director of Mannin Research. S.E.Q. also receives consulting fees from AstraZeneca,
1542 Janssen, the Lowy Medical Research Foundation, and Roche/Genentech; is Chair of the External
1543 Scientific Advisory Board for AstraZeneca; and is a scientific advisor or member of
1544 AstraZeneca, Genentech/Roche, the Karolinska CVRM Institute, the Lowy Medical Research
1545 Institute, Mannin, and Novartis. J.J. has applied for a patent related to the ANGPT1 mimetic
1546 compound described in the article. In addition, he is a scientific advisor for Mannin Research and
1547 QBioMed. T.L.Y. serves as a consultant to Aerpio Pharmaceuticals. The other authors declare no
1548 competing interests.
1549 25. Kizhatil K, Ryan M, Marchant JK, Henrich S, John SW. Schlemm's canal is a unique
1550 vessel with a combination of blood vascular and lymphatic phenotypes that forms by a novel
1551 developmental process. PLoS Biol. 2014;12(7):e1001912. Epub 2014/07/23. doi:
1552 10.1371/journal.pbio.1001912. PubMed PMID: 25051267; PubMed Central PMCID:
1553 PMCPMC4106723.

1554 26. Balasubramanian R, Kizhatil K, Li T, Tolman N, Bhandari A, Clark G, et al.
1555 Transcriptomic profiling of Schlemm's canal cells reveals a lymphatic-biased identity and three
1556 major cell states. bioRxiv. 2024. Epub 2023/10/27. doi: 10.1101/2023.08.31.555823. PubMed
1557 PMID: 37886472; PubMed Central PMCID: PMCPMC10602040.
1558 27. Stamer WD, Acott TS. Current understanding of conventional outflow dysfunction in
1559 glaucoma. Curr Opin Ophthalmol. 2012;23(2):135-43. Epub 2012/01/21. doi:
1560 10.1097/ICU.0b013e32834ff23e. PubMed PMID: 22262082; PubMed Central PMCID:
1561 PMCPMC3770936.
1562 28. Gharahkhani P, Jorgenson E, Hysi P, Khawaja AP, Pendergrass S, Han X, et al. Genome-
1563 wide meta-analysis identifies 127 open-angle glaucoma loci with consistent effect across
1564 ancestries. Nat Commun. 2021;12(1):1258. Epub 2021/02/26. doi: 10.1038/s41467-020-20851-4.
1565 PubMed PMID: 33627673; PubMed Central PMCID: PMCPMC7904932 J.W. is a consultant for
1566 Allergan, Editas, Maze, Regenxbio and has received sponsored research support from Aerpio
1567 Pharmaceuticals Inc. L.P. is a consultant for Eyenovia, Bausch + Lomb, Verily, and Nicox.
1568 T.L.Y. serves as a consultant to Aerpio Pharmaceuticals, Inc. A.P.K. is a consultant to Aerie,
1569 Allergan, Google Health, Novartis, Reichert, Santen and Thea. All remaining authors declare no
1570 competing interests.
1571 29. Chen L, Zhao Y, Zhang H. Comparative Anatomy of the Trabecular Meshwork, the
1572 Optic Nerve Head and the Inner Retina in Rodent and Primate Models Used for Glaucoma
1573 Research. Vision (Basel). 2016;1(1). Epub 2016/07/18. doi: 10.3390/vision1010004. PubMed
1574 PMID: 31740629; PubMed Central PMCID: PMCPMC6848998.
1575 30. Smith RS, Zabaleta A, Savinova OV, John SW. The mouse anterior chamber angle and
1576 trabecular meshwork develop without cell death. BMC Dev Biol. 2001;1:3. Epub 2001/03/03.
1577 doi: 10.1186/1471-213x-1-3. PubMed PMID: 11228591; PubMed Central PMCID:
1578 PMCPMC31337.
1579 31. van Zyl T, Yan W, McAdams A, Peng YR, Shekhar K, Regev A, et al. Cell atlas of
1580 aqueous humor outflow pathways in eyes of humans and four model species provides insight into
1581 glaucoma pathogenesis. Proc Natl Acad Sci U S A. 2020;117(19):10339-49. Epub 2020/04/29.
1582 doi: 10.1073/pnas.2001250117. PubMed PMID: 32341164; PubMed Central PMCID:
1583 PMCPMC7229661.
1584 32. van Zyl T, Yan W, McAdams AM, Monavarfeshani A, Hageman GS, Sanes JR. Cell
1585 atlas of the human ocular anterior segment: Tissue-specific and shared cell types. Proc Natl Acad
1586 Sci U S A. 2022;119(29):e2200914119. Epub 2022/07/21. doi: 10.1073/pnas.2200914119.
1587 PubMed PMID: 35858321; PubMed Central PMCID: PMCPMC9303934.
1588 33. Patel G, Fury W, Yang H, Gomez-Caraballo M, Bai Y, Yang T, et al. Molecular
1589 taxonomy of human ocular outflow tissues defined by single-cell transcriptomics. Proc Natl
1590 Acad Sci U S A. 2020;117(23):12856-67. Epub 2020/05/23. doi: 10.1073/pnas.2001896117.
1591 PubMed PMID: 32439707; PubMed Central PMCID: PMCPMC7293718.
1592 34. Khawaja AP, Cooke Bailey JN, Wareham NJ, Scott RA, Simcoe M, Igo RP, Jr., et al.
1593 Genome-wide analyses identify 68 new loci associated with intraocular pressure and improve
1594 risk prediction for primary open-angle glaucoma. Nat Genet. 2018;50(6):778-82. Epub
1595 2018/05/23. doi: 10.1038/s41588-018-0126-8. PubMed PMID: 29785010; PubMed Central
1596 PMCID: PMCPMC5985943.
1597 35. MacGregor S, Ong JS, An J, Han X, Zhou T, Siggs OM, et al. Genome-wide association
1598 study of intraocular pressure uncovers new pathways to glaucoma. Nat Genet. 2018;50(8):1067-
1599 71. Epub 2018/07/29. doi: 10.1038/s41588-018-0176-y. PubMed PMID: 30054594.

36. Choquet H, Paylakhi S, Kneeland SC, Thai KK, Hoffmann TJ, Yin J, et al. A multiethnic genome-wide association study of primary open-angle glaucoma identifies novel risk loci. Nat Commun. 2018;9(1):2278. Epub 2018/06/13. doi: 10.1038/s41467-018-04555-4. PubMed PMID: 29891935; PubMed Central PMCID: PMCPMC5995837.
37. Gao XR, Huang H, Nannini DR, Fan F, Kim H. Genome-wide association analyses identify new loci influencing intraocular pressure. Hum Mol Genet. 2018;27(12):2205-13. Epub 2018/04/05. doi: 10.1093/hmg/ddy111. PubMed PMID: 29617998; PubMed Central PMCID: PMCPMC5985721.
38. Shiga Y, Akiyama M, Nishiguchi KM, Sato K, Shimozawa N, Takahashi A, et al. Genome-wide association study identifies seven novel susceptibility loci for primary open-angle glaucoma. Hum Mol Genet. 2018;27(8):1486-96. Epub 2018/02/17. doi: 10.1093/hmg/ddy053. PubMed PMID: 29452408; PubMed Central PMCID: PMCPMC6251544.
39. Cross SH, Macalinao DG, McKie L, Rose L, Kearney AL, Rainger J, et al. A dominant-negative mutation of mouse Lmx1b causes glaucoma and is semi-lethal via LDB1-mediated dimerization [corrected]. PLoS Genet. 2014;10(5):e1004359. Epub 2014/05/09. doi: 10.1371/journal.pgen.1004359. PubMed PMID: 24809698; PubMed Central PMCID: PMCPMC4014447.
40. Tolman NG, Balasubramanian R, Macalinao DG, Kearney AL, MacNicoll KH, Montgomery CL, et al. Genetic background modifies vulnerability to glaucoma-related phenotypes in Lmx1b mutant mice. Dis Model Mech. 2021;14(2). Epub 2021/01/20. doi: 10.1242/dmm.046953. PubMed PMID: 33462143; PubMed Central PMCID: PMCPMC7903917.
41. Akula M, Taiyab A, Deschamps P, Yee S, Ball AK, Williams T, et al. AP-2beta is required for formation of the murine trabecular meshwork and Schlemm's canal. Exp Eye Res. 2020;195:108042. Epub 2020/05/01. doi: 10.1016/j.exer.2020.108042. PubMed PMID: 32353428; PubMed Central PMCID: PMCPMC8005257.
42. Ostojic J, Grozdanic S, Syed NA, Hargrove MS, Trent JT, 3rd, Kuehn MH, et al. Neuroglobin and cytoglobin distribution in the anterior eye segment: a comparative immunohistochemical study. J Histochem Cytochem. 2008;56(9):863-72. Epub 2008/06/25. doi: 10.1369/jhc.2008.951392. PubMed PMID: 18574250; PubMed Central PMCID: PMCPMC2516955.
43. de Kater AW, Shahsafaei A, Epstein DL. Localization of smooth muscle and nonmuscle actin isoforms in the human aqueous outflow pathway. Invest Ophthalmol Vis Sci. 1992;33(2):424-9. Epub 1992/02/01. PubMed PMID: 1740375.
44. Patel SP, Parker MD. SLC4A11 and the Pathophysiology of Congenital Hereditary Endothelial Dystrophy. Biomed Res Int. 2015;2015:475392. Epub 2015/10/10. doi: 10.1155/2015/475392. PubMed PMID: 26451371; PubMed Central PMCID: PMCPMC4588344.
45. Lopez IA, Rosenblatt MI, Kim C, Galbraith GC, Jones SM, Kao L, et al. Slc4a11 gene disruption in mice: cellular targets of sensorineuronal abnormalities. J Biol Chem. 2009;284(39):26882-96. Epub 2009/07/10. doi: 10.1074/jbc.M109.008102. PubMed PMID: 19586905; PubMed Central PMCID: PMCPMC2785376.
46. Liu CY, Birk DE, Hassell JR, Kane B, Kao WW. Keratocan-deficient mice display alterations in corneal structure. J Biol Chem. 2003;278(24):21672-7. Epub 2003/04/01. doi: 10.1074/jbc.M301169200. PubMed PMID: 12665512.

1645 47. Toyono T, Usui T, Yokoo S, Taketani Y, Nakagawa S, Kuroda M, et al. Angiopoietin-
1646 like 7 is an anti-angiogenic protein required to prevent vascularization of the cornea. PLoS One.
1647 2015;10(1):e0116838. Epub 2015/01/27. doi: 10.1371/journal.pone.0116838. PubMed PMID:
1648 25622036; PubMed Central PMCID: PMCPMC4306551.
1649 48. Monje PV, Sant D, Wang G. Phenotypic and Functional Characteristics of Human
1650 Schwann Cells as Revealed by Cell-Based Assays and RNA-SEQ. Mol Neurobiol.
1651 2018;55(8):6637-60. Epub 2018/01/13. doi: 10.1007/s12035-017-0837-3. PubMed PMID:
1652 29327207; PubMed Central PMCID: PMCPMC6041199.
1653 49. Stratton JA, Kumar R, Sinha S, Shah P, Stykel M, Shapira Y, et al. Purification and
1654 Characterization of Schwann Cells from Adult Human Skin and Nerve. eNeuro. 2017;4(3). Epub
1655 2017/05/18. doi: 10.1523/ENEURO.0307-16.2017. PubMed PMID: 28512649; PubMed Central
1656 PMCID: PMCPMC5432758.
1657 50. Nitzan E, Pfaltzgraff ER, Labosky PA, Kalcheim C. Neural crest and Schwann cell
1658 progenitor-derived melanocytes are two spatially segregated populations similarly regulated by
1659 Foxd3. Proc Natl Acad Sci U S A. 2013;110(31):12709-14. Epub 2013/07/17. doi:
1660 10.1073/pnas.1306287110. PubMed PMID: 23858437; PubMed Central PMCID:
1661 PMCPMC3732929.
1662 51. Ujiie N, Norden PR, Fang R, Beckmann L, Cai Z, Kweon J, et al. Differential roles of
1663 FOXC2 in the trabecular meshwork and Schlemm's canal in glaucomatous pathology. Life Sci
1664 Alliance. 2023;6(9). Epub 2023/07/07. doi: 10.26508/lsa.202201721. PubMed PMID: 37414529;
1665 PubMed Central PMCID: PMCPMC10326420 of patents related to therapeutic targeting of the
1666 ANGPT-TEK pathway in ocular hypertension and glaucoma and owns stock in and is a director
1667 of Mannin Research. SE Quaggin also receives consulting fees from AstraZeneca, Hanssen, the
1668 Lowry Medical Research Foundation, and Roche/Genentech; is Chair of the External Scientific
1669 Advisory Board for AstraZeneca; and is a scientific advisor or member of AstraZeneca,
1670 Genentech/Roche, the Karolinska CVRM Institute, the Lowry Medical Research Institute,
1671 Mannin, and Novartis. HF Zhang has financial interests in Opticent, Inc. The other authors
1672 declare no competing interests.
1673 52. van den Brink SC, Sage F, Vertesy A, Spanjaard B, Peterson-Maduro J, Baron CS, et al.
1674 Single-cell sequencing reveals dissociation-induced gene expression in tissue subpopulations.
1675 Nat Methods. 2017;14(10):935-6. Epub 2017/09/30. doi: 10.1038/nmeth.4437. PubMed PMID:
1676 28960196.
1677 53. Desronvil T, Logan-Wyatt D, Abdrabou W, Triana M, Jones R, Taheri S, et al.
1678 Distribution of COL8A2 and COL8A1 gene variants in Caucasian primary open angle glaucoma
1679 patients with thin central corneal thickness. Mol Vis. 2010;16:2185-91. Epub 2010/12/09.
1680 PubMed PMID: 21139683; PubMed Central PMCID: PMCPMC2994337.
1681 54. Ali M, McKibbin M, Booth A, Parry DA, Jain P, Riazuddin SA, et al. Null mutations in
1682 LTBP2 cause primary congenital glaucoma. Am J Hum Genet. 2009;84(5):664-71. Epub
1683 2009/04/14. doi: 10.1016/j.ajhg.2009.03.017. PubMed PMID: 19361779; PubMed Central
1684 PMCID: PMCPMC2680998.
1685 55. Roberts AL, Mavlyutov TA, Perlmutter TE, Curry SM, Harris SL, Chauhan AK, et al.
1686 Fibronectin extra domain A (FN-EDA) elevates intraocular pressure through Toll-like receptor 4
1687 signaling. Sci Rep. 2020;10(1):9815. Epub 2020/06/20. doi: 10.1038/s41598-020-66756-6.
1688 PubMed PMID: 32555351; PubMed Central PMCID: PMCPMC7299944.

56. Knepper PA, Farbman AI, Telser AG. Aqueous outflow pathway glycosaminoglycans. Exp Eye Res. 1981;32(3):265-77. Epub 1981/03/01. doi: 10.1016/0014-4835(81)90032-4. PubMed PMID: 7227459.
57. Knepper PA, McLone DG. Glycosaminoglycans and outflow pathways of the eye and brain. Pediatr Neurosci. 1985;12(4-5):240-51. Epub 1985/01/01. doi: 10.1159/000120258. PubMed PMID: 3916537.
58. Knepper PA, Goossens W, Hvizd M, Palmberg PF. Glycosaminoglycans of the human trabecular meshwork in primary open-angle glaucoma. Invest Ophthalmol Vis Sci. 1996;37(7):1360-7. Epub 1996/06/01. PubMed PMID: 8641839.
59. Aumailley M. The laminin family. Cell Adh Migr. 2013;7(1):48-55. Epub 2012/12/25. doi: 10.4161/cam.22826. PubMed PMID: 23263632; PubMed Central PMCID: PMCPMC3544786.
60. Aboobakar IF, Kinzy TG, Zhao Y, Fan B, Pasquale LR, Qassim A, et al. Mitochondrial TXNRD2 and ME3 Genetic Risk Scores Are Associated with Specific Primary Open-Angle Glaucoma Phenotypes. Ophthalmology. 2023;130(7):756-63. Epub 2023/02/23. doi: 10.1016/j.ophtha.2023.02.018. PubMed PMID: 36813040; PubMed Central PMCID: PMCPMC10330404.
61. Khawaja AP, Cooke Bailey JN, Kang JH, Allingham RR, Hauser MA, Brilliant M, et al. Assessing the Association of Mitochondrial Genetic Variation With Primary Open-Angle Glaucoma Using Gene-Set Analyses. Invest Ophthalmol Vis Sci. 2016;57(11):5046-52. Epub 2016/09/24. doi: 10.1167/iovs.16-20017. PubMed PMID: 27661856; PubMed Central PMCID: PMCPMC5040191.
62. Zhang ZQ, Xie Z, Chen SY, Zhang X. Mitochondrial dysfunction in glaucomatous degeneration. Int J Ophthalmol. 2023;16(5):811-23. Epub 2023/05/19. doi: 10.18240/ijo.2023.05.20. PubMed PMID: 37206187; PubMed Central PMCID: PMCPMC10172101.
63. Xin Y, Lyu P, Jiang J, Zhou F, Wang J, Blackshaw S, et al. LRLoop: a method to predict feedback loops in cell-cell communication. Bioinformatics. 2022;38(17):4117-26. Epub 2022/07/06. doi: 10.1093/bioinformatics/btac447. PubMed PMID: 35788263; PubMed Central PMCID: PMCPMC9438954.
64. Browaeys R, Saelens W, Saeys Y. NicheNet: modeling intercellular communication by linking ligands to target genes. Nat Methods. 2020;17(2):159-62. Epub 2019/12/11. doi: 10.1038/s41592-019-0667-5. PubMed PMID: 31819264.
65. Shibuya M. Vascular Endothelial Growth Factor (VEGF) and Its Receptor (VEGFR) Signaling in Angiogenesis: A Crucial Target for Anti- and Pro-Angiogenic Therapies. Genes Cancer. 2011;2(12):1097-105. Epub 2012/08/07. doi: 10.1177/1947601911423031. PubMed PMID: 22866201; PubMed Central PMCID: PMCPMC3411125.
66. Saharinen P, Eklund L, Alitalo K. Therapeutic targeting of the angiopoietin-TIE pathway. Nat Rev Drug Discov. 2017;16(9):635-61. Epub 2017/05/23. doi: 10.1038/nrd.2016.278. PubMed PMID: 28529319.
67. Genovesi S, Giussani M, Orlando A, Lieti G, Viazzi F, Parati G. Relationship between endothelin and nitric oxide pathways in the onset and maintenance of hypertension in children and adolescents. Pediatr Nephrol. 2022;37(3):537-45. Epub 2021/06/05. doi: 10.1007/s00467-021-05144-2. PubMed PMID: 34085102; PubMed Central PMCID: PMCPMC8921137.
68. Thomson BR, Grannonico M, Liu F, Liu M, Mendapara P, Xu Y, et al. Angiopoietin-1 Knockout Mice as a Genetic Model of Open-Angle Glaucoma. Transl Vis Sci Technol.

1735 2020;9(4):16. Epub 2020/08/21. doi: 10.1167/tvst.9.4.16. PubMed PMID: 32818103; PubMed
1736 Central PMCID: PMCPMC7396191.
1737 69. Fujimoto T, Inoue T, Maki K, Inoue-Mochita M, Tanihara H. Vascular Endothelial
1738 Growth Factor-A Increases the Aqueous Humor Outflow Facility. PLoS One.
1739 2016;11(9):e0161332. Epub 2016/09/02. doi: 10.1371/journal.pone.0161332. PubMed PMID:
1740 27584577; PubMed Central PMCID: PMCPMC5008796 Senju Pharmaceutical, Santen
1741 Pharmaceutical, Alcon Japan, and Pfizer Japan. This does not alter our adherence to PLOS ONE
1742 policies on sharing data and materials. The other authors have declared that no competing
1743 interests exist.
1744 70. Reina-Torres E, Wen JC, Liu KC, Li G, Sherwood JM, Chang JY, et al. VEGF as a
1745 Paracrine Regulator of Conventional Outflow Facility. Invest Ophthalmol Vis Sci.
1746 2017;58(3):1899-908. Epub 2017/03/31. doi: 10.1167/iovs.16-20779. PubMed PMID: 28358962;
1747 PubMed Central PMCID: PMCPMC5374885.
1748 71. Comes N, Borras T. Individual molecular response to elevated intraocular pressure in
1749 perfused postmortem human eyes. Physiol Genomics. 2009;38(2):205-25. Epub 2009/04/30. doi:
1750 10.1152/physiolgenomics.90261.2008. PubMed PMID: 19401404; PubMed Central PMCID:
1751 PMCPMC2712225.
1752 72. Zhang C, Simon M, Lim H, Tolman NG, Horbal L, Juarez FA, et al. IOP-induced blood-
1753 retinal barrier compromise contributes to RGC death in glaucoma. bioRxiv. 2024. Epub
1754 2024/10/28. doi: 10.1101/2024.10.15.618539. PubMed PMID: 39463998; PubMed Central
1755 PMCID: PMCPMC11507889.
1756 73. Schondorf DC, Ivanyuk D, Baden P, Sanchez-Martinez A, De Cicco S, Yu C, et al. The
1757 NAD+ Precursor Nicotinamide Riboside Rescues Mitochondrial Defects and Neuronal Loss in
1758 iPSC and Fly Models of Parkinson's Disease. Cell Rep. 2018;23(10):2976-88. Epub 2018/06/07.
1759 doi: 10.1016/j.celrep.2018.05.009. PubMed PMID: 29874584.
1760 74. Williams PA, Harder JM, Foxworth NE, Cochran KE, Philip VM, Porciatti V, et al.
1761 Vitamin B(3) modulates mitochondrial vulnerability and prevents glaucoma in aged mice.
1762 Science. 2017;355(6326):756-60. Epub 2017/02/18. doi: 10.1126/science.aal0092. PubMed
1763 PMID: 28209901; PubMed Central PMCID: PMCPMC5408298.
1764 75. Libby RT, Smith RS, Savinova OV, Zabaleta A, Martin JE, Gonzalez FJ, et al.
1765 Modification of ocular defects in mouse developmental glaucoma models by tyrosinase. Science.
1766 2003;299(5612):1578-81. Epub 2003/03/08. doi: 10.1126/science.1080095. PubMed PMID:
1767 12624268.
1768 76. Keller KE, Aga M, Bradley JM, Kelley MJ, Acott TS. Extracellular matrix turnover and
1769 outflow resistance. Exp Eye Res. 2009;88(4):676-82. Epub 2008/12/18. doi:
1770 10.1016/j.exer.2008.11.023. PubMed PMID: 19087875; PubMed Central PMCID:
1771 PMCPMC2700052.
1772 77. Fuchshofer R, Tamm ER. Modulation of extracellular matrix turnover in the trabecular
1773 meshwork. Exp Eye Res. 2009;88(4):683-8. Epub 2009/04/23. doi: 10.1016/j.exer.2009.01.005.
1774 PubMed PMID: 19385040.
1775 78. Wang WH, McNatt LG, Pang IH, Millar JC, Hellberg PE, Hellberg MH, et al. Increased
1776 expression of the WNT antagonist sFRP-1 in glaucoma elevates intraocular pressure. J Clin
1777 Invest. 2008;118(3):1056-64. Epub 2008/02/16. doi: 10.1172/JCI33871. PubMed PMID:
1778 18274669; PubMed Central PMCID: PMCPMC2242621.
1779 79. McDowell CM, Tebow HE, Wordinger RJ, Clark AF. Smad3 is necessary for
1780 transforming growth factor-beta2 induced ocular hypertension in mice. Exp Eye Res.

2013;116:419-23. Epub 2013/11/05. doi: 10.1016/j.exer.2013.10.017. PubMed PMID: 24184030; PubMed Central PMCID: PMCPMC3895953.
80. Shepard AR, Millar JC, Pang IH, Jacobson N, Wang WH, Clark AF. Adenoviral gene transfer of active human transforming growth factor-beta2 elevates intraocular pressure and reduces outflow facility in rodent eyes. Invest Ophthalmol Vis Sci. 2010;51(4):2067-76. Epub 2009/12/05. doi: 10.1167/iovs.09-4567. PubMed PMID: 19959644.
81. Rudzitis CN, Lakk M, Singh A, Redmon SN, Kirdajova D, Tseng YT, et al. TRPV4 activation by TGFbeta2 enhances cellular contractility and drives ocular hypertension. Elife. 2025;14. Epub 2025/06/24. doi: 10.7554/eLife.104894. PubMed PMID: 40552711; PubMed Central PMCID: PMCPMC12187138.
82. Fleenor DL, Shepard AR, Hellberg PE, Jacobson N, Pang IH, Clark AF. TGFbeta2-induced changes in human trabecular meshwork: implications for intraocular pressure. Invest Ophthalmol Vis Sci. 2006;47(1):226-34. Epub 2005/12/31. doi: 10.1167/iovs.05-1060. PubMed PMID: 16384967.
83. Gottanka J, Chan D, Eichhorn M, Lutjen-Drecoll E, Ethier CR. Effects of TGF-beta2 in perfused human eyes. Invest Ophthalmol Vis Sci. 2004;45(1):153-8. Epub 2003/12/24. doi: 10.1167/iovs.03-0796. PubMed PMID: 14691167.
84. Wordinger RJ, Fleenor DL, Hellberg PE, Pang IH, Tovar TO, Zode GS, et al. Effects of TGF-beta2, BMP-4, and gremlin in the trabecular meshwork: implications for glaucoma. Invest Ophthalmol Vis Sci. 2007;48(3):1191-200. Epub 2007/02/28. doi: 10.1167/iovs.06-0296. PubMed PMID: 17325163.
85. Mody AA, Millar JC, Clark AF. ID1 and ID3 are Negative Regulators of TGFbeta2-Induced Ocular Hypertension and Compromised Aqueous Humor Outflow Facility in Mice. Invest Ophthalmol Vis Sci. 2021;62(6):3. Epub 2021/05/04. doi: 10.1167/iovs.62.6.3. PubMed PMID: 33938911; PubMed Central PMCID: PMCPMC8107646.
86. Gagen D, Faralli JA, Filla MS, Peters DM. The role of integrins in the trabecular meshwork. J Ocul Pharmacol Ther. 2014;30(2-3):110-20. Epub 2013/11/26. doi: 10.1089/jop.2013.0176. PubMed PMID: 24266581; PubMed Central PMCID: PMCPMC3991962.
87. Faralli JA, Filla MS, Peters DM. Effect of alphavbeta3 Integrin Expression and Activity on Intraocular Pressure. Invest Ophthalmol Vis Sci. 2019;60(5):1776-88. Epub 2019/04/26. doi: 10.1167/iovs.18-26038. PubMed PMID: 31022732; PubMed Central PMCID: PMCPMC6485315.
88. Yang YF, Sun YY, Peters DM, Keller KE. The Effects of Mechanical Stretch on Integrins and Filopodial-Associated Proteins in Normal and Glaucomatous Trabecular Meshwork Cells. Front Cell Dev Biol. 2022;10:886706. Epub 2022/05/17. doi: 10.3389/fcell.2022.886706. PubMed PMID: 35573666; PubMed Central PMCID: PMCPMC9100841.
89. Bermudez JY, Montecchi-Palmer M, Mao W, Clark AF. Cross-linked actin networks (CLANs) in glaucoma. Exp Eye Res. 2017;159:16-22. Epub 2017/02/28. doi: 10.1016/j.exer.2017.02.010. PubMed PMID: 28238754; PubMed Central PMCID: PMCPMC5499152.
90. Xue W, Comes N, Borras T. Presence of an established calcification marker in trabecular meshwork tissue of glaucoma donors. Invest Ophthalmol Vis Sci. 2007;48(7):3184-94. Epub 2007/06/27. doi: 10.1167/iovs.06-1403. PubMed PMID: 17591888; PubMed Central PMCID: PMCPMC1994153.

1827 91. Borras T, Comes N. Evidence for a calcification process in the trabecular meshwork. Exp
1828 Eye Res. 2009;88(4):738-46. Epub 2008/12/17. doi: 10.1016/j.exer.2008.11.027. PubMed
1829 PMID: 19084518; PubMed Central PMCID: PMCPMC2670947.
1830 92. Saccuzzo EG, Youngblood HA, Lieberman RL. Myocilin misfolding and glaucoma: A
1831 20-year update. Prog Retin Eye Res. 2023;95:101188. Epub 2023/05/23. doi:
1832 10.1016/j.preteyeres.2023.101188. PubMed PMID: 37217093; PubMed Central PMCID:
1833 PMCPMC10330797.
1834 93. Fingert JH, Stone EM, Sheffield VC, Alward WL. Myocilin glaucoma. Surv Ophthalmol.
1835 2002;47(6):547-61. Epub 2002/12/31. doi: 10.1016/s0039-6257(02)00353-3. PubMed PMID:
1836 12504739.
1837 94. Sharma R, Grover A. Myocilin-associated Glaucoma: A Historical Perspective and
1838 Recent Research Progress. Mol Vis. 2021;27:480-93. Epub 2021/09/10. PubMed PMID:
1839 34497454; PubMed Central PMCID: PMCPMC8403517.
1840 95. Herrmann H, Bar H, Kreplak L, Strelkov SV, Aebi U. Intermediate filaments: from cell
1841 architecture to nanomechanics. Nat Rev Mol Cell Biol. 2007;8(7):562-73. Epub 2007/06/07. doi:
1842 10.1038/nrm2197. PubMed PMID: 17551517.
1843 96. Ethier CR. The inner wall of Schlemm's canal. Exp Eye Res. 2002;74(2):161-72. Epub
1844 2002/04/13. doi: 10.1006/exer.2002.1144. PubMed PMID: 11950226.
1845 97. Acott TS, Kingsley PD, Samples JR, Van Buskirk EM. Human trabecular meshwork
1846 organ culture: morphology and glycosaminoglycan synthesis. Invest Ophthalmol Vis Sci.
1847 1988;29(1):90-100. Epub 1988/01/01. PubMed PMID: 3335436.
1848 98. Munger JS, Sheppard D. Cross talk among TGF-beta signaling pathways, integrins, and
1849 the extracellular matrix. Cold Spring Harb Perspect Biol. 2011;3(11):a005017. Epub 2011/09/09.
1850 doi: 10.1101/cshperspect.a005017. PubMed PMID: 21900405; PubMed Central PMCID:
1851 PMCPMC3220354.
1852 99. Meng XM, Nikolic-Paterson DJ, Lan HY. TGF-beta: the master regulator of fibrosis. Nat
1853 Rev Nephrol. 2016;12(6):325-38. Epub 2016/04/26. doi: 10.1038/nrneph.2016.48. PubMed
1854 PMID: 27108839.
1855 100. Frangogiannis N. Transforming growth factor-beta in tissue fibrosis. J Exp Med.
1856 2020;217(3):e20190103. Epub 2020/10/01. doi: 10.1084/jem.20190103. PubMed PMID:
1857 32997468; PubMed Central PMCID: PMCPMC7062524.
1858 101. Biernacka A, Dobaczewski M, Frangogiannis NG. TGF-beta signaling in fibrosis.
1859 Growth Factors. 2011;29(5):196-202. Epub 2011/07/12. doi: 10.3109/08977194.2011.595714.
1860 PubMed PMID: 21740331; PubMed Central PMCID: PMCPMC4408550.
1861 102. Fuchshofer R, Tamm ER. The role of TGF-beta in the pathogenesis of primary open-
1862 angle glaucoma. Cell Tissue Res. 2012;347(1):279-90. Epub 2011/11/22. doi: 10.1007/s00441-
1863 011-1274-7. PubMed PMID: 22101332.
1864 103. Tripathi RC, Li J, Chan WF, Tripathi BJ. Aqueous humor in glaucomatous eyes contains
1865 an increased level of TGF-beta 2. Exp Eye Res. 1994;59(6):723-7. Epub 1994/12/01. doi:
1866 10.1006/exer.1994.1158. PubMed PMID: 7698265.
1867 104. Min SH, Lee TI, Chung YS, Kim HK. Transforming growth factor-beta levels in human
1868 aqueous humor of glaucomatous, diabetic and uveitic eyes. Korean J Ophthalmol.
1869 2006;20(3):162-5. Epub 2006/09/29. doi: 10.3341/kjo.2006.20.3.162. PubMed PMID:
1870 17004630; PubMed Central PMCID: PMCPMC2908840.
1871 105. Overby DR, Bertrand J, Schicht M, Paulsen F, Stamer WD, Lutjen-Drecoll E. The
1872 structure of the trabecular meshwork, its connections to the ciliary muscle, and the effect of

pilocarpine on outflow facility in mice. Invest Ophthalmol Vis Sci. 2014;55(6):3727-36. Epub 2014/05/17. doi: 10.1167/iovs.13-13699. PubMed PMID: 24833737; PubMed Central PMCID: PMCPMC4059081.
106. Shifera AS, Trivedi S, Chau P, Bonnemaison LH, Iguchi R, Alvarado JA. Constitutive secretion of chemokines by cultured human trabecular meshwork cells. Exp Eye Res. 2010;91(1):42-7. Epub 2010/04/21. doi: 10.1016/j.exer.2010.04.001. PubMed PMID: 20403352.
107. Souma T, Tompson SW, Thomson BR, Siggs OM, Kizhatil K, Yamaguchi S, et al. Angiopoietin receptor TEK mutations underlie primary congenital glaucoma with variable expressivity. J Clin Invest. 2016;126(7):2575-87. Epub 2016/06/09. doi: 10.1172/JCI85830. PubMed PMID: 27270174; PubMed Central PMCID: PMCPMC4922711.
108. Kabra M, Zhang W, Rathi S, Mandal AK, Senthil S, Pyatla G, et al. Angiopoietin receptor TEK interacts with CYP1B1 in primary congenital glaucoma. Hum Genet. 2017;136(8):941-9. Epub 2017/06/18. doi: 10.1007/s00439-017-1823-6. PubMed PMID: 28620713; PubMed Central PMCID: PMCPMC5953556.
109. Aspelund A, Tammela T, Antila S, Nurmi H, Leppanen VM, Zarkada G, et al. The Schlemm's canal is a VEGF-C/VEGFR-3-responsive lymphatic-like vessel. J Clin Invest. 2014;124(9):3975-86. Epub 2014/07/26. doi: 10.1172/JCI75395. PubMed PMID: 25061878; PubMed Central PMCID: PMCPMC4153703.
110. DeWane G, Salvi AM, DeMali KA. Fueling the cytoskeleton - links between cell metabolism and actin remodeling. J Cell Sci. 2021;134(3). Epub 2021/02/10. doi: 10.1242/jcs.248385. PubMed PMID: 33558441; PubMed Central PMCID: PMCPMC7888749.
111. Baker N, Patel J, Khacho M. Linking mitochondrial dynamics, cristae remodeling and supercomplex formation: How mitochondrial structure can regulate bioenergetics. Mitochondrion. 2019;49:259-68. Epub 2019/06/18. doi: 10.1016/j.mito.2019.06.003. PubMed PMID: 31207408.
112. Jenkins BC, Neikirk K, Katti P, Claypool SM, Kirabo A, McReynolds MR, et al. Mitochondria in disease: changes in shapes and dynamics. Trends Biochem Sci. 2024;49(4):346-60. Epub 2024/02/25. doi: 10.1016/j.tibs.2024.01.011. PubMed PMID: 38402097; PubMed Central PMCID: PMCPMC10997448.
113. Golombek M, Tsigaras T, Schaumkessel Y, Hansch S, Weidtkamp-Peters S, Anand R, et al. Cristae dynamics is modulated in bioenergetically compromised mitochondria. Life Sci Alliance. 2024;7(2). Epub 2023/11/15. doi: 10.26508/lsa.202302386. PubMed PMID: 37957016; PubMed Central PMCID: PMCPMC10643176.
114. Huang C, Deng K, Wu M. Mitochondrial cristae in health and disease. Int J Biol Macromol. 2023;235:123755. Epub 2023/02/23. doi: 10.1016/j.ijbiomac.2023.123755. PubMed PMID: 36812974.
115. Jezek P, Jaburek M, Holendova B, Engstova H, Dlaskova A. Mitochondrial Cristae Morphology Reflecting Metabolism, Superoxide Formation, Redox Homeostasis, and Pathology. Antioxid Redox Signal. 2023;39(10-12):635-83. Epub 2023/02/17. doi: 10.1089/ars.2022.0173. PubMed PMID: 36793196; PubMed Central PMCID: PMCPMC10615093.
116. Jimenez-Moreno N, Kollareddy M, Stathakos P, Moss JJ, Anton Z, Shoemark DK, et al. ATG8-dependent LMX1B-autophagy crosstalk shapes human midbrain dopaminergic neuronal resilience. J Cell Biol. 2023;222(5). Epub 2023/04/05. doi: 10.1083/jcb.201910133. PubMed PMID: 37014324; PubMed Central PMCID: PMCPMC10075225.
117. Doucet-Beaupre H, Gilbert C, Profes MS, Chabrat A, Pacelli C, Giguere N, et al. Lmx1a and Lmx1b regulate mitochondrial functions and survival of adult midbrain dopaminergic

1919 neurons. Proc Natl Acad Sci U S A. 2016;113(30):E4387-96. Epub 2016/07/14. doi:
1920 10.1073/pnas.1520387113. PubMed PMID: 27407143; PubMed Central PMCID:
1921 PMCPMC4968767.
1922 118. Bergman O, Hakansson A, Westberg L, Belin AC, Sydow O, Olson L, et al. Do
1923 polymorphisms in transcription factors LMX1A and LMX1B influence the risk for Parkinson's
1924 disease? J Neural Transm (Vienna). 2009;116(3):333-8. Epub 2009/02/04. doi: 10.1007/s00702-
1925 009-0187-z. PubMed PMID: 19189040.
1926 119. Jang SY, Kang HT, Hwang ES. Nicotinamide-induced mitophagy: event mediated by
1927 high NAD+/NADH ratio and SIRT1 protein activation. J Biol Chem. 2012;287(23):19304-14.
1928 Epub 2012/04/12. doi: 10.1074/jbc.M112.363747. PubMed PMID: 22493485; PubMed Central
1929 PMCID: PMCPMC3365962.
1930 120. Verdin E. NAD(+) in aging, metabolism, and neurodegeneration. Science.
1931 2015;350(6265):1208-13. Epub 2016/01/20. doi: 10.1126/science.aac4854. PubMed PMID:
1932 26785480.
1933 121. Mouchiroud L, Houtkooper RH, Moullan N, Katsyuba E, Ryu D, Canto C, et al. The
1934 NAD(+)/Sirtuin Pathway Modulates Longevity through Activation of Mitochondrial UPR and
1935 FOXO Signaling. Cell. 2013;154(2):430-41. Epub 2013/07/23. doi: 10.1016/j.cell.2013.06.016.
1936 PubMed PMID: 23870130; PubMed Central PMCID: PMCPMC3753670.
1937 122. Gomes AP, Price NL, Ling AJ, Moslehi JJ, Montgomery MK, Rajman L, et al. Declining
1938 NAD(+) induces a pseudohypoxic state disrupting nuclear-mitochondrial communication during
1939 aging. Cell. 2013;155(7):1624-38. Epub 2013/12/24. doi: 10.1016/j.cell.2013.11.037. PubMed
1940 PMID: 24360282; PubMed Central PMCID: PMCPMC4076149.
1941 123. Imai S, Guarente L. NAD+ and sirtuins in aging and disease. Trends Cell Biol.
1942 2014;24(8):464-71. Epub 2014/05/03. doi: 10.1016/j.tcb.2014.04.002. PubMed PMID:
1943 24786309; PubMed Central PMCID: PMCPMC4112140.
1944 124. Song SB, Park JS, Jang SY, Hwang ES. Nicotinamide Treatment Facilitates
1945 Mitochondrial Fission through Drp1 Activation Mediated by SIRT1-Induced Changes in Cellular
1946 Levels of cAMP and Ca(2). Cells. 2021;10(3). Epub 2021/04/04. doi: 10.3390/cells10030612.
1947 PubMed PMID: 33802063; PubMed Central PMCID: PMCPMC7999186.
1948 125. Kang HT, Hwang ES. Nicotinamide enhances mitochondria quality through autophagy
1949 activation in human cells. Aging Cell. 2009;8(4):426-38. Epub 2009/05/29. doi: 10.1111/j.1474-
1950 9726.2009.00487.x. PubMed PMID: 19473119.
1951 126. Sweeney E, Fryer A, Mountford R, Green A, McIntosh I. Nail patella syndrome: a review
1952 of the phenotype aided by developmental biology. J Med Genet. 2003;40(3):153-62. Epub
1953 2003/03/08. doi: 10.1136/jmg.40.3.153. PubMed PMID: 12624132; PubMed Central PMCID:
1954 PMCPMC1735400.
1955 127. Chen H, Lun Y, Ovchinnikov D, Kokubo H, Oberg KC, Pepicelli CV, et al. Limb and
1956 kidney defects in Lmx1b mutant mice suggest an involvement of LMX1B in human nail patella
1957 syndrome. Nat Genet. 1998;19(1):51-5. Epub 1998/05/20. doi: 10.1038/ng0598-51. PubMed
1958 PMID: 9590288.
1959 128. Vollrath D, Jaramillo-Babb VL, Clough MV, McIntosh I, Scott KM, Lichter PR, et al.
1960 Loss-of-function mutations in the LIM-homeodomain gene, LMX1B, in nail-patella syndrome.
1961 Hum Mol Genet. 1998;7(7):1091-8. Epub 1998/06/09. doi: 10.1093/hmg/7.7.1091. PubMed
1962 PMID: 9618165.
1963 129. Choquet H, Thai KK, Yin J, Hoffmann TJ, Kvale MN, Banda Y, et al. A large multi-
1964 ethnic genome-wide association study identifies novel genetic loci for intraocular pressure. Nat

1965 Commun. 2017;8(1):2108. Epub 2017/12/14. doi: 10.1038/s41467-017-01913-6. PubMed PMID:
1966 29235454; PubMed Central PMCID: PMCPMC5727399.
1967 130. Hui F, Tang J, Williams PA, McGuinness MB, Hadoux X, Casson RJ, et al. Improvement
1968 in inner retinal function in glaucoma with nicotinamide (vitamin B3) supplementation: A
1969 crossover randomized clinical trial. Clin Exp Ophthalmol. 2020;48(7):903-14. Epub 2020/07/29.
1970 doi: 10.1111/ceo.13818. PubMed PMID: 32721104.
1971 131. Williams PA, Harder JM, Foxworth NE, Cardozo BH, Cochran KE, John SWM.
1972 Nicotinamide and WLD(S) Act Together to Prevent Neurodegeneration in Glaucoma. Front
1973 Neurosci. 2017;11:232. Epub 2017/05/11. doi: 10.3389/fnins.2017.00232. PubMed PMID:
1974 28487632; PubMed Central PMCID: PMCPMC5403885.
1975 132. Williams PA, Harder JM, Cardozo BH, Foxworth NE, John SWM. Nicotinamide
1976 treatment robustly protects from inherited mouse glaucoma. Commun Integr Biol.
1977 2018;11(1):e1356956. Epub 2018/03/03. doi: 10.1080/19420889.2017.1356956. PubMed PMID:
1978 29497468; PubMed Central PMCID: PMCPMC5824969.
1979 133. De Moraes CG, John SWM, Williams PA, Blumberg DM, Cioffi GA, Liebmann JM.
1980 Nicotinamide and Pyruvate for Neuroenhancement in Open-Angle Glaucoma: A Phase 2
1981 Randomized Clinical Trial. JAMA Ophthalmol. 2022;140(1):11-8. Epub 2021/11/19. doi:
1982 10.1001/jamaophthalmol.2021.4576. PubMed PMID: 34792559; PubMed Central PMCID:
1983 PMCPMC8603231 Belite, Carl Zeiss Meditec, Galimedix, Genentech, Novartis, Ora, Thea, and
1984 Reichert outside the submitted work and from Heidelberg Engineering, the National Institutes of
1985 Health, the US Centers for Disease Control and Prevention, and Topcon during the conduct of
1986 the study. Drs John and Williams are inventors on a patent application filed by the Jackson
1987 Laboratory that covers nicotinamide- and pyruvate-based therapies in glaucoma. Dr John was
1988 employed by Howard Hughes Medical Institute during the conduct of the study. Dr Liebmann
1989 reports support from Allergan, Carl Zeiss Meditec, Genentech, and Thea outside the submitted
1990 work. No other disclosures were reported.
1991 134. Abu-Amero KK, Morales J, Bosley TM. Mitochondrial abnormalities in patients with
1992 primary open-angle glaucoma. Invest Ophthalmol Vis Sci. 2006;47(6):2533-41. Epub
1993 2006/05/26. doi: 10.1167/iovs.05-1639. PubMed PMID: 16723467.
1994 135. Lo Faro V, Nolte IM, Ten Brink JB, Snieder H, Jansonius NM, Bergen AA.
1995 Mitochondrial Genome Study Identifies Association Between Primary Open-Angle Glaucoma
1996 and Variants in MT-CYB, MT-ND4 Genes and Haplogroups. Front Genet. 2021;12:781189.
1997 Epub 2022/01/04. doi: 10.3389/fgene.2021.781189. PubMed PMID: 34976016; PubMed Central
1998 PMCID: PMCPMC8719162.
1999 136. Petriti B, Rabiolo A, Chau KY, Williams PA, Montesano G, Lascaratos G, et al.
2000 Peripheral blood mononuclear cell respiratory function is associated with progressive
2001 glaucomatous vision loss. Nat Med. 2024;30(8):2362-70. Epub 2024/06/18. doi:
2002 10.1038/s41591-024-03068-6. PubMed PMID: 38886621; PubMed Central PMCID:
2003 PMCPMC11333286 and Viatris. G.M. received consultation fees from Alcon and Omikron. G.L.
2004 has research funding from Aerie, Abbvie and other remuneration received by Glaukos and
2005 Rayner. P.A.W. is an inventor on an awarded US patent held by The Jackson Laboratory for
2006 NAM treatment in glaucoma (Treatment and prevention of ocular neurodegenerative disorder,
2007 US11389439B2).
2008 137. Venkatesan A, Bernstein AM. Protein misfolding and mitochondrial dysfunction in
2009 glaucoma. Front Cell Dev Biol. 2025;13:1595121. Epub 2025/05/19. doi:

10.3389/fcell.2025.1595121. PubMed PMID: 40385286; PubMed Central PMCID: PMCPMC12083186.
138. Venkatesan A, Ridilla M, Castro N, Wolosin JM, Henty-Ridilla JL, Knox BE, et al. Mitochondrial and microtubule defects in Exfoliation Glaucoma. Free Radic Biol Med. 2025;233:226-39. Epub 2025/04/04. doi: 10.1016/j.freeradbiomed.2025.03.046. PubMed PMID: 40180018; PubMed Central PMCID: PMCPMC12074171.
139. Thaung C, West K, Clark BJ, McKie L, Morgan JE, Arnold K, et al. Novel ENU-induced eye mutations in the mouse: models for human eye disease. Hum Mol Genet. 2002;11(7):755-67. Epub 2002/04/04. doi: 10.1093/hmg/11.7.755. PubMed PMID: 11929848.
140. John SW, Hagaman JR, MacTaggart TE, Peng L, Smithes O. Intraocular pressure in inbred mouse strains. Invest Ophthalmol Vis Sci. 1997;38(1):249-53. Epub 1997/01/01. PubMed PMID: 9008647.
141. Savinova OV, Sugiyama F, Martin JE, Tomarev SI, Paigen BJ, Smith RS, et al. Intraocular pressure in genetically distinct mice: an update and strain survey. BMC Genet. 2001;2:12. Epub 2001/09/05. doi: 10.1186/1471-2156-2-12. PubMed PMID: 11532192; PubMed Central PMCID: PMCPMC48141.
142. Corces MR, Trevino AE, Hamilton EG, Greenside PG, Sinnott-Armstrong NA, Vesuna S, et al. An improved ATAC-seq protocol reduces background and enables interrogation of frozen tissues. Nat Methods. 2017;14(10):959-62. Epub 2017/08/29. doi: 10.1038/nmeth.4396. PubMed PMID: 28846090; PubMed Central PMCID: PMCPMC5623106.
143. Hao Y, Hao S, Andersen-Nissen E, Mauck WM, 3rd, Zheng S, Butler A, et al. Integrated analysis of multimodal single-cell data. Cell. 2021;184(13):3573-87 e29. Epub 2021/06/02. doi: 10.1016/j.cell.2021.04.048. PubMed PMID: 34062119; PubMed Central PMCID: PMCPMC8238499.
144. Stuart T, Srivastava A, Madad S, Lareau CA, Satija R. Single-cell chromatin state analysis with Signac. Nat Methods. 2021;18(11):1333-41. Epub 2021/11/03. doi: 10.1038/s41592-021-01282-5. PubMed PMID: 34725479; PubMed Central PMCID: PMCPMC9255697.
145. Granja JM, Corces MR, Pierce SE, Bagdatli ST, Choudhry H, Chang HY, et al. ArchR is a scalable software package for integrative single-cell chromatin accessibility analysis. Nat Genet. 2021;53(3):403-11. Epub 2021/02/27. doi: 10.1038/s41588-021-00790-6. PubMed PMID: 33633365; PubMed Central PMCID: PMCPMC8012210 associated with ATAC-seq. W.J.G. has additional affiliations with Guardant Health (consultant) and Protillion Biosciences (cofounder and consultant). H.Y.C. is a cofounder of Accent Therapeutics and Boundless Bio and is a consultant for Arsenal Biosciences and Spring Discovery.
146. Timmons JA, Szkop KJ, Gallagher IJ. Multiple sources of bias confound functional enrichment analysis of global -omics data. Genome Biol. 2015;16(1):186. Epub 2015/09/09. doi: 10.1186/s13059-015-0761-7. PubMed PMID: 26346307; PubMed Central PMCID: PMCPMC4561415.
147. Yu G, Wang LG, Han Y, He QY. clusterProfiler: an R package for comparing biological themes among gene clusters. OMICS. 2012;16(5):284-7. Epub 2012/03/30. doi: 10.1089/omi.2011.0118. PubMed PMID: 22455463; PubMed Central PMCID: PMCPMC3339379.
148. van Koolwijk LM, Ramdas WD, Ikram MK, Jansonius NM, Pasutto F, Hysi PG, et al. Common genetic determinants of intraocular pressure and primary open-angle glaucoma. PLoS

2055 Genet. 2012;8(5):e1002611. Epub 2012/05/10. doi: 10.1371/journal.pgen.1002611. PubMed
2056 PMID: 22570627; PubMed Central PMCID: PMCPMC3342933.
2057 149. Hysi PG, Cheng CY, Springelkamp H, Macgregor S, Bailey JNC, Wojciechowski R, et
2058 al. Genome-wide analysis of multi-ancestry cohorts identifies new loci influencing intraocular
2059 pressure and susceptibility to glaucoma. Nat Genet. 2014;46(10):1126-30. Epub 2014/09/01. doi:
2060 10.1038/ng.3087. PubMed PMID: 25173106; PubMed Central PMCID: PMCPMC4177225.
2061 150. Springelkamp H, Iglesias AI, Mishra A, Hohn R, Wojciechowski R, Khawaja AP, et al.
2062 New insights into the genetics of primary open-angle glaucoma based on meta-analyses of
2063 intraocular pressure and optic disc characteristics. Hum Mol Genet. 2017;26(2):438-53. Epub
2064 2017/01/12. doi: 10.1093/hmg/ddw399. PubMed PMID: 28073927; PubMed Central PMCID:
2065 PMCPMC5968632.
2066 151. Blue Mountains Eye S, Wellcome Trust Case Control C. Genome-wide association study
2067 of intraocular pressure identifies the GLCCI1/ICA1 region as a glaucoma susceptibility locus.
2068 Hum Mol Genet. 2013;22(22):4653-60. Epub 2013/07/10. doi: 10.1093/hmg/ddt293. PubMed
2069 PMID: 23836780; PubMed Central PMCID: PMCPMC3904806.
2070 152. Nag A, Venturini C, Small KS, International Glaucoma Genetics C, Young TL,
2071 Viswanathan AC, et al. A genome-wide association study of intra-ocular pressure suggests a
2072 novel association in the gene FAM125B in the TwinsUK cohort. Hum Mol Genet.
2073 2014;23(12):3343-8. Epub 2014/02/13. doi: 10.1093/hmg/ddu050. PubMed PMID: 24518671;
2074 PubMed Central PMCID: PMCPMC4030784.
2075 153. Springelkamp H, Iglesias AI, Cuellar-Partida G, Amin N, Burdon KP, van Leeuwen EM,
2076 et al. ARHGEF12 influences the risk of glaucoma by increasing intraocular pressure. Hum Mol
2077 Genet. 2015;24(9):2689-99. Epub 2015/02/01. doi: 10.1093/hmg/ddv027. PubMed PMID:
2078 25637523.
2079 154. Ozel AB, Moroi SE, Reed DM, Nika M, Schmidt CM, Akbari S, et al. Genome-wide
2080 association study and meta-analysis of intraocular pressure. Hum Genet. 2014;133(1):41-57.
2081 Epub 2013/09/05. doi: 10.1007/s00439-013-1349-5. PubMed PMID: 24002674; PubMed Central
2082 PMCID: PMCPMC3982323.
2083 155. Bonnemaijer PWM, Iglesias AI, Nadkarni GN, Sanyiwa AJ, Hassan HG, Cook C, et al.
2084 Genome-wide association study of primary open-angle glaucoma in continental and admixed
2085 African populations. Hum Genet. 2018;137(10):847-62. Epub 2018/10/15. doi: 10.1007/s00439-
2086 018-1943-7. PubMed PMID: 30317457; PubMed Central PMCID: PMCPMC6754628.
2087 156. Verma SS, Gudiseva HV, Chavali VRM, Salowe RJ, Bradford Y, Guare L, et al. A multi-
2088 cohort genome-wide association study in African ancestry individuals reveals risk loci for
2089 primary open-angle glaucoma. Cell. 2024;187(2):464-80 e10. Epub 2024/01/20. doi:
2090 10.1016/j.cell.2023.12.006. PubMed PMID: 38242088.
2091 157. Bailey JN, Loomis SJ, Kang JH, Allingham RR, Gharahkhani P, Khor CC, et al.
2092 Genome-wide association analysis identifies TXNRD2, ATXN2 and FOXC1 as susceptibility
2093 loci for primary open-angle glaucoma. Nat Genet. 2016;48(2):189-94. Epub 2016/01/12. doi:
2094 10.1038/ng.3482. PubMed PMID: 26752265; PubMed Central PMCID: PMCPMC4731307.
2095 158. Craig JE, Han X, Qassim A, Hassall M, Cooke Bailey JN, Kinzy TG, et al. Multitrait
2096 analysis of glaucoma identifies new risk loci and enables polygenic prediction of disease
2097 susceptibility and progression. Nat Genet. 2020;52(2):160-6. Epub 2020/01/22. doi:
2098 10.1038/s41588-019-0556-y. PubMed PMID: 31959993; PubMed Central PMCID:
2099 PMCPMC8056672.

2100 159. Weirauch MT, Yang A, Albu M, Cote AG, Montenegro-Montero A, Drewe P, et al.
2101 Determination and inference of eukaryotic transcription factor sequence specificity. Cell.
2102 2014;158(6):1431-43. Epub 2014/09/13. doi: 10.1016/j.cell.2014.08.009. PubMed PMID:
2103 25215497; PubMed Central PMCID: PMCPMC4163041.
2104 160. Schep AN, Wu B, Buenrostro JD, Greenleaf WJ. chromVAR: inferring transcription-
2105 factor-associated accessibility from single-cell epigenomic data. Nat Methods. 2017;14(10):975-
2106 8. Epub 2017/08/22. doi: 10.1038/nmeth.4401. PubMed PMID: 28825706; PubMed Central
2107 PMCID: PMCPMC5623146.
2108 161. Lam J, Katti P, Biete M, Mungai M, AshShareef S, Neikirk K, et al. A Universal
2109 Approach to Analyzing Transmission Electron Microscopy with ImageJ. Cells. 2021;10(9). Epub
2110 2021/09/29. doi: 10.3390/cells10092177. PubMed PMID: 34571826; PubMed Central PMCID:
2111 PMCPMC8465115.
2112 162. Neikirk K, Lopez EG, Marshall AG, Alghanem A, Krystofiak E, Kula B, et al. Call to
2113 action to properly utilize electron microscopy to measure organelles to monitor disease. Eur J
2114 Cell Biol. 2023;102(4):151365. Epub 2023/10/22. doi: 10.1016/j.ejcb.2023.151365. PubMed
2115 PMID: 37864884.
2116